VILNIUS UNIVERSITY
CENTER FOR PHYSICAL SCIENES AND TECHNOLOGY
INSTITUTE OF PHYSICS

Paulius Gečys

ULTRASHORT PULSED LASER PROCESSING OF THIN-FILMS FOR SOLAR CELLS

Doctoral dissertation
Technological Sciences, Material Engineering (08T)
Laser Technology (T165)

Vilnius, 2012

The research was performed at the Institute of Physics of the Center for Physical Sciences and Technology in 2008-2012.

Scientific supervisor:

Dr. Gediminas Račiukaitis (Department of Laser Technologies of the Center for Physical Sciences and Technology, technological sciences, material engineering – 08T, laser technology - T165).

VILNIAUS UNIVERSITETAS
FIZINIŲ IR TECHNOLOGIJOS MOKSLŲ CENTRO
FIZIKOS INSTITUTAS

Paulius Gečys

PLONASLUOKSNIŲ SAULĖS ELEMENTŲ APDIRBIMAS ULTRATRUMPAIS LAZERIŲ IMPULSAIS

Daktaro disertacija
Technologijos mokslai, Medžiagų inžinerija (08T)
Lazerinė technologija (T165)

Vilnius, 2012

Disertacija rengta 2008-2012 metais Fizinių ir technologijos mokslų centro Fizikos institute.

Mokslinis vadovas:

Dr. Gediminas Račiukaitis (Fizinių ir technologijos mokslų centro Lazerinių technologijų skyrius, technologijos mokslai, medžiagų inžinerija -08T, lazerinė technologija - T165).

CONTENTS

ACKNOWLEDGMENTS

The work was supported by the Lithuanian State Science and Studies Foundation under Project No B31/2008 and the Research Council of Lithuania under project No AUT-06/2010.

I would like to thank the Research Council of Lithuania for supporting my internship to the Leibniz Institute for Surface Modification under project “Promotion of student academic activity”.

I am very grateful to my scientific supervisor Dr. G. Račiukaitis for huge support in preparing this dissertation.

I would also like to thank Dr. M. Gedvilas for the valuable discussions and support with modeling.

I want to thank my colleagues Dr. A. Selskis from the Institute of Chemistry of the Center for Physical Sciences and Technology in Vilnius and K. Zimmer, M. Ehrhardt and A. Wehrmann from the Leibniz Institute for Surface Modification in Germany, for the access to their research facilities and valuable discussions.

Thanks to Solarion AG, Germany for the support with solar cell samples.

Thanks to my colleagues B. Voisiat, E. Stankevičius, R. Trusovas, E. Markauskas, Dr. M. Maciulevičius for the friendly atmosphere in the laboratory.

I would also like to thank my wife Marta for the support and every day question “*Tai kiek puslapių parašei šiandien?*“.

LIST OF ABBREVIATIONS

μ-Si	Microcrystalline silicon
a-Si	Amorphous silicon
CdS	Cadmium sulfide
CdTe	Cadmium telluride
CIGS	Copper indium gallium (di)selenide ($Cu(In,Ga)Se_2$)
c-Si	Crystalline silicon
EDS	X-ray energy dispersion spectroscopy
FBS	Fundamental beam-mode shaper
fs	Femtosecond (10^{-15} s)
ITO	Indium tin oxide
LBIC	Laser-beam-induced current
LIT	Lock-in thermography
mc-Si	Multicrystalline silicon
ns	Nanosecond (10^{-9} s)
ps	Picosecond (10^{-12} s)
PV	Photovoltaic
QNR	Quasi-neutral region
R&D	Research and development
SCR	Space charged region
TCO	Transparent conductive oxide
TF-Si	Thin-film silicon
UV	Ultraviolet radiation
W_P	Peak power
ZnO	Zinc oxide

1 INTRODUCTION

Presently, the world's energy consumption is 10 terawatts (TW) per year, and by 2050, it is projected to be about 30 TW. The world will need about 20 TW of "clean" energy to stabilize CO_2 concentration in the atmosphere by the mid of this century. The simplest scenario to stabilize the CO_2 concentration is one in which photovoltaics (PV) and other renewable energy sources are used for electricity generation (10 TW), hydrogen is used for transportation (10 TW), and fossil fuel is only used for residential and industrial heating (10 TW) [1,2]. Thus, PV will play a significant role in meeting the future demands of global supply [2,3].

Photovoltaics market is now dominated by crystalline silicon solar cells. Continuously increasing demand for PV modules and the need for low-cost PV options have stretched this type of cells to the limit and exposed some inherent disadvantages of the c-Si technology such as costly processing of materials and device fabrication steps. This, in turn, restricts the potential of Si wafer technology and it appears difficult to achieve sustainable PV module production costs below $1/W with typical lifetime of 20-30 years, which is considered essential for cost-competitive generation of solar electricity [2].

Recently, commercial interest has started to shift towards thin-film solar cells [4]. Saving of materials, manufacturing time and weight of modules are driving an interest in the thin-film solar cells. $CuIn_xGa_{1-x}Se_2$ (CIGS) is one of the most promising semiconductors for the absorber-layer of the thin-film solar cells [5,6]. These cells show record efficiencies of up to 20.3 % [7] in laboratory conditions and up to 15.7 % of module efficiency in mass production [8]. Further manufacturing process optimization and cost reduction is needed for wider application of these devices. A lot of effort is made to develop new cost-effective manufacturing technologies in order to increase the cell efficiency. Wider use of laser-based tools may be the key to optimize and reduce manufacturing cost of the PV devices and moving the cell efficiency to higher levels.

Laser processing offers a ‘non-contact’ means of scribing, drilling, and melting of specific materials used within production steps of the crystalline-silicon (c-Si) and thin-film solar cell manufacturing [9]. To maintain the PV efficiency of the large thin-film module, it should be divided into smaller cells connected in series in order to increase the generated voltage and maintain the single cell efficiency over a large area. Interconnection between separated cells can be made by a sequence of deposition and structuring steps, including three laser scribing processes. The P1 process is intended for patterning of the Mo back-contact. In the P2 process, the CIGS absorber is scribed by a mechanical or laser tool, and the scribe allows the connection of a front-contact of the neighboring cell with the Mo back-contact of the patterned cell. Isolation of individual cells after the deposition of the conductive and transparent ZnO window layer is defined as the P3 process [10].

For CdTe and a-Si/μ-Si thin-film solar cells on the glass substrate, the laser scribing can be arranged through the substrate by the so-called “lift-off” process to minimize the thermal effects [11]. Use of flexible substrates and metallic back-contacts for the CIGS solar cell manufacturing eliminates possibility to scribe through the substrate side. Only the front-side scribing could be applied with the direct laser ablation process, although no reliable industrial processes have been developed yet. The main limiting factors for laser processing of the multilayer $Cu(In,Ga)Se_2$ structures are deposition of molybdenum on walls of channels scribed in the films, and phase transition of semi-conducting $CuInSe_2$ to the metallic phase close to the ablation area due to the thermal effects [12]. Both effects shunt the device and reduce its photoelectrical conversion efficiency. Various laser sources were tested for selective ablation of thin-films [12-15]. Nanosecond laser pulses were found to be not favorable for the damage-free front-side scribing of the thin-film CIGS solar cells. According to the results of theoretical modeling, processing without damage is possible with ultra-short-pulse lasers [14,16], which stimulated our research.

In this thesis the experimental and modeling results on the P3 laser scribing of CIGS solar cells are presented. The original results are presented in four chapters of the thesis. In chapter 6, scribing experiments with the picosecond laser different wavelengths together with modeling of the laser energy coupling and heat transfer in the thin-film layers of the GIGS solar cells are presented and discussed. In chapter 7, the scribing results at picosecond and femtosecond pulse durations are presented. The process optimization toward industrial implementation is presented in chapter 8. In chapter 9, the results on the solar cell characterization using various techniques after the laser scribing are presented.

1.1 The aim of the research

The aim of the research was to investigate the possibilities of using the ultrashort pulsed lasers in the thin-film scribing processes. For this purpose two tasks were considered:

1. To model and investigate processes of the ultrashort-pulsed laser ablation and the residual thermal effects in the multilayer CIGS thin-film solar cell structures.
2. To develop the laser scribing processes for the flexible thin-film CIGS solar cells on the polymer substrate and propose concepts for the process industrialization.

1.2 The practical value and novelty of thesis

Numerous research groups are working to find the thin-film laser scribing processes suitable for industrial implementation. However, in case of flexible solar cells, no reliable industrial laser scribing processes have been developed yet. Use of ultrashort-pulsed lasers enables us to achieve scribing processes with a low thermal damage to the flexible solar cell structure.

The novelty of this study was in the use of a wide range of wavelengths from the laser for the scribing experiments. The layer ablation has been carried out using 1575 nm, 1064 nm, 532 nm, 355 nm and 266 nm wavelengths. The novel model of laser irradiation energy coupling in thin layers has been developed for the complex structure of the thin-film solar cells and it was confirmed by experimental results on selective film removal. The new front side laser scribing regime was proposed for the P3 type process using the “lift-off” mechanism. Finally, use of the ultrashort-pulsed lasers enabled us to develop the industrial-grade thin layer scribing processes which can be implemented.

1.3 Statements to be defended

1. Selection of the proper laser wavelength is important to keep the energy coupling in a well defined volume at the interlayer interface and this can trigger a selective removal of layers even in the front-side irradiation geometry.
2. The 1064 nm wavelength is optimal for the P3 type scribing with picosecond lasers of the thin-film CIGS solar cells due to matching with optical properties of the films and its absorption facilitates the thermo-mechanical removal process of the CIGS layer.
3. Picosecond laser pulses provide a higher layer removal efficiency although the remaining thermal impact on the thin layers is larger compared to the femtosecond regime.
4. Use of the flat-top shaped laser beam affords reduction of the intermediate area on the trench edges, where melting of the CIGS layer takes place.
5. Parallel processing with several beams obtained by splitting the initial output from the laser provides means for reliable scribing of the films and is a way to increase the overall process speed.

1.4 Approbation

Results of the research, presented in this thesis, were published in scientific papers **[A1-A8]** and together with coauthors the results were presented in contributions to conferences **[C1-C25]**.

Publications related to the topic of the thesis (ISI WoS - with Conference Proceedings)

[A1] G. Račiukaitis, S.Grubinskas, **P. Gečys**, M. Gedvilas: Selectiveness of laser processing due to energy coupling localization: case of thin film solar cell scribing, Applied Physics A, 2012. (**accepted for publication).**

[A2] G. Račiukaitis, **P. Gečys**, M. Gedvilas and B. Voisiat: Structuring of functional thin films and surfaces with picosecond-pulsed lasers, Proc. SPIE **8243**, 824316, (2012).

[A3] P. Gečys, G. Račiukaitis, A. Wehrmann, K. Zimmer, A. Braun, S. Ragnow: Scribing of thin-film solar cells with picosecond and femtosecond lasers, J. Laser Micro/Nanoengineering, **7**, 33-37, (2012).

[A4] P. Gečys, G. Račiukaitis, E. Miltenis, A. Braun and S. Ragnow: Scribing of thin-film solar cells with picosecond laser pulses, Physics Procedia **12**, 141-148, (2011).

[A5] G. Račiukaitis, E. Stankevičius, **P. Gečys**, M. Gedvilas, C. Bischoff, E. Jäger, U. Umhofer, F. Völklein: Laser processing by using diffractive optical laser beam shaping technique, J. Laser Micro/Nanoengineering **6**, 37-43 (2011).

[A6] G. Račiukaitis and **P. Gečys**: Picosecond-laser structuring of thin films for CIGS solar cells, J. Laser Micro/Nanoengineering **5**, 10-15, (2010).

[A7] P. Gečys, G. Račiukaitis, M. Ehrhardt, K. Zimmer and M. Gedvilas: ps-laser scribing of CIGS films at different wavelengths, Applied Physics A: Materials Science & Processing **101**, 373-378, (2010).

[A8] **P. Gečys**, G. Račiukaitis, M. Gedvilas and A. Selskis: Laser structuring of thin-film solar cells on polymers, The European Physical Journal Applied Physics **46**, 12508, (2009).

Publications not directly related to the thesis (ISI WoS - with Conference Proceedings)

[A9] **P. Gečys** and G. Račiukaitis: Scribing of a-Si thin-film solar cells with picosecond laser, The European Physical Journal Applied Physics **51**, 33209, (2010).

[A10] M. Ehrhardt, G. Račiukaitis, **P. Gečys** and K. Zimmer: Microstructuring of fused silica by laser-induced backside wet etching using picosecond laser pulses, Applied Surface Science **256**, 7222-7227, (2010).

[A11] M. Ehrhardt, G. Račiukaitis, **P. Gečys** and K. Zimmer: Laser-induced backside wet etching of fluoride and sapphire using picosecond laser pulses, Applied Physics A: Materials Science & Processing **101**, 399-404, (2010).

[A12] G. Račiukaitis, M. Brikas, **P. Gečys**, B. Voisiat and M. Gedvilas: Use of high repetition rate and high power lasers in microfabrication: how to keep the efficiency high?, J. Laser Micro/Nanoengineering **4**, 186-191, (2009).

[A13] M. Gedvilas, G. Račiukaitis, K. Regelskis and **P. Gečys**: Formation of Gratings by Self-Organization of the Chromium Thin Film on the Glass Substrate under Irradiation with Laser Pulses J. Laser Micro/Nanoengineering 3, 1, (2008).

[A14] G. Račiukaitis, M. Brikas, **P. Gečys** and M. Gedvilas: Accumulation effects in laser ablation of metals with high-repetition-rate lasers, Proc. SPIE **7005**, 70052L, (2008).

[A15] K. Regelskis, G. Račiukaitis and **P.Gečys**: Ripple formation at laser ablation of chromium thin film, Proc. SPIE **6596**, 65960Q, (2007).

Author's presentations directly related to the topic of the thesis

[C1] P. Gečys, G. Račiukaitis: Ultrashort pulsed laser processing of thin-film CIGS solar cells, Photovoltaic Technical Conference - Thin Film & Advanced Silicon Solutions, Aix-en-Provence, June 6-8, 2012. (poster)

[C2] P. Gečys, G. Račiukaitis: Ultrashort pulsed laser processing of thin-films for photovoltaics, 4-th Int. Conf. „Radiation interaction with material and it use in technologies 2012“, Kaunas, Lithuania, 14-17 May, 2012. (oral)

[C3] P. Gečys, G. Račiukaitis, A. Wehrmann, K. Zimmer, A. Braun, S. Ragnow, Scribing of thin-film solar cells with picosecond and femtosecond lasers, The 12th International Symposium on Laser Precision Microfabrication (LPM2011), Takamatsu, Japan, June 7-10, 2011. (oral)

[C4] P. Gečys, G. Račiukaitis, E. Miltenis, A. Braun, S. Ragnow, Scribing of thin-film solar cells with picosecond laser pulses, Int. conf. Lasers in Manufacturing (LiM 2011), Munich, Germany, May 23-26, 2011. (oral)

[C5] P. Gečys, G. Račiukaitis, A. Braun, S. Ragnow, Ultrashort pulse laser scribing of thin-film CIGS solar cells, E-MRS 2011 Spring Meeting, Symposium: J, Laser materials processing for micro and nano applications, Nice, France, May 9-13, 2011. (poster)

[C6] P.Gečys, Ultrashort pulse laser scribing of thin-film CIGS solar cells, The 13th International Conference-School Advanced materials and technologies, Palanga, Lithuania, August 27-31, 2011. (poster)

[C7] P. Gečys, G. Račiukaitis, A. Braun, S. Ragnow, Ps- laser scribing of CIGS at 1064 nm wavelength, Alexander von Humboldt forum „Science & Society in Modern Europe“, Vilnius, Lithuania, September 23-26, 2010. (poster)

[C8] P. Gečys, G. Račiukaitis, A. Braun, S. Ragnow, Ps-laser scribing of CIGS at 1064 nm wavelength, 11th International Symposium on Laser Precision Microfabrication, Stuttgart, Germany, June 7-10, 2010. (poster)

[C9] P. Gečys, G. Račiukaitis, M. Gedvilas, A., Selskis, Laser structuring of thin-film solar cells on polymers, 12th Nordic Conference in Laser Processing of Materials, NOLAMP, Copenhagen, August 24– 26, 2009. (oral)

[C10] P. Gečys, G. Račiukaitis, Scribing of a-Si thin-film Solar Cells with Picosecond Laser, 2nd International Symposium on Flexible Organic Electronics (IS-FOE09), Halkidiki, Greece, July 8-10, 2009. (oral)

[C11] P. Gečys, G. Račiukaitis, M. Gedvilas, A. Selskis, Laser structuring of thin-film solar cells on polymers, 1st International Symposium on Flexible Organic Electronics (IS-FOE), Halkidiki, Greece, July 10-11, 2008. (poster)

Contribution to presentations directly related to the topic of the thesis

[C12] G. Račiukaitis, **P. Gečys**, M. Gedvilas, B. Voisiat: Structuring of functional thin films and surfaces with picosecond-pulsed lasers, SPIE Photonics West, LASE, Conference 8244 "Laser-based Micro- and Nanopackaging and Assembly" VI, San Francisco, California, USA, January 21-26, 2012. (invited)

[C13] G. Račiukaitis, **P. Gečys**, S. Grubinskas, M. Gedvilas, A. Braun, S. Ragnow, Progress in picosecond-laser scribing for CIGS solar cells, The 12th International Symposium on Laser Precision Microfabrication (LPM2011), Takamatsu, Japan, June 7-10, 2011. (oral)

[C14] P. Gečys, G. Račiukaitis, M. Gedvilas, A. Braun, S. Ragnow, Scribing of thin films with picosecond laser pulses for CIGS solar cells, International Congress on Applications of Lasers & Electro- Optics, ICALEO 2010, Anaheim, California, USA, September 27- 30, 2010. (oral)

[C15] G. Račiukaitis, **P. Gečys**, M. Gedvilas, M. Brikas, B. Voisiat, Ultra-short-pulse lasers in selective ablation of thin films for solar cells and other technical applications, The 3rd international conference „Radiation interaction with material and its use in technologies”, Kaunas, Lithuania, September 20-23, 2010 (invited).

[C16] G. Račiukaitis, **P. Gečys**, M. Gedvilas, Energy coupling localization and selective laser processing in thin-film structures, 7th International Conference on Photo-Excited Processes and Applications, Copenhagen, Denmark, August 16-20, 2010. (oral)

[C17] G. Račiukaitis, E. Stankevičius, **P. Gečys**, M. Gedvilas, C. Bischoff, E. Jäger, U. Umhofer, Laser processing by using diffractive optical laser beam shaping technique, 11th International Symposium on Laser Precision Microfabrication, Stuttgart, Germany, June 7-10, 2010. (oral)

[C18] G. Račiukaitis, **P. Gečys**, R. Trusovas, R. Kondrotas, Picosecond Laser Scribing for Thin-film Solar Cell Manufacturing, Pacific International Conference on Applications of Lasers & Optics, PICALO 2010, Wuhan, China, March 23-25, 2010. (oral)

[C19] G. Račiukaitis, **P. Gečys**, M. Gedvilas, K. Regelskis, B. Voisiat, Selective Ablation of Thin Films with Ultra-Short-Pulse Lasers for Solar Cells and Other Technical Applications, The International High Power Laser Ablation Conference, HPLA 2010, Santa Fe, New Mexico, USA, April 18-22, 2010. (invited)

[C20] G. Račiukaitis, **P.Gečys**, A. Braun, S. Ragnow, H. Schulte-Huxel, A. Wehrmann, M. Ehrhardt, K. Zimmer, Patterning of composite semiconductor films by ultrashort laser pulses: Basics and applications, 10th International Conference on Laser Ablation (COLA 2009) Singapore, November 22-27, 2009. (poster)

[C21] P. Gečys, G. Račiukaitis, A. Braun, S. Ragnow, M. Ehrhardt, K. Zimmer, Ps-laser scribing of CIGS films at different wavelengths, 10th International Conference on Laser Ablation (COLA 2009), Singapore, November 22-27, 2009. (poster)

[C22]G. Račiukaitis, **P.Gečys**, Picosecond-laser structuring of thin films for CIGS solar cells, The 5th International Congress on Laser Advanced Materials Processing (LAMP 2009), Kobe, Japan, 2009. (oral)

[C23] G. Račiukaitis, M. Brikas, **P. Gečys**, M. Gedvilas, Laidininkų formavimas lazeriais plonasluoksnės elektronikos prietaisams/ Laser structuring of electro-conducting layers for thin-film electronic devices,38-oji Lietuvos nac. fizikos konf., Vilnius, birželio 8-10, 2009. (oral)

[C24] **P. Gečys**, G. Račiukaitis, a-Si Plonasluoksnių Saulės Elementų Struktūrinimas Pikosekundiniu Lazeriu /Structuring of a-Si fhin-film solar cells with picosecond laser, 38-oji Lietuvos nac. fizikos konf., Vilnius, birželio 8-10, 2009. (oral)

[C25] G. Račiukaitis, **P. Gečys**, M. Gedvilas, Laser structuring of conducting films on transparent substrates for electronics devices, International Congress on Applications of Lasers & Electro- Optics, ICALEO 2008, Temecula, California, USA, October 20- 24, 2008. (oral)

Contribution to presentations not directly related to the topic of the thesis

[C26] M. Ehrhardt, K. Zimmer, **P. Gečys**, G. Račiukaitis, Laser-induced backside wet etching of transparent materials with picosecond UV laser pulses, 10th International Conference on Laser Ablation (COLA 2009), Singapore, November 22-27, 2009. (poster)

[C27] V. Ulevicius, G. Račiukaitis, **P. Gečys**, S. Kecorius, N. Spirkauskaite, Aerosol particle formation and evolution during laser ablation, NOSA (Nordic Society for Aerosol Research) Aerosol Symposium, Lund, Sweden, November 12-13, 2009.

[C28] V. Dudoitis, V. Ulevičius, G. Račiukaitis, **P.Gečys**, Aerosol particle formation during laser ablation in particle-free ambient air, European Aerosol conference, EAC 2008, Thessaloniki, Greece, 24-29 August, 2008. (poster)

[C29] M. Gedvilas, B. Voisiat, K. Regelskis, **P. Gečys**, Ripple formation by laser irradiation and FEMLAB simulation. 1st Int. School on Laser-surface interactions for new materials production: tailoring structure and properties, Venice, Italy, July 13-20, 2008. (poster)

[C30] G. Račiukaitis, M. Brikas, **P. Gečys**, B. Voisiat, M. Gedvilas, Use of High Repetition Rate and High Power Lasers in Microfabrication: How to Keep the Efficiency High?, 9thInternational Symposium on Laser Precision Microfabrication, LPM 2008, Quebec City, Canada, June 16-20, 2008. (oral)

[C31] G. Račiukaitis, M. Brikas, **P. Gečys**, M. Gedvilas, Accumulation effects in laser ablation of metals with high-repetition rate lasers, SPIE Conference on High-Power Laser Ablation, HPLA 2008, Taos, New Mexico, USA, April 20-24, 2008. (oral)

[C32] K. Regelskis, M. Gedvilas, G. Račiukaitis, **P.Gečys**, Fabrication of gratings by self-organization of thin metal film, The 11th Nordic Conference in Laser Materials Processing, NOLAMP 11, Lappeenranta, Finland, August 20-22, 2007. (oral)

[C33] M. Gedvilas, K. Regelskis, **P. Gečys**, G. Račiukaitis, Savaiminis gardelių formavimasisploname chromo sluoksnyje, apšvitinus jį lazerio impulsais / Formation of gratings by self-organization of chromium thin film under irradiation with laser pulses, 37-oji Lietuvos nacionalinė fizikos konferencija, Vilnius, birželio 11-13, 2007.

[C34] Gedvilas, G. Račiukaitis, K. Regelskis, **P. Gečys**, Formation of gratings by self-organization of chromium thin film on the glass substrate under irradiation with laser pulses, The International Symposium on Laser Precision Microfabrication, LPM 2007, Vienna, Austria, April 24-28, 2007.

1.5 Contributions

1.5.1 Author's contribution

All experimental part of the thesis was performed by the author by consulting with the scientific supervisor. My contribution included:

1. Development and assembly of experimental setups including the systems with 1575 nm, 1064 nm, 532 nm, 355 nm and 266 nm laser wavelengths.
2. Experiment planning and realization.
3. Sample characterization after laser scribing experiments with listed techniques: optical microscopy, scanning electron microscopy with X-ray energy dispersion spectrometer, Raman spectroscopy, solar cell efficiency measurements.
4. Experimental data analysis, writing scientific publications and presentation of the results at conferences.

1.5.2 Coauthors' contribution

The solar cell electrical characterization with LIT (Lock-in thermography) and LBIC (Laser-beam-induced current measurements) techniques was performed by the staff of the solar cell vendor Solarion AG.

First SEM (Scanning electron microscopy) together with EDS (X-ray energy dispersion spectroscopy) analysis was performed by Dr. A. Selskis from the Institute of Chemistry of the Center for Physical Sciences and Technology in Vilnius.

Modeling work was done by S. Grubinskas under supervision of Dr. M. Gedvilas and author of the thesis.

2 LITERATURE REVIEW

2.1 Market review

2.1.1 Manufacturing capacity and cost

Over the past decade photovoltaics continued to be one of the fastest growing industries with growth rates well beyond 40 % per year. This growth is driven not only by the progress in materials and processing technology, but also by the market support programs in an increasing number of countries around the world [8,17]. In 2010, the PV production reached 23.5 GW representing a doubling of production compared to 2009. The world-wide new investments into the renewable energy and energy efficiency sectors increased to a new record of € 187 billion, by 30% from 2009. The most rapid growth in the annual production over the last five years was observed in Asia, where China and Taiwan together now account for almost 60% of the world-wide production (see Fig. 1) and will continue to grow in the future (see Fig. 2) [8].

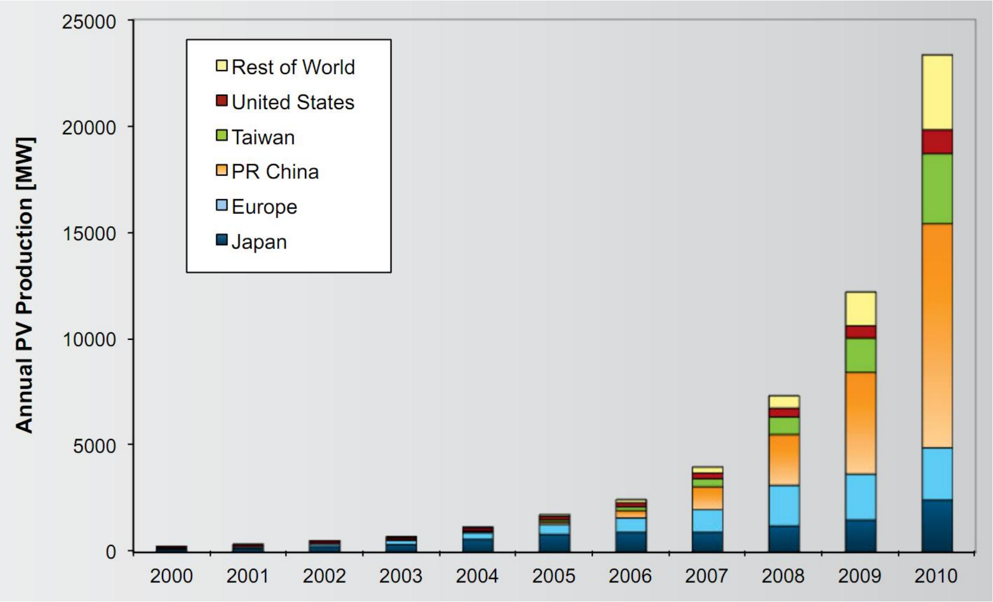

Fig. 1 World PV cell/module production from 2000 to 2010 [8].

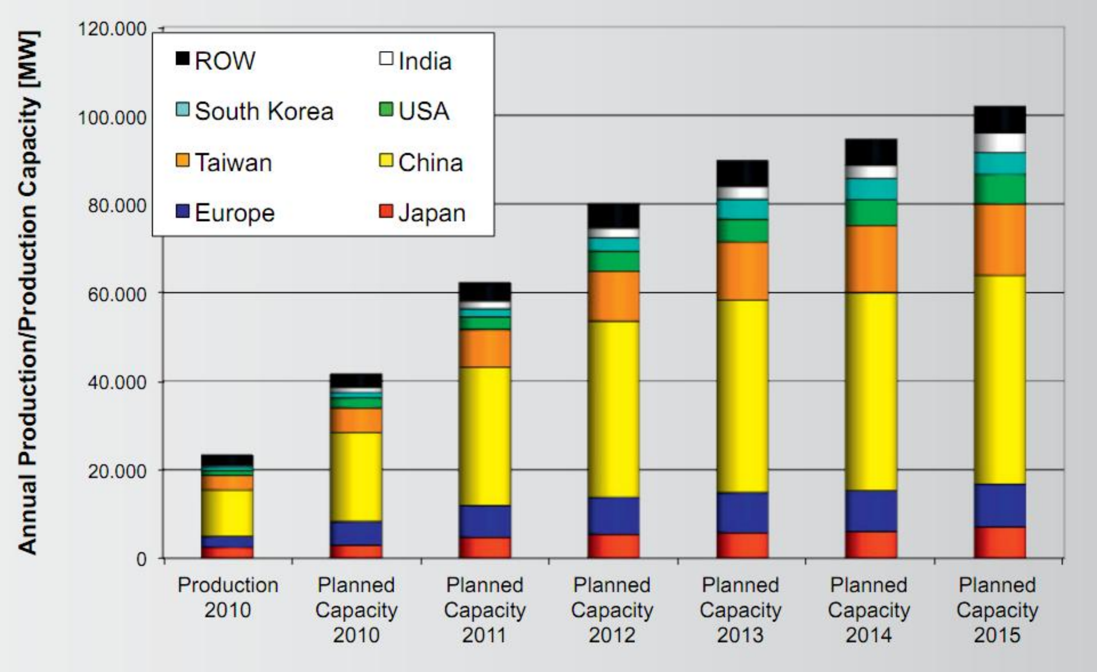

Fig. 2 World-wide PV production capacity in 2010 and forecast until 2015 [8].

The wafer-based silicon solar cells are still the main technology and had around 85% market shares in 2010 [8], although thin-film based PV cells emerge to the market due potential in lowering production cost (see Fig. 3).

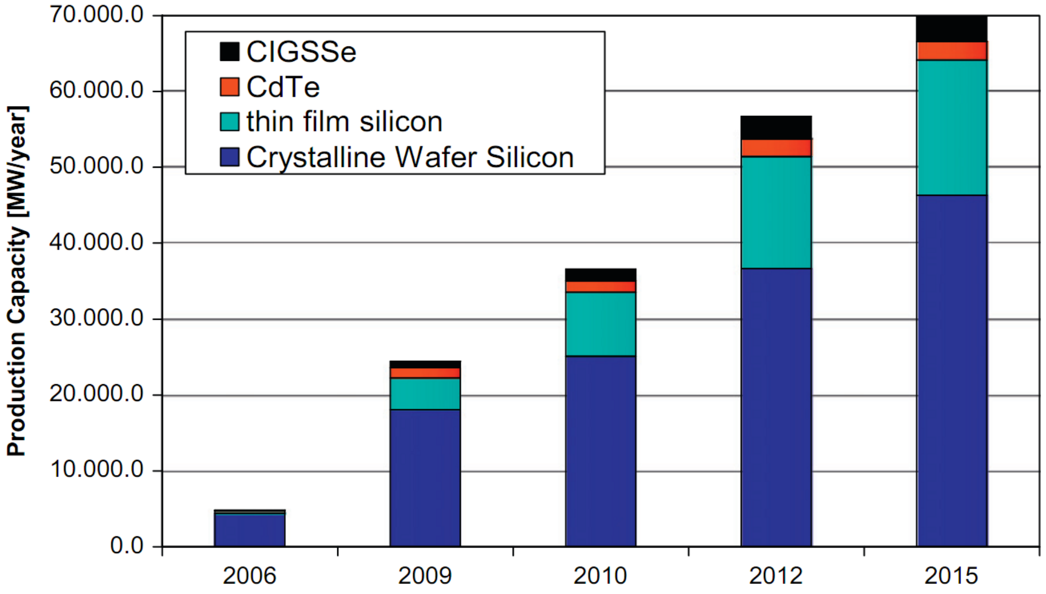

Fig. 3 Actual and planned PV production capacities of different solar cell technologies [8,17].

The largest thin-film market share belongs to the a-Si based PV technologies, although CdTe and CIGS based thin-film photovoltaics emerge to the market. For the CIGS technology, it shows the highest efficiencies reached in the thin-film segment (see section 2.1.2), although further development of this technology depends on the adaptation to the cost-effective large-scale manufacturing processes.

The cost of PV cells tends to decrease while manufacturing capacity increases as well as new modern manufacturing processes are developed to increase the efficiency of the PV devices. The goal of PV industry is to achieve sustainable manufacturing cost less than 1\$/W_p. Price reduction of photo-electricity will promote higher application possibilities worldwide and further development. For the CdTe thin-film solar modules, manufacturing costs of the First Solar company have already dropped down to 0.76 \$/W_p and their goal is to reduce to 0.55\$/W_p by 2014 [18]. The same trends could be observed for other PV technologies such as CIGS, TF-Si (thin-film), mc-Si, and others (see Fig. 4).

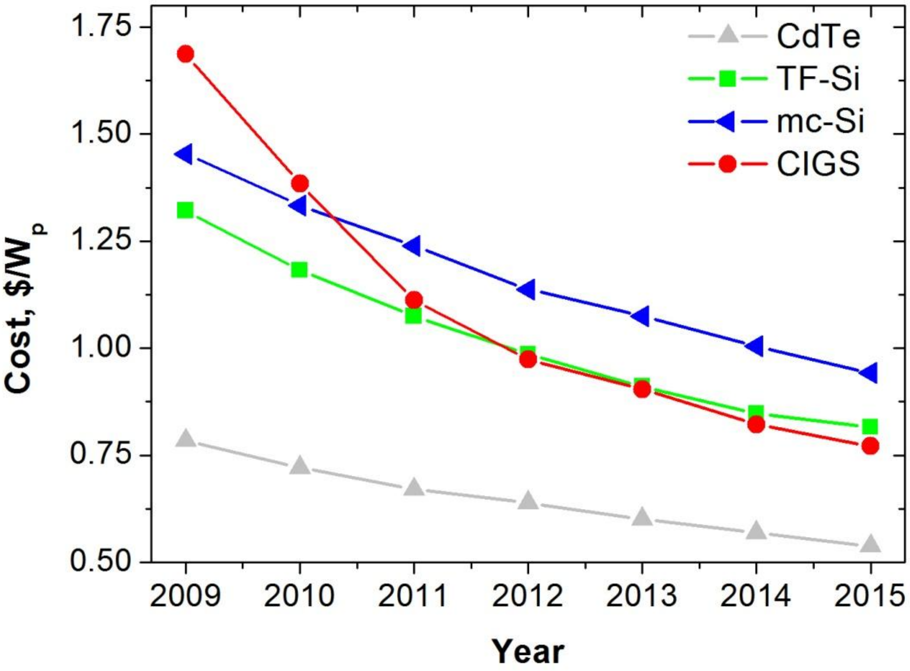

Fig. 4 Trends in manufacturing cost for the different PV technologies [19].

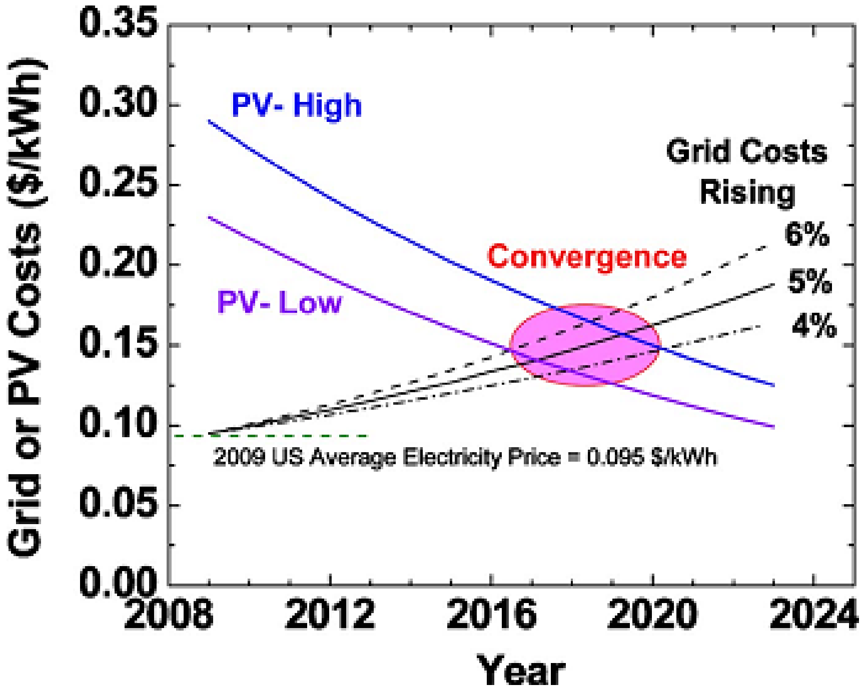

Fig. 5 Projected convergence of the cost of electricity produced by PV and the conventional grid prices [20].

Fig. 5 shows the forecasted price per kWh evolution until 2025. A further decrease in manufacturing costs of the PV devices and the efficiency increase will lead to cheaper solar electricity which will be able to compete with conventional grid prices.

2.1.2 Solar cell efficiency

The highest confirmed module and cell efficiencies are shown in Table 1 and Table 2. Usually PV modules show lower conversion efficiencies compared to those of single cells due to energy losses in the series interconnect wirings and absorption in the lamination layer which is used to protect the cells from the environmental influence. All modules presented in Table 1 are commercially available on the market. Table 2 presents the record efficiencies of the commercial cells and R&D products. The CIGS solar cells show the highest module and R&D cell performance (15.7 % and 20.3 %) in the thin-film segment (see Table 2) and the performance of their closest competitor CdTe reaches only 12.8 %. The overall record efficiencies of the solar cells belong to the multi-junction devices (GalnP/GaAs/GalnNAs) with efficiencies up to 43.5 % [21] which normally are used with solar concentrators.

Table 1 Confirmed module efficiencies measured under the global AM1.5 spectrum (1000 W/m^2) at a cell temperature of 25°C (2011) [21].

Classification	Eff., (%)	Description
Si (crystalline)	22.9±0.6	UNSW/Gochermann
Si (large crystalline)	21.4±0.6	SunPower
Si (multi-crystalline)	17.8±0.4	Q-cells (60 serial cells)
Si (thin-film polycrystalline)	8.2±0.2	Pacific Solar (1–2μm on glass)
CIGS	**15.7±0.5**	**Miasole**
CIGSS (Cd free)	**13.5±0.7**	**Showa Shell**
CdTe	12.8±0.4	PrimeStar monolithic
a-Si/a-SiGe/a-SiGe	10.4±0.5	USSC

Table 2 Confirmed commercial and R&D cell and sub-module efficiencies measured under the global AM1.5 spectrum (1000 W/m^2) at 25°C (2011) [21].

Classification	Eff, (%)	Description
Silicon		
Si (crystalline)	25.0 ±0.5	UNSWPERL
Si (multi-crystalline)	20.4±0.5	FhG-ISE
Si (thin-film transfer)	19.1 ±0.4	ISFH (43 μm thick)
Si (thin-film submodule)	10.5±0.3	CSG Solar (1-2 μm on glass; 20 cells)
III-V cells		
GaAs (thin-film)	28.1 ±0.8	Alta Devices
GaAs (multi-crystalline)	18.4±0.8	RTI, Ge substrate
InP (crystalline)	22.1 ±0.7	Spire, epitaxial
Thin film chalcogenide		
CIGS (cell)	**20.3 ±0.6**	**ZSW Stuttgart, CIGS on glass**
CIGS (submodule)	**16.7± 0.4**	**U. Uppsala, 4 serial cells**
CdTe (cell)	16.7 ±0.5	NREL, mesa on glass
Amorphous, nano-crystalline Si		
Si (amorphous)	10.1 ±0.3	Oerlikon Solar Lab, Neuchatel
Si (nano-crystalline)	10.1 ±0.2	Kaneka (2 μm on glass)

Photochemica		
Dye-sensitized	10.9±0.3	Sharp
Dye-sensitized (sub-module)	9.9±0.4	Sony, eight parallel cells
Organic		
Organic polymer	8.3±0.3	Konarka
Organic (sub-module)	3.5±0.3	Solarmer
Multi-junction devices		
GalnP/GaAs/Ge	32.0±1.5	Spectrolab (monolithic)
GaAs/CIS (thin-film)	25.8±1.3	Kopin/Boeing (four terminal)
a-Si/nc-Si/nc-Si (thin film)	12.4±0.7	United Solar
a-Si/nc-Si (thin-film cell)	11.9± 0.8	Oerlikon Solar Lab, Neuchatel
a-Si/nc-Si (thin-film sub-module)	11.7±0.4	Kaneka (thin-film)
Concentrator multi-junction devices		
GalnP/GaAs/GalnNAs	**43.5±2.6**	**Solar Junction, triple cell**
GaInP/GaInAs/Ge	**41.6±2.5**	**Spectrolab, lattice-matched**
GaInP/GaAs; GaInAsP/GaInAs	**38.5±1.9**	**DuPont et al., split spectrum**
Organic (two-cell tandem)	8.3 ±0.3	Heliatek

2.1.3 Solar energy in 2011

Despite large investments to the PV industry and cost reduction in the solar cell module production, the solar electricity cannot compete with conventional grid electricity prices yet. A lot of effort is made to increase the share of renewable energy in the overall electricity production worldwide in order to reduce CO_2 emission. Government support is widely used to promote photovoltaics development and installations. The support is arranged by investment subsidy or the feed-in tariffs (see Table 3). The support mechanisms differ depending on the country. In northern Europe countries, the support is greater due to the lower sun irradiance and lower electricity production by the modules of the same power compared to the southern countries.

Table 3 Support mechanisms for photovoltaics in a few Europe countries in 2011 [8,22].

	€/kWh	comments
Denmark	Price for green electricity (bonus) (0.08 €/kWh) for 10 years, then 10 more years (0.04€/kWh)	
Estonia	0.054 bonus	
Finland	investment subsidy up to 40% and tax/production subsidy	
France	0.46-0.12	Depending on size
Germany	0.287-0.216	Depending on size
Greece	0.419-0.373	Depending on size
Italy	0.387-0.261	Depending on size and time of the year
Latvia	0.101	For ten years
Lithuania	**0.472 (1.63 Lt/kWh)**	**Less than 100kW**
	0.452 (1.56 Lt/kWh)	**From 100kW to 1MW**
	0.347 (1.51 Lt/kWh)	**From 1MW**
Poland	No specific PV program	
Spain	0.289-0.204	Depending on size
Sweden	60% of the eligible costs	

The average PV electricity production in different European and African countries is shown in Fig. 6. For example, the average electricity production per year for the 1 kWp PV system is about 880 kWh in Lithuania, although in Spain it could reach about 1400 kWh per year [23]. Taking into account different feed-in tariffs in these countries the annual income from 1 kWp system should be the same and equals to about 400 €/Year. The average price for the 1 kWp house hold grid tie solar electric systems in 2011 were about 1500-3000 €/Wp (2000-4000 $/Wp) including solar panels, inverter and other electrical components [24-27]. Taking this into account, the pay-back time for the solar power system of 10-12 years could be fulfilled even in the northern European countries such as Lithuania if the feed-in tariffs stay constant during this period.

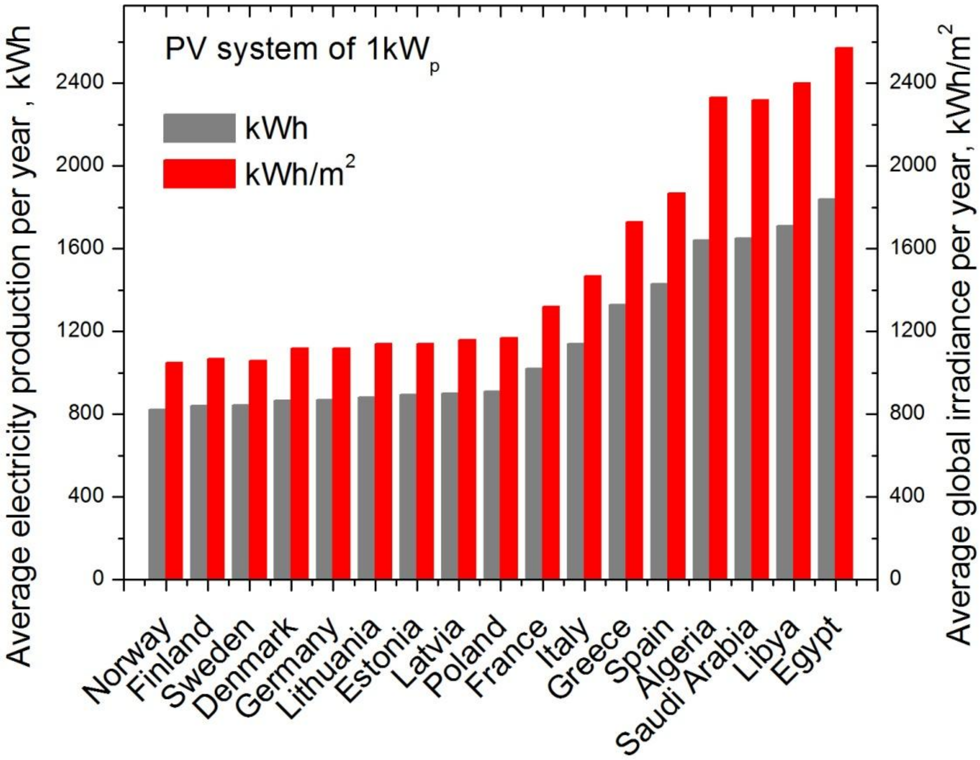

Fig. 6 Average electricity production and global irradiance for the different European and African countries. The nominal power of the optimized PV system: 1 kW (crystalline silicon) [23].

2.2 Solar spectrum

The quantity of light absorbed by a semiconductor depends not only on its band-gap energy, but also on the spectrum of the incoming light (i.e. the energy distribution of the incident light as a function of wavelength). Fig. 7 shows the spectrum of light emitted by the sun (which can be considered as a black body at 5778 K), as well as the spectrum of sunlight received on the Earth's surface, both outside the atmosphere and at the ground level. The difference between the last two is due to the path through the earth's atmosphere, which attenuates the solar spectrum (Rayleigh scattering, scattering by aerosols, absorption by the constituent gases of the atmosphere: UV absorption by ozone, infrared absorption by water vapor, etc.) [28].

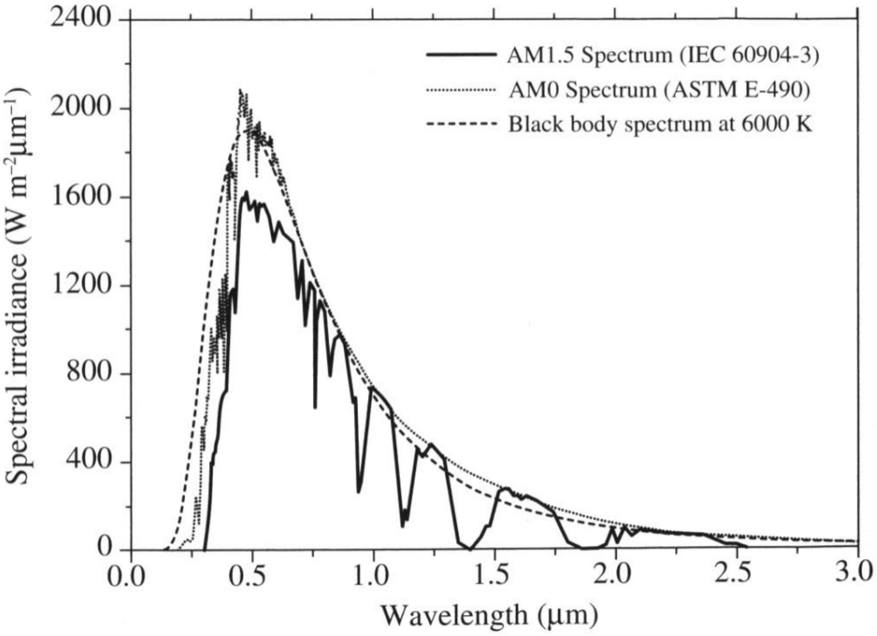

Fig. 7 Spectral distribution of the solar emission on the Earth's surface (AM 1.5) and outside the atmosphere (AM 0); The standardized spectra are given according to standards IEC 60904-3 (for AM 1.5) and ASTM E-490 (for AM 0) [28].

This attenuation effect is characterized by the "Air Mass" coefficient AM=1/cos(α), where α is the angle between the solar ray and a vertical line (see Fig. 8). Thus, AM 0 corresponds to the solar spectrum outside the atmosphere and AM 1 to solar spectrum on the earth's surface when the sun is directly (vertically) overhead [28].

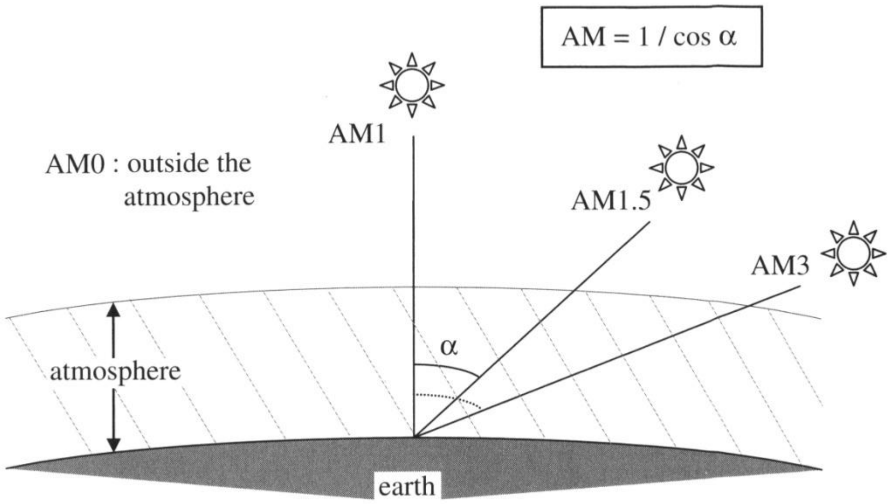

Fig. 8 Diagram illustrating the definition of AM 0, AM 1.5 and AM 3. A is the angle of incidence of the sunlight, defined as the angle between a vertical line and the incident sunrays [28].

AM 1.5 (i.e α≈48.2°) is considered to be the "standard" value for testing and specifications in terrestrial applications of the solar cells, as it corresponds to a "reasonable average value" of the air mass through which the incoming sunlight passes. Note that not only the spectrum is defined by this coefficient, but also the intensity of incoming sunlight. However, the intensity is generally normalized to 1000 W/m^2 in order to calibrate the efficiency of photovoltaic systems [28].

2.3 Thin-film CIGS solar cells

Current trends suggest that solar energy will play an important role in the future energy production [3]. Silicon has been and remains the traditional solar cell material of choice. Although silicon is a highly abundant material, it requires an energy intensive process to purify and crystallize. Furthermore, installations of silicon cells require heavy constructions, which reduce residential applications [6,10].

Recently, commercial interest has started to shift towards the thin-film cells [4]. Savings in material consumption, manufacturing time and weight of devices are driving an interest in the thin-film cells. $Cu(In,Ga)Se_2$ (CIGS) is one of the most promising semiconductors for the absorber layer of thin-film solar cells [5,6]. The conversion efficiency of such cells on glass substrates has already overcame 20% on glass [7] and 18% on flexible substrates [29]. Chalcopyrite-based solar modules are uniquely combining advantages of the thin-film technology with the efficiency and stability of conventional crystalline silicon cells [6]. The copper indium gallium selenide (CIGS) solar cells have the highest efficiency among thin-film technologies.

Even today the chalcopyrite-based solar modules can compete with the Si wafer-based modules on the market. The thin-film CIGS solar cells application area extends from the building integrated photovoltaic (BIPV) to industrial applications. The unique design of flexible modules and light weight makes possible integration on complex surfaces, car roofs, portable devices and other areas.

CIGS solar cells also attract considerable interest in space applications due to their two main advantages. It offers specific power up to 919W/kg, the highest for any solar cell [30]. The CIGS cells are also superior to GaAs cells in radiation hardness [31]. Moreover, the flexibility of these cells allows novel storage and deployment options [30].

2.3.1 Basic CIGS solar cell structure

The most common device structure for the CIGS solar cells is shown in Fig. 9. Glass of a few milimeters thick is commonly used as a substrate, however, many companies are also looking for lighter, thinner and more flexible substrates such as polyimide or metal foils [32]. The 0.5 µm-thick molybdenum layer is used as a back-contact with the 1-2 µm thickness p–type CIGS absorber layer on its top. The 10-50 nm n-type CdS buffer layer is used to form the p-n junction. Less than 1 µm-thick TCO (ZnO:Al or ITO) layer is used as a front-contact.

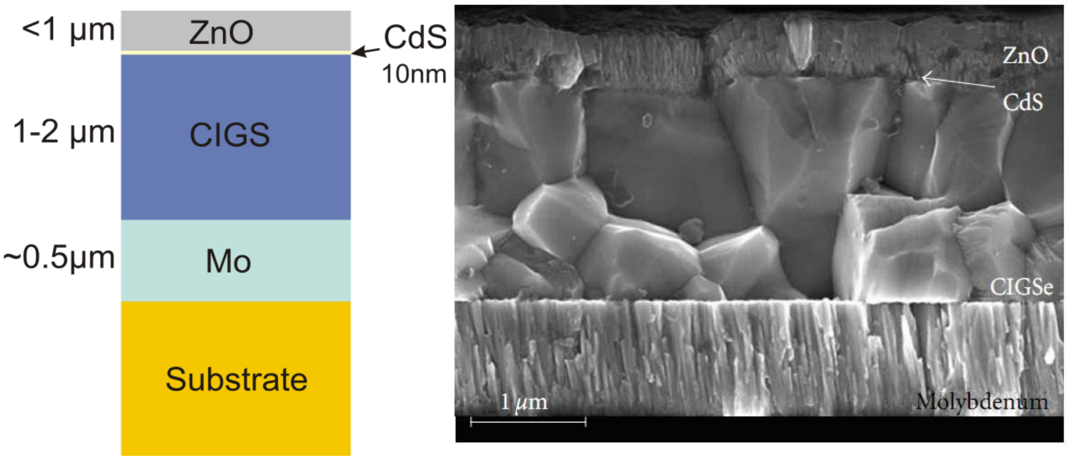

Fig. 9 Structure of thin-film CIGS solar cell [6].

The most promising flexible substrates are metal and polyimide (PI) films. The stability under mechanical stress of CIGS solar cells on PI has been tested, proving a high degree of flexibility, although the maximum applicable temperature for PI is significantly lower, typically below 500°C, than for metal foils and glass substrates, which can withstand temperatures up to 600°C or even higher [29]. For this reason, the flexible PV devices demonstrated lower conversion efficiencies due to higher defect concentration in the CIGS layer in low temperature deposition processes.

Molybdenum (Mo) emerged as the dominant choice for the back-contact due to its relative stability at the processing temperature, resistance to alloying with Cu and In, and its low contact resistance to CIGS [6].

The most successful technique for deposition of CIGS absorber layers for the highest-efficiency cells is the simultaneous co-evaporation [33] of the constituent elements from multiple sources in single processes where Se is offered in excess during the whole deposition process [6]. CIGS semiconductor is considered to have a direct band-gap as the maximum of the valance band corresponds to the minimum of the conduction band. State-of-the-art $CuIn_xGa_{1-x}Se_2$ (CIGS) devices generally have an average band-gap energy of around 1.2 eV, corresponding to a relative gallium content of $x=[Ga]/([Ga]+[In])= 0.3-0.4$ [29], although variation of the band gap energy is possible by varying Ga and In content in the absorber layer.

The CdS layer for the high-efficiency CIGS cells is generally grown by a chemical bath deposition (CBD), which is a low-cost, large-area process [6]. The role of the CdS buffer layer is twofold: it affects both the electrical properties of the junction and protects the junction against chemical reactions and mechanical damage. From the electric point of view, the CdS layer optimizes the band alignment of the device [34,35] and builds a sufficiently wide depletion layer that minimizes tunneling and establishes a higher contact potential that allows a higher value of the open-circuit voltage [6,35].

For the front-contact, the CIGS solar cells employ either tin-doped In_2O_3 (In_2O_3:Sn, ITO) [36] or, more frequently, RF-sputtered Al-doped ZnO. A combination of an intrinsic and doped ZnO layer is commonly used because this double layer yields consistently higher solar cell efficiencies [6].

2.3.2 Principle of solar cell operation

When light illuminates a solar cell, photons are absorbed by the semiconductor material and pairs of free electrons are created. However, in order to be absorbed, the photon must have energy higher or at least equal to the band-gap energy E_g of the semiconductor. The band-gap energy is the difference in energy levels between the lowest energy level of the conduction band (E_c) and the highest energy level of the valence band (E_v) [28].

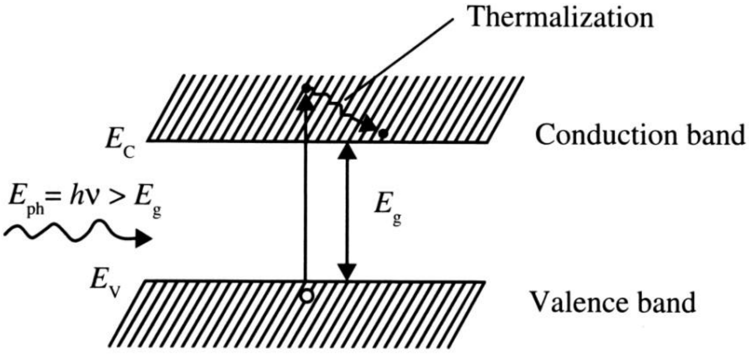

Fig. 10 Absorption of photons when $E_{ph}>E_g$ [28].

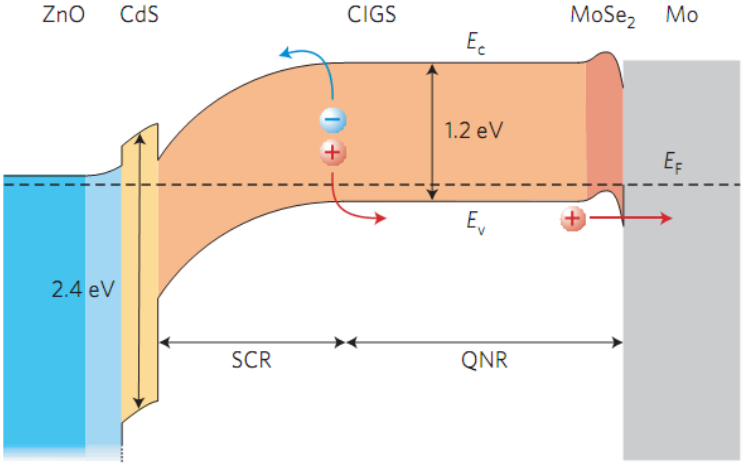

Fig. 11 Schematic band diagram of a CIGS solar cell under zero-bias voltage condition [29].

For the PV device to generate the current, the photon generated electron-hole pairs have to be separated [28]. Fig. 11 shows a schematic band diagram of a CIGS solar cell under the zero-bias voltage condition. The p-n junction is formed between the p-type CIGS absorber layer and the n-type CdS and ZnO layers, which causes bending of the valence and conduction bands. The CIGS layer divides into a majority charge carrier depleted space charge region (SCR) and a quasi-neutral region (QNR). The incoming light with energy higher than the CIGS band-gap is mostly absorbed within the first micrometer of the absorber layer, where it creates electron-hole pairs that are spatially separated by the internal electric field of the p-n junction [29].

2.3.3 Electrical properties of CIGS solar cells

2.3.3.1 *J(V)* characteristics

A solar cell is basically a diode. The simplest equivalent circuit for an “ideal” solar cell is shown below.

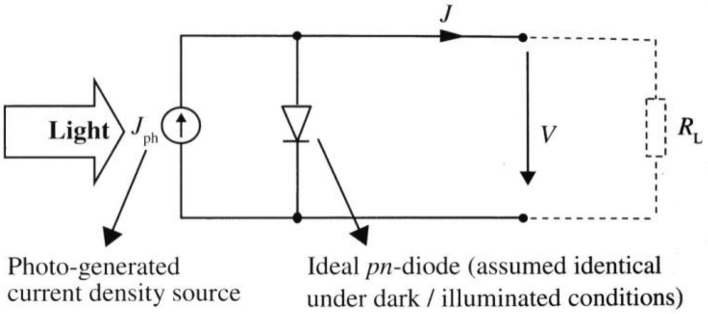

Fig. 12 Simplest equivalent circuit for an “ideal” solar cell; an external load resistance R_L has also been drawn [28].

When no light is applied (dark conditions), the relation between the current density J_{dark} flowing through the device and the voltage V applied to its boundaries is given by the following equation:

$$J_{dark} = J_0\left[\exp\left(\frac{qV}{nkT}\right)-1\right], \tag{1}$$

where: q=1.6022x10^{-19} C is the elementary charge, k=1.3870x10^{-23} J/K is the Boltzmann constant, T [K] is the absolute temperature, J_0 is the reverse saturation current density of the diode (see Eq. (2)), n is the “ideality factor” of the diode.

The value of n lies basically within the range between 1 and 2. For crystalline silicon, n=1 when the diffusion current is dominating, whereas n=2 when the generation/recombination current dominates [28]. For the CIGS based solar cells, the n value is from 1.35 to 1.62 [37].

Martin Green [38] has proposed a simple empirical relation that can be used reasonably to estimate the minimal value of the reverse saturation current density:

$$J_0 = 1.5\times10^8 \exp\left(\frac{-E_g}{kT}\right) \quad \text{in}\left[\frac{\text{mA}}{\text{cm}^2}\right], \tag{2}$$

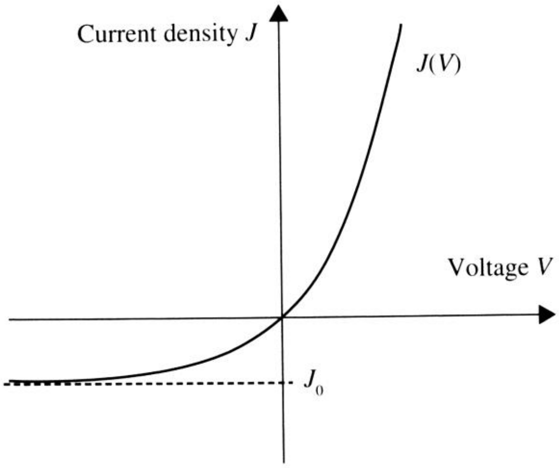

Fig. 13 Typical dark $J(V)$ characteristic for a solar cell device. J_0 is the reverse saturation current density [28].

As soon as light hits the solar cell, the photo-generated current density J_{ph} will be superimposed on the dark current density J_{dark}. Equation (1) then becomes:

$$J_{illum} = J_{ph} - J_{dark} = J_{ph} - J_0\left[\exp\left(\frac{qV}{nKT}\right) - 1\right], \tag{3}$$

There is no negative sign in the front of $J_{dark,}$ because the photon-generated current and the diode forward current flow in opposite directions. The photon-generated current is composed of holes flowing to the p-side and electrons flowing to the n-side, whereas in the forward operation of a (dark) diode, the flow of carriers is just the opposite. Equation (3) implicitly assumes that the photo-generated current and the dark current of the diode can simply be additively superimposed, without any additional terms [28].

According to the superposition principle, the curve for illuminated conditions is exactly the same as that for dark conditions, but it is simply shifted down by the value J_{ph} (see Fig. 14). The point "MPP" is the "maximum Power point", i.e. the operating at which the solar cell gives maximum power to the attached load [28].

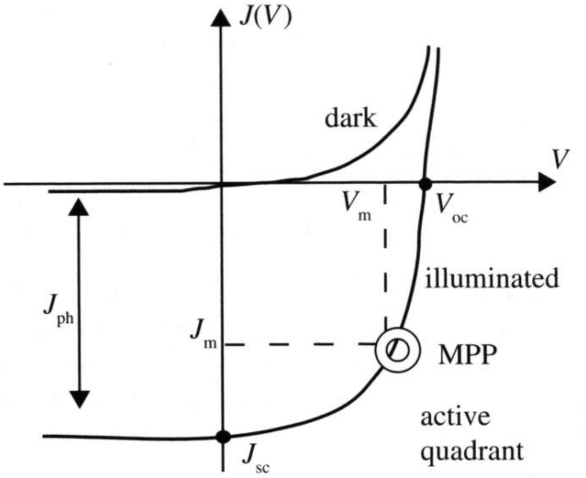

Fig. 14 *J(V)* characteristics of an "ideal" solar cell (*pn*-diode) under dark and illuminated conditions.

In reality, other circuit elements have to be added to the basic solar cell equivalent circuit. These are the series resistance R_S and the parallel resistance R_P (see Fig. 15). The series resistance R_S represents thereby ohmic resistance in the connection wires up to the solar cell and also other ohmic resistances within the solar cell, between the external connection point and the actual active device. The parallel resistance R_P is employed not only to designate actual ohmic shunts, but also, and mainly, to symbolize the recombination losses within the solar cell [28].

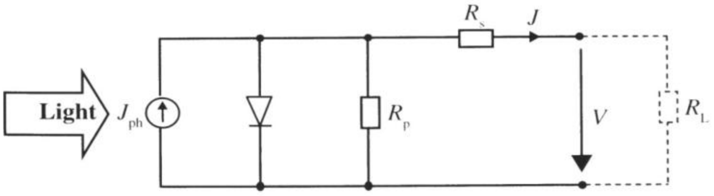

Fig. 15 Universally used equivalent circuit for a solar cell [28].

2.3.3.2 Basic solar cell parameters J_{sc}, V_{oc}, FF, η

The short-circuit current is the current through the solar cell when the voltage across the solar cell is zero (i.e., when the solar cell is short-circuited). In the short-circuit condition when no voltage is applied (V=0), equation (3) gives in the case of an ideal illuminated diode (see Fig. 14):

$$J_{sc} = J_{ph}, \tag{4}$$

In real solar cell R_p represents both the carrier recombination and ohmic shunts which will decrease J_{ph} and the real J_{sc} value will be lower.

The open-circuit voltage, V_{oc}, is the maximum voltage available from a solar cell, and this occurs at the zero current. The open-circuit voltage corresponds to the amount of forward bias on the solar cell due to the bias of the solar cell junction with the light-generated current. The open-circuit voltage V_{oc} can be found by setting J_{illum}=0 in (3). This gives an equation [28]:

$$V_{oc} = \frac{nkT}{q}\left(\frac{J_{ph}}{J_0}+1\right) \approx \frac{kT}{q}\ln\left(\frac{J_{ph}}{J_{00}}\right)+\frac{E_g}{q}, \tag{5}$$

where:

$$J_{00} = J_{00}^{Green} = 1.5\times10^{8}[\mathrm{mA/cm^2}]. \tag{6}$$

The V_{oc} value depends on the current density generated by photons (illumination level), temperature and the band-gap of the semiconductor material. In the real solar cells, R_s should be taken into account as well, because it reduces the overall generated voltage.

The short-circuit current and the open-circuit voltage are the maximum current and voltage available from a solar cell, respectively. However, at both of these operating points, the power from the solar cell is equal to zero. The "fill factor", more commonly known by its abbreviation "*FF*", is a parameter which, in conjunction with V_{oc} and I_{sc}, determines the maximum power available from a solar cell. The *FF* is defined as the ratio of the maximum power from the solar cell to the product of V_{oc} and I_{sc}.

$$FF = \frac{V_m \times J_m}{V_{oc} \times J_{sc}}, \tag{7}$$

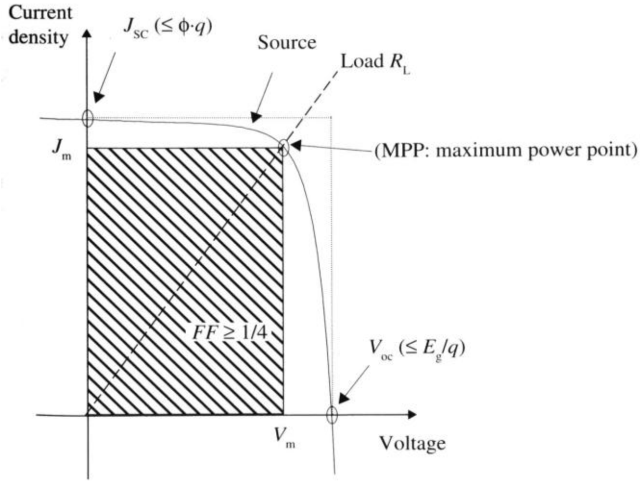

Fig. 16 Fourth quadrant of the solar cell *J(V)* characteristics. MMP represents maximum power point [28].

The overall energy conversion efficiency η of the solar cell is equal to the ratio between the electrical output power P_{out} (at the maximum power point) and the illumination power P_{illum}.

$$\eta = \frac{P_{out}}{P_{illum}}, \tag{8}$$

where:

$$P_{out} = V_m \times J_m; \quad P_{illum} = s \times \phi. \tag{9}$$

s is the active area of a solar cell [m^2], ϕ in the sun irradiation [W/m^2].

2.4 Interconnects in large-area thin-film solar cells

The a-Si thin-film based solar industry today mainly produces the Gen 5 panels with dimensions of 1100x1300 mm. The upcoming Gen 8.5 will move to 2200x2600 mm panels [11]. For the CIGS solar panels the dimensions might differ depending on the manufacturer, although the nominal module area is about 1-1.5 m^2. The sunlight falls on the earth's surface with an intensity of about 1 kW/m^2, so that 1 m^2 solar cell operating at 10 % efficiency is capable of producing 100 W of electrical energy. The electrical current from each PV cell scales with its area, but generated voltage is independent of the cell area. The CIGS single cells generate voltage between 0.6 and 1.2 V depending on the band gap of the ternary semiconductor and the adjusted layer producing p-n junction [39]. As an example, a CIGS cell with the efficiency of 10 % and the area of 1 m^2 producing 100 W of power and operating at 0.6 V voltage would create the current of about 160 A. Such high current will result heat release at the contacts and the current-carrying bus lines increasing energy losses and reducing the solar cell efficiency.

To maintain the module efficiency, the large scale device should be divided into smaller cells connected in series in order to increase the generated voltage and maintain the single cell efficiency over a large area. The same 1 m^2 of thin-film solar module with 100 integrated cells would produce only 1.6 A current at 60 V but yields the same power as the large cell.

To form a monolithically integrated series interconnects between separated cells, the isolation lines have to be scribed at different stages of solar cell production (see Fig. 17). These narrow strip-shaped cells should span the entire width of the panel (1-2 m) with the period of 5-10 mm to limit the current [11]. The interconnect area should be in the range of 100-500 μm with single scribe widths of 50 μm [11,40].

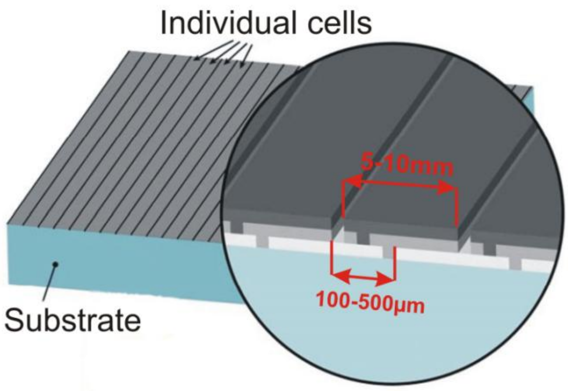

Fig. 17 Thin-film solar panel fabricated as a large monolithic sheet which is patterned into a large number of individual strip-shaped solar cells, electrically connected in series [11].

2.4.1 Interconnect architectures

In case of interconnect formation, there are standard layer scribing processes performed at different stages of the solar cell production line. The P1 process starts with patterning of the Mo back contact, which defines the number of cells and their width along a panel. The P2 process is used to locally remove the CIGS absorber by a mechanical or laser tool, and that allows the connection of the ZnO front-contact of the neighboring cell with the Mo back-contact of the patterned cell. Separation of individual cells after the deposition of the conductive and transparent ZnO window layer is defined as P3 process [10]. The P4 process is defined as a border deletion and is used to scribe completely through the solar cell structure to reach underneath substrate mainly in perpendicular to other scribes direction.

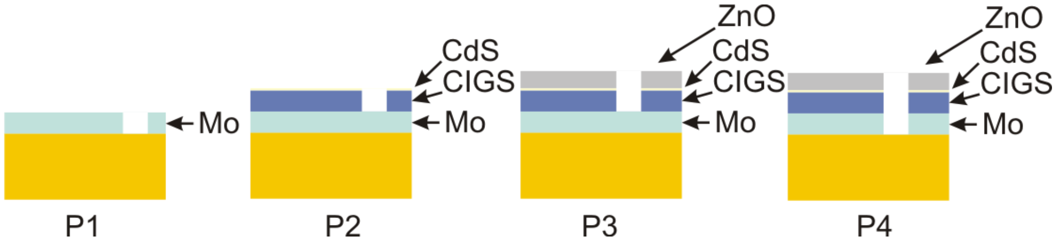

Fig. 18 The P1, P2, P3 and P4 process illustration.

There are three main interconnect architectures used for serial interconnections (see Fig. 19). These architectures are realized by different patterning processes of the thin layers. In case (a) the interconnect is formed by scribing P1, P2 and P3 patterns at the different stages of the cell production line. In case (b) the P2 scribing process is changed to the micro-weld formation. The interconnect in case (c) is formed by P3 and P4 patterning and ink-jet printing of isolating and conductive adhesives.

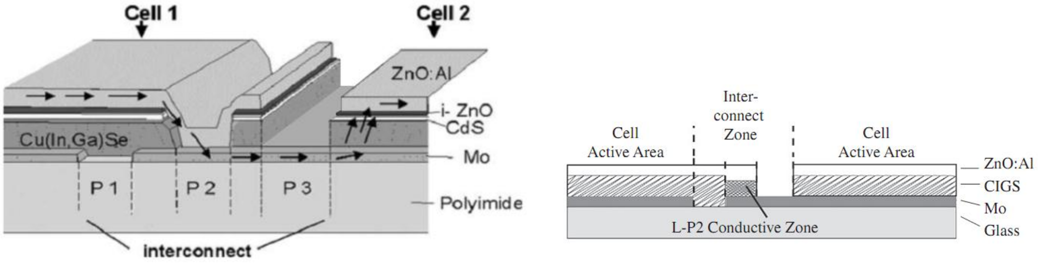

(a) Interconnect formed by standard P1, P2, P3 scribing.

(b) Interconnect formed by P2 microvelding.

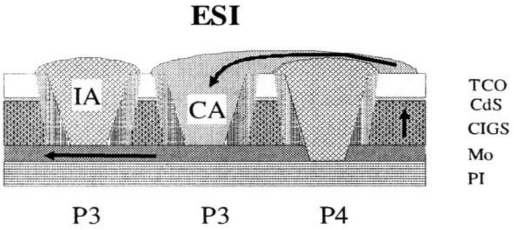

(c) Interconect formed by P3, P4 scribing.

Fig. 19 Different interconnect architectures.

2.4.2 Laser treatment of thin-film solar cells

Laser processing offers a ‘non-contact’ means of scribing, drilling, and melting specific materials used within production line steps for crystalline-silicon (c-Si) and thin-film manufacturing. Non-contact techniques enable the key road-map drivers in cell and panel manufacturing today to increase yield levels by reducing the bulk micro-crack formation, and to combine this with high throughput. Compared to other technologies (plasma/chemical etching, screen printing, and mechanical cutting), laser processing offers specific advantages such as ‘green‘ equipment types, low cost-of-ownership, and increased micromachining quality [9]. Lasers as industrial tools were used in manufacturing for a few decades and proved to be a reliable technique for mass production applications.

As c-Si based solar cells have been dominating on the solar cell market and most of laser applications have been developed for this particular type of cells, although in some thin-film applications lasers play an important role in manufacturing processes. In Table 4 laser applications in modern thin-film solar cell industry are listed.

Table 4 Laser applications within thin-film solar industry [9].

		Production status		
		Widespread production	Partially adopted	R&D or pilot-line
Thin-film	Scribing (P1, P2, P3)	✓		
	Border deletion (P4)		✓	
	Glass cutting		✓	
	Crystallization			✓
	Pulsed laser deposition			✓
	Sintering			✓
	Isolation of shunted regions			✓

Laser scribing is the most developed technique for the thin-film solar cells manufacturing which is widely used by many solar cell companies. Border deletion (isolation) is another process which is partially adopted today although it will play an important role in the future laser applications. Such processes as glass cutting, material crystallization, pulsed laser deposition and sintering are under development to make the effective low-cost PV devices in the future.

2.4.2.1 Laser scribing and interconnects formation

Lasers are the technology of choice for these processes, delivering the desired combination of high throughput and narrow, clean scribes [11]. Accuracy in the ablation depth, layer selectivity and a high scribing speed are required for the efficient and low-cost production of solar cells of this type. The laser scribing rate has to be in the range of 2 m/s. Lasers are the preferred technology type for selective removing thin films of materials [41] making this technique dominant in the thin-film solar cell manufacturing.

Although the interconnect formation consists of three scribing processes P1, P2 and P3, depending on the solar cell technology (CIGS, CdTe or a-Si) and the design, these scribing processes could have different approach.

In the standard P1 process, the laser scribing is used for all types of solar cells in mass production today for separation of the electro-conductive film into contact pads. The P2 and P3 formation with lasers is used only where the back-side scribing could be applied (a-Si or CdTe solar cells on glass substrates). No laser scribing process has been developed yet for the P2 and P3 stage scribing in the CIGS thin-film solar cell structure. The scribing is done with mechanical tools today, although there is a lot of effort to adapt laser scribing technology for these processes in mass production.

2.4.2.2 Serial interconnect formation by wavelength selective back-side P1, P2 and P3 scribing

In case of the a-Si thin-film solar cells based on glass substrates, the laser scribing can be arranged through the glass side by the so-called material lift-off process. Instead of melting, vaporizing or atomizing all the target material, the laser beam vaporizes a small amount of material at the film-substrate interface, removing the overlaying layers entirely by the micro-explosive effect [11]. This minimizes thermal effects, increases the layer selectivity and the process efficiency because the required laser power for the material removal is lower compared to the direct laser ablation. Careful selection of the laser wavelength automatically provides material selectivity, eliminating the cost and complexity of implementing the active depth control [11,42] and makes possible the use of the nanosecond range laser pulses.

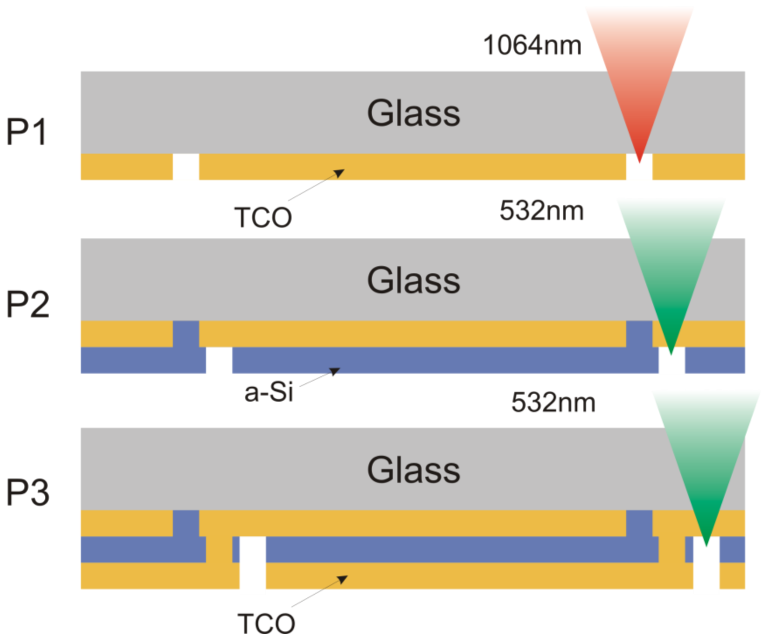

Fig. 20 Series interconnect formation in the thin-films solar cells on the glass substrate. P1: back-contact formation, P2: back-contact exposure to strip a-Si layer, P3: top-contact formation.

The series interconnect formation starts with the P1 type laser scribe after TCO back-contact is deposited on the glass substrate. The purpose of P1 is to completely cut through the TCO, thereby defining one edge of each individual cell. P1 needs a laser wavelength that is transparent for a glass but is strongly absorbed by the TCO. The use of UV and visible wavelengths is not favorable due to absorption of a glass substrate (UV) or high transmittance of the TCO for the visible radiation. The near-infrared (1064 nm) fundamental harmonics of solid-state laser is almost perfect for this application. Several watts of the laser power can be transmitted through the glass substrate with no damage. However, this wavelength is strongly absorbed by the TCO layer. Since this TCO layer is very thin (a few hundred nanometers), it can be completely ablated in a single pass at a low-power level [11].

P2 (and P3) scribing involves removal of much more material than in P1, including the silicon layers with the larger thickness. By conventional ablation, removal of more material requires that the laser power is increased by a corresponding amount. A novel “micro-explosive” lift-off process allows this to be accomplished at high speed, without the use of high laser power which could damage the glass or TCO (see Fig. 21).

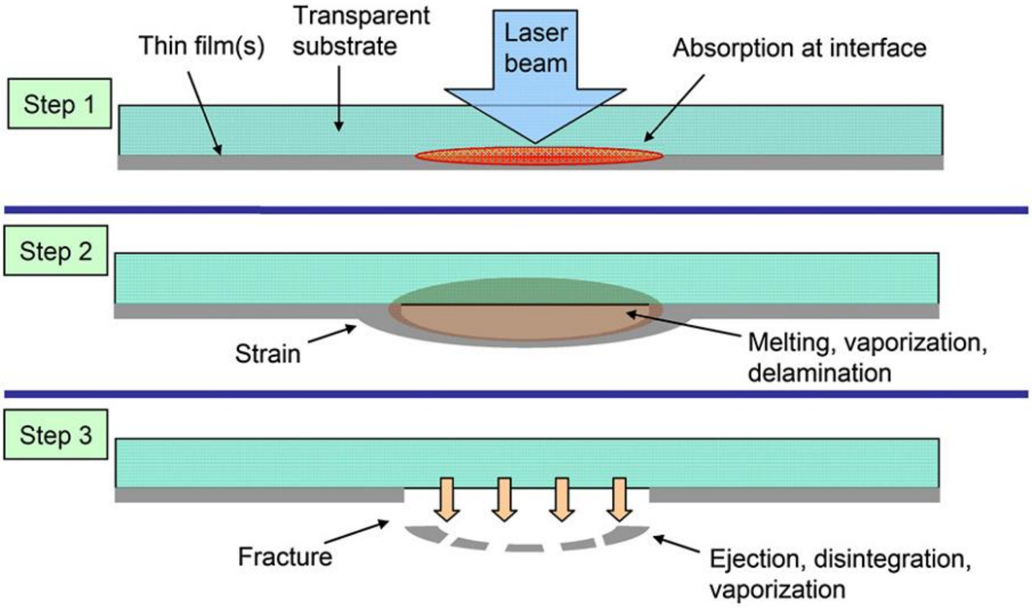

Fig. 21 Illustration of “micro-explosive” lift-off process [43].

In this case, P2 uses a frequency-doubled solid-state laser with 532 nm output. The green beam passes through the glass and the TCO. In particular, the weak absorption of TCO at 532 nm allows it to transmit the laser power of 1 W levels without sustaining any damage. Since silicon absorbs this green laser light very strongly, most of the laser pulse energy is therefore deposited at the TCO-silicon interface. This cleanly and completely blows off the overlying silicon layer at much lower power levels than is needed for either photo-thermal or photo-chemical ablation processes. P3 uses exactly the same process; the thin film of metal is carried away with the underlying silicon. Because this is a binary-threshold process, producing clean edges dictates the use of a masked beam rather than a focused beam. In practice, a circular mask is used to aperture the central portion of the Gaussian laser beam so that the intensity exceeds the process threshold across the entire apertured beam (see Fig. 22) [11].

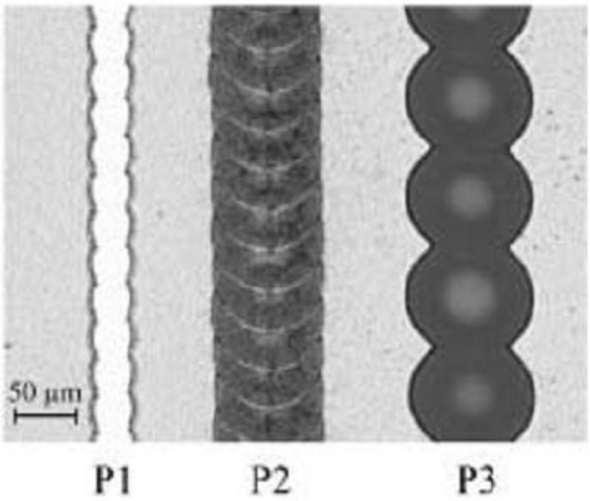

Fig. 22 Microscopic view of the interconnection region with optimized laser parameters in the a-Si thin-film solar cell structure: P1 - glass/ZnO/SnO_2 processed with 1064 nm wavelength; P2 - glass/ZnO/SnO_2/a-Si processed with 532 nm wavelength and P3 - glass/ZnO /SnO_2/ZnO/Ag processed with 532 nm wavelength [44].

2.4.2.3 Serial interconnect formation by a front-side P1, P2 and P3 scribing

Use of flexible substrate or metal back-contact eliminates possibility to scribe the thin-film solar cells through the substrate side. Only a front-side scribing could be applied by direct laser ablation process and no wavelength selective process could be used. The laser pulse length and accuracy in the ablation depth play important roles as material has to be removed with no damage to the underneath layers. Various laser sources were tested in selective ablation of thin-films [12-15]. Nanosecond laser pulses were not found to be favorable for the damage-free front-side scribing of the thin-film CIGS solar cells [12]. The main limiting factor for laser processing of the multilayer Cu(In,Ga)Se_2 structures is deposition of molybdenum on walls of the channels scribed in the films, and the phase transition of semi-conducting Cu(In,Ga)Se_2 to the metallic state close to the ablation area due to formation of the thermally-induced highly conductive Cu_xSe segregations [12,45,46]. The local increase of copper concentration in overheated areas is responsible for Cu_xSe phase formation.

The shunt resistance of laser-affected areas is proportional to the resistivity of the corresponding CIGS absorber material and exponentially decreases when the amount of Cu in the film is increased [46]. In order to avoid thermal shunting of laser-affected regions, the use of shorter pulse lengths is required.

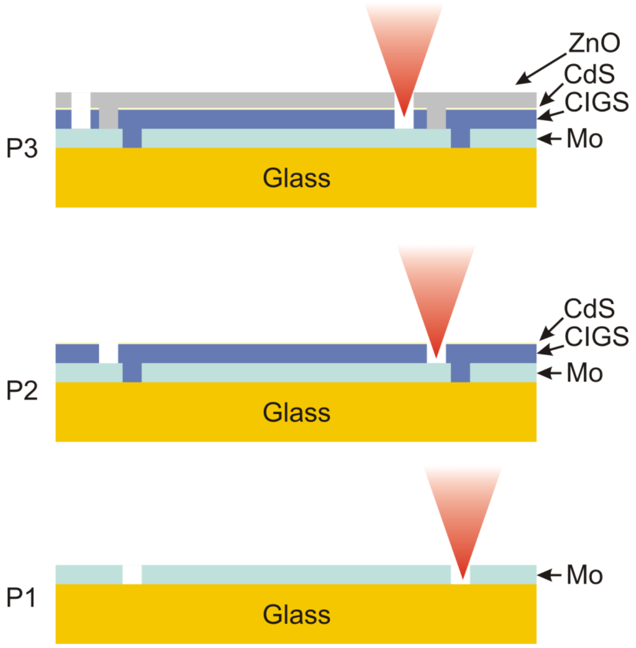

Fig. 23 Series interconnect formation in the thin-films CIGS solar cells on the glass substrate. P1: back-contact formation, P2: back-contact exposure to strip CIGS layer, P3: top-contact formation.

According to the results of theoretical modeling, processing without damage is possible with ultra-short-pulse lasers [14,16], although no industrial process has been developed yet and P2 and P3 steps are processed mechanically.

In case of the CIGS solar cells, molybdenum is nearly always used for the back-contact layer [47], and independently of the substrate type (glass or flexible polymer) the interconnects should be formed only by the front-side scribing process.

In a typical CIGS process, a laser is used to segment the first conductive layer (P1), typically molybdenum (Mo), into adjacent electrically-isolated strips (or bands). Next, the CIGS absorber, CdS, and intrinsic ZnO (iZO) layers are deposited and in the P2 step scribed down to the first conductive layer (Mo) with a slight offset from the underlying P1 scribe. Finally, another transparent conductive layer is added and scribed again (P3) with an offset from the previous P2 scribe. The area between the P1 and the P3 scribe becomes electrically inactive for the purpose of generating electricity, and minimizing of this so called "dead zone" is a primary motivation to consider a laser tool over a mechanical scribe tool. It should be noted that, while it is only necessary to scribe the top conductive layer to make the P3 scribe. In practice the P3 scribe is made down to the bottom conductor layer (Mo) making it nearly identical to the P2 scribe [40].

2.4.2.4 Serial interconnect formation by front-side P2 micro welding

When CIGS thin-film solar cells are manufactured on the flexible substrate, the use of mechanical P2 and P3 scribing is difficult or impossible due to the nature of the substrate material [48]. Film stability and surface flatness play an important role.

In contrast to the extremely smooth and hard surface of glass substrates, solar cells on the polyimide films or metal foils are difficult to structure by a mechanical tool without damaging the soft polymer surface or the sensitive dielectric insulation layer [10].

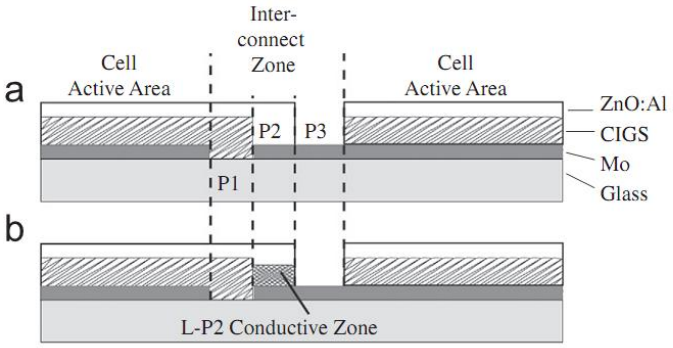

Fig. 24 (a) Module interconnect structure showing the isolating P1 scribe, the interconnect P2 scribe and the isolating P3 scribe. (b) Laser-formed P2 replaces the direct ZnO–Mo contact [48].

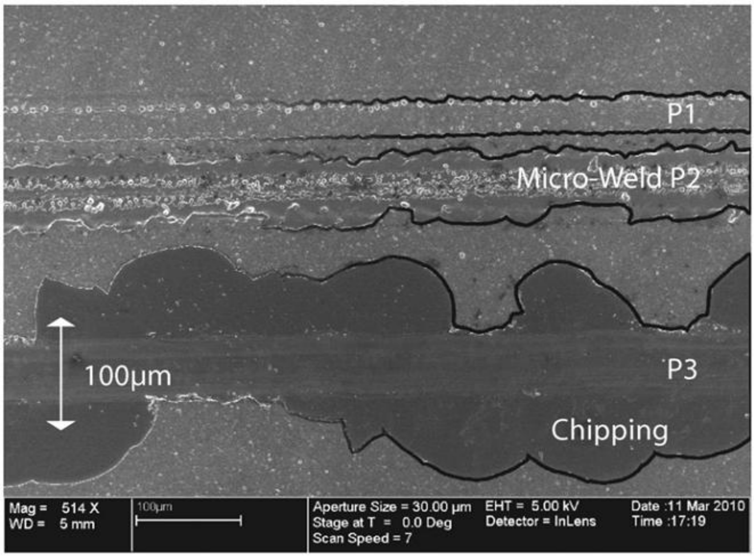

Fig. 25 SEM image showing the experimental P2 scribe between the P1 scribe and a mechanically patterned P3 isolation scribe. The necessity for extensive safety margins for mechanical patterning is illustrated by considerable chipping of the CIGS/ZNO layers along the P3 scribe edges. Contrasting lines have been added on the right for clarity [49].

As an alternative method for the P2 step direct laser scribing process could be the P2 micro weld formation technique (see Fig. 24). Instead of removing the CIGS entirely, analogous to mechanical patterning, some research groups used a laser to transform CIGS locally to create a conductive zone that replaces the direct contact between ZnO:Al and Mo [48,49]. Although the process is used where mechanical patterning is not an alternative, direct benefit such as reduced interconnect resistivity have been reported [50].

2.4.2.5 Serial interconnect formation by front side P3 and P4 scribing

Serial interconnects can also be formed by using P3 and P4 step laser scribing together with ink-jet printing of isolating and conductive adhesives. In this case laser processes are applied after deposition of all the thin-film layers. In CIGS solar cells at P3 step, the laser has to expose the Mo back-contact by removing all the upper material. For P4 process, all the solar cell layers have to be removed leaving the underneath substrate undamaged. Two P3 scribes and one P4 scribe are required for interconnection. The first P3 and last P4 patterns are filled with an isolating adhesive to isolate separate cells. Then the middle P3 scribe is filled with a conductive adhesive in order to connect back and front contacts of separate cells.

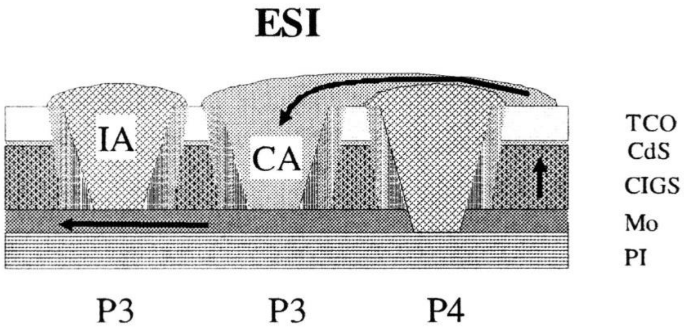

Fig. 26 Interconnection area of the CIGS solar cell. The electrical connection and insulation are realized by means of conductive and isolating adhesive, which are applied after the patterning steps P3 and P4 [51].

2.4.2.6 Pulse duration effects

When long nanosecond laser pulses are used, the ablation mechanism is associated with thermal heating, melting and evaporation of the material. Heat diffusion plays an important role as larger melted area is formed. The material can be removed not only in vapor form, but also as melted clusters. As less energy is used for evaporation, the material can be removed more efficiently. In case of ultra-short laser pulses, the ablation mechanism can be still thermal, although the heat diffusion is much lower, and the ablation is associated only by evaporation of the material. This gives a smaller heat effected zone and higher ablation quality.

For the back-side scribing processes, the material lift-off process dominates making possible thermal damage-free ablation of thin film layers. However, some defected areas can still be formed leading to the shunt formation and decrease in the solar cell efficiency. The pulse duration is critical in case of the front-side P3 scribing of CIGS solar cells. Nanosecond-laser machining causes damage of the PV devices. Shunts can be produced between the top-contact and Mo layer that transforms the solar cell in to an ohmic resistance [12,16].

The reason for this is the projection of the molybdenum onto the side walls of the scribe and modification of the CIGS layer to the conductive state. For this reason, the front-side P3 step scribing of CIGS can be performed only with ultra-short laser pulses [14,52].

2.4.2.7 Border deletion (P4)

Border deletion is a common process in manufacturing of the thin-film solar cells. Usually, depositions of the absorber layer, back and front contacts are separate processes and the deposited area for each layer could vary depending on the process.

In case of CIGS solar cells, some non-uniformity of the absorber layer thickness and layer composition can also be detected at the edges of the deposition area. Combination of all these irregularities led to the defected area formation with a low efficiency or even to the shunt formation which reduces the overall efficiency of the solar cell device. For this reason, the defected edges should be removed or isolated from the rest of uniform layer stack by removing all the material from the substrate (see Fig. 18). The edge deletion is also used to prepare the module for electrical interconnect and encapsulation.

There are several processes developed for the edge deletion including wet chemical etching, sand blasting, plasma etching and laser scribing. Lasers offer flexible, damage-free non-contact method for the thin film removal and it is being integrated in mass production lines.

2.4.2.8 Laser crystallization for thin-film solar cells

Polycrystalline silicon thin layers fabricated at low temperature on cheap substrates such as glass are of great interest for large area electronic devices such as thin-film transistors or thin-film solar cells. Polycrystalline silicon thin-film solar cells represent a low-cost alternative to wafer-based solar cells while still having the potential for high efficiency. In order to benefit from the cost advantage of Si thin-film solar cells, low-cost substrate materials such a glass are required. One limitation of glass substrates is that these substrates cannot be heated above 650°C (already a high temperature for the boron-silicate glass) during the thin-film processing. Among several methods proposed for the preparation of polycrystalline Si layers, laser crystallization offers the advantage to produce large grains of several 100 μm size while heating the glass substrate only for a very short duration (<ms at the glass surface). These laser-crystallized layers can be used as seed layers for subsequent epitaxial growth of less defected thicker Si layers (1.5–2 μm) for sufficient light absorption in the indirect semiconductor silicon [53,54].

2.4.2.9 Pulsed laser deposition of thin layers for thin-film solar cells

Pulsed laser deposition (PLD) is a thin-film deposition technique where a high-power pulsed laser beam is focused inside a vacuum chamber to strike a target of the material that is to be deposited. This material is vaporized from the target and is deposited as a thin film on a substrate. This process can occur in the ultra high vacuum or in the presence of a background gas, such as oxygen which is commonly used when depositing oxides to fully oxygenate the deposited films.

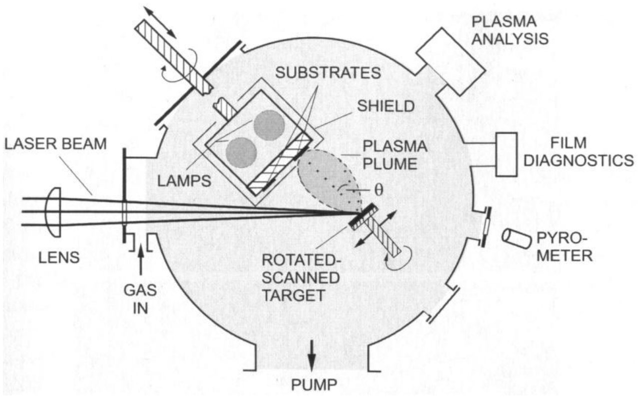

Fig. 27 Schematic of a PLD setup [55].

High quality of the absorbing thin-film layer has been regarded as one of the key success factors for high-efficiency solar cells. Electrical properties such as carrier concentration and mobility are also important for realization of high-efficiency devices. Hence, investigation and enhancement of these properties have drawn significant interest in recent years [56]. The CIGS thin-films with higher carrier concentration may be achievable through a suitable choice of process parameters of the corresponding deposition technique. Several deposition and post-treatment techniques, such as thermal co-evaporation, sputtering, electro-deposition, and selenization of metallic precursors, have been studied to satisfy the requirements of the absorbing layer [56-58]. As one of the alternative techniques, the pulsed laser deposition (PLD) has been recognized as an effective method in preparing homogeneous multi-component films primarily because it proceeds congruently [59,60]. However the process scalability is very complex and this technique can be applied only for the small-area high-efficiency solar cells and is not suitable for mass production.

2.4.2.10 Isolation of shunted regions

Efficiency loss due to regions with low shunt resistance is one of the major challenges currently facing PV manufacturers. Shunted cells significantly reduce average efficiencies, resulting in modules with poor PV performance and reduce the total yield. Although defected areas are highly localized, the lateral conductive path formed by the emitter and by metal contacts generally causes much larger areas of the solar cell to be affected [61]. Usually this technique is used for Si wafer based solar cells, but it could also be applied for thin films. Today there are several tools (lock-in thermography, laser beam induced current detection, electroluminescence or photoluminescence measurements) used to detect shunted regions on the solar cell surface. The already developed P3 step laser scribing technique could be applied to isolate the shunt areas.

2.4.3 Mechanical scribing of thin-film solar cells

In mechanical patterning of thin-film layers needles are used for the layer removal. This is a direct contact method which induces mechanical stress and damage to the material. The substrate roughness plays important role when mechanical scribing is applied as this method is sensitive to the height variations of the scribed surface. Therefore this method could only be applied if thin films are deposited on a hard and smooth substrate [10] and is not suitable for thin films on soft flexible substrates. Other disadvantages are the wide scribe width which leads to the larger dead area formation of the formed interconnect, edge microcracking leading to losses in the module efficiency and constant tool wear. Tool wear gets important when going to mass production where modules have to be manufactured 24 hours per day, 7 days per week and constant replacement and recalibration of needles become time consuming and not efficient.

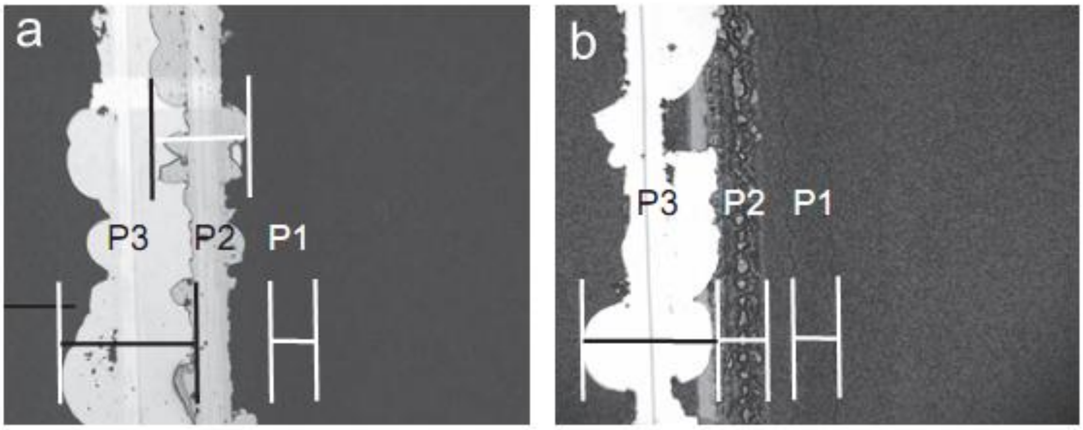

Fig. 28 Optical microscope images showing the interconnect zone to compare standard mechanical patterning (a) with the laser P2 (b). The laser made P2 scribe is approximately 60 μm wide while the mechanical P2 is almost three times wider [48].

2.4.4 Photolithographic method of interconnect formation in thin-film solar cells

Photolithography is a process used in microfabrication to selectively remove parts of a thin film or the bulk of a substrate. It uses light to transfer a geometric pattern from a photo mask to a light-sensitive chemical photoresist on the substrate. A series of chemical treatments then engrave the exposed pattern into the material underneath the photo-resist.

Photolithographic methods in principle allow chemical and selective patterning of all layers. The UV-lamp in combination with photomask could be applied to form required patterns in thin-film solar cells. This approach works for P1 and on small areas but is unsuitable for large areas (>30 x 30 cm^2). The exact adjustment of the photomasks for P2 and P3 (with regard to P1), however, is both time-consuming and unsatisfying. Another approach is to use the UV-laser source. The focused blue laser beam could be used for scribing (illumination) of the photo-resist only, but not for the direct film removal [10], then chemical treatment could be used to form a required pattern. Applying these methods gives fine scribe quality, although the application of photolithography in mass production of solar cells is very complex and time-consuming.

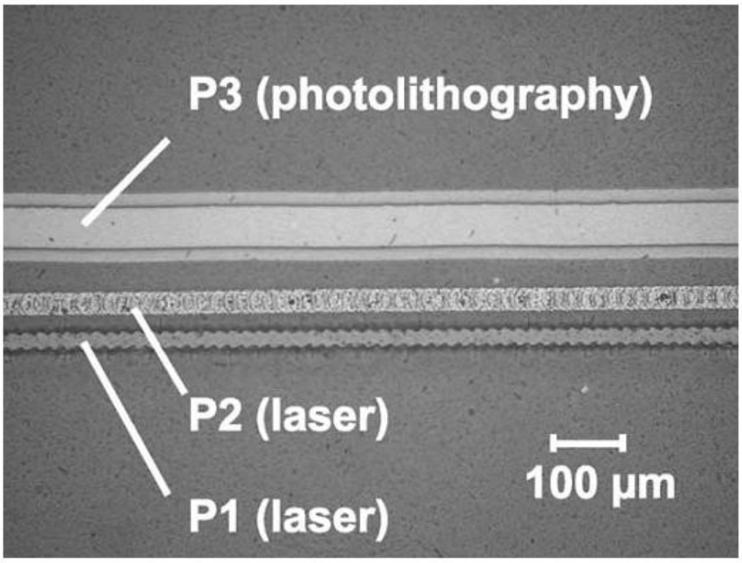

Fig. 29 Patterning scribes P1, P2 and P3 on a polyimide substrate [10].

2.5 Laser scribing experiments in literature

The first US patent for laser scribing for solar module integration was granted to J.J. Hanak in 1981. Since then, a number of refinements of this method have been patented, mostly emphasizing a-Si:H and SnO_2, with at least one of these emphasizing the use of excimer lasers [12].

Thirst attempts of Nd:YAG nanosecond laser scribing of thin-film CIGS solar cells were made by A.D. Compaan et al. [12]. In this paper the author investigates the ablation properties of CdTe, CIGS, ZnO, SnO_2, Mo, Al and Au thin-films with nanosecond lasers, although no electrical characterization of solar cells after laser scribing was performed. Later J. Hermann investigated nanosecond and femtosecond laser scribing processes of CIS thin-film PV devices [14,16]. In those papers authors have concluded that processing with nanosecond lasers leads to degradation of the solar cell electrical properties. The picture below shows *J(V)* characteristics of solar cells after laser processing.

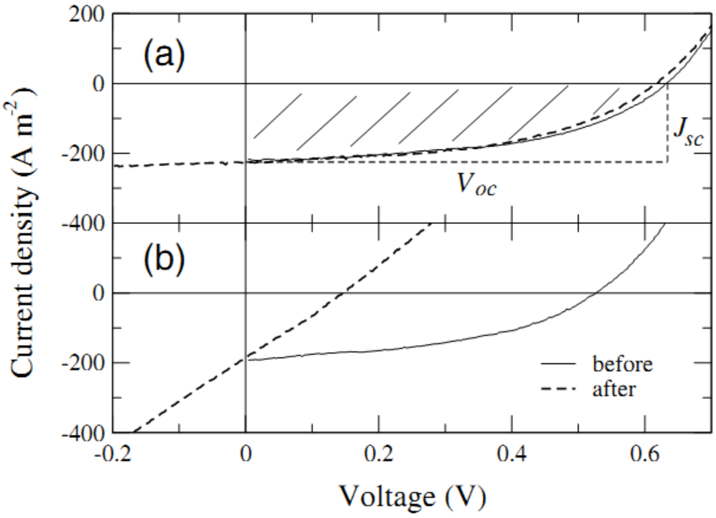

Fig. 30 Solar cells current density as a function of the applied voltage measured before and after machining with femtosecond Ti:Sapphire (a) and ArF UV nanosecond laser pulses (b) [14,16].

Measurements of the photo-electrical properties of the solar cells demonstrate that nanosecond laser-machining causes damage. In that case, a shunt is produced between the ZnO and Mo layers and it transform the solar cell in to an ohmic resistance. SEM and EDX analyses identified two major causes of the degradation: (i) residues of Mo were projected onto the walls of the ablation channel (see Fig. 31), and (ii) the metallization of the CIS semiconductor occurred close to the channel border [14,16].

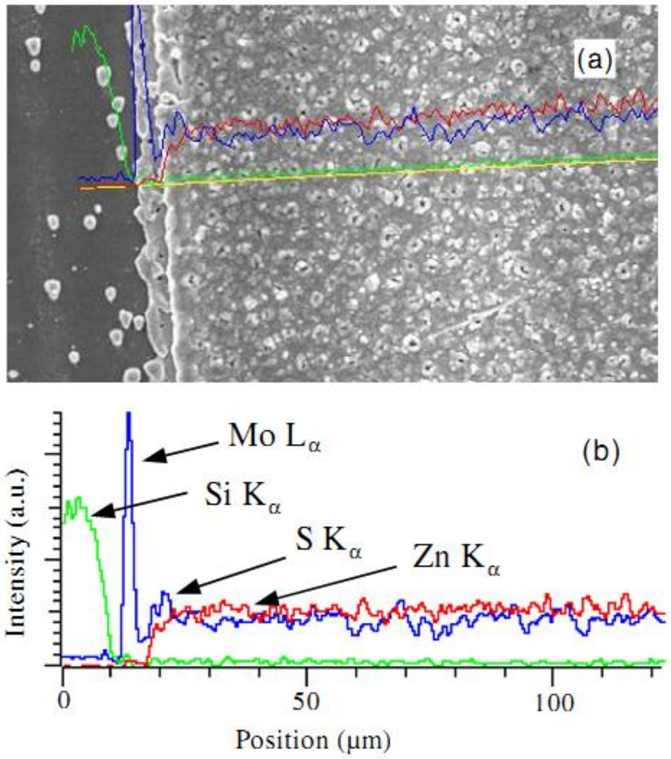

Fig. 31 (a) SEM image showing an ablation channel of a solar cell obtained with Nd :YAG nanosecond laser pulses of 2.1 J/cm^2 fluence and a scanning velocity of 15 μm/s .(b) EDS analysis showing the intensities of Zn K_α, Si K_α, S K_α and Mo L_α lines as a function of the position orthogonal to the ablation channel [14,16].

Other investigations of standard P1, P2, P3 laser scribing of solar cells with picosecond and femtosecond lasers were performed by a number of authors [40,51,62-67]. Some of the results are shown below.

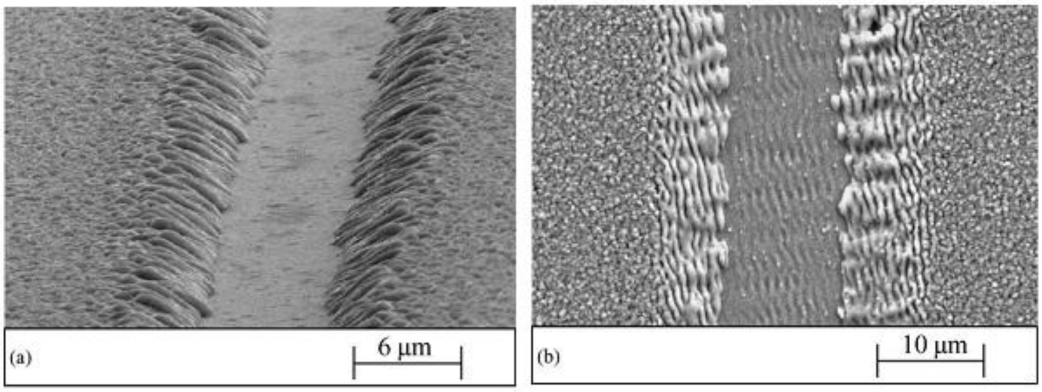

Fig. 32 SEM micrographs of $CuInSe_2$–Mo/Ti-layers on polyimide after selective P3 structuring. On the bottom of the grooves the molybdenum back-contact is visible: (a) femtosecond laser (F = 0.63 J/cm^2, v = 0.4 mm/s) and (b) picosecond laser (F = 0.72 J/cm^2,v = 20 mm/s) [64].

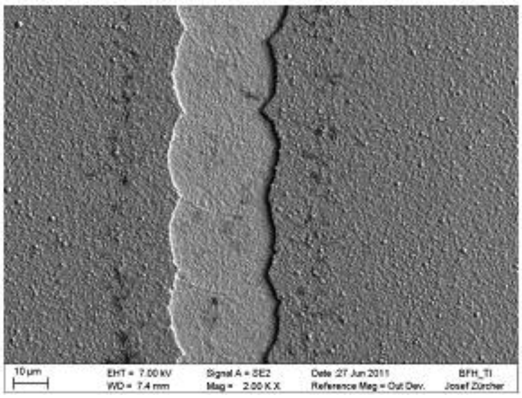

Fig. 33 Electron micrograph of a P3 scribe made at 532 nm with the 30 ps pulse length [66].

In all cases the authors concluded the ability of the ultrashort pulsed lasers for damage-free processing thin-film CIGS solar cells. Several groups [40,66,67] were able to produce mini PV modules with laser scribed series interconnects and compare them with mechanical scribed modules. The laser scribed mini-modules showed similar efficiencies compared with those manufactured mechanically (see Fig. 34). Other groups were investigating alternative interconnection design and scribing methods. P2 micro-weld formation was investigated by a group from Sweden [48,49]. More details can be found in section 2.4.2.4. The use of an alternative method for laser and mechanical patterning was investigated by group from Germany and Switzerland [10,68]. More details can be found in section 2.4.4.

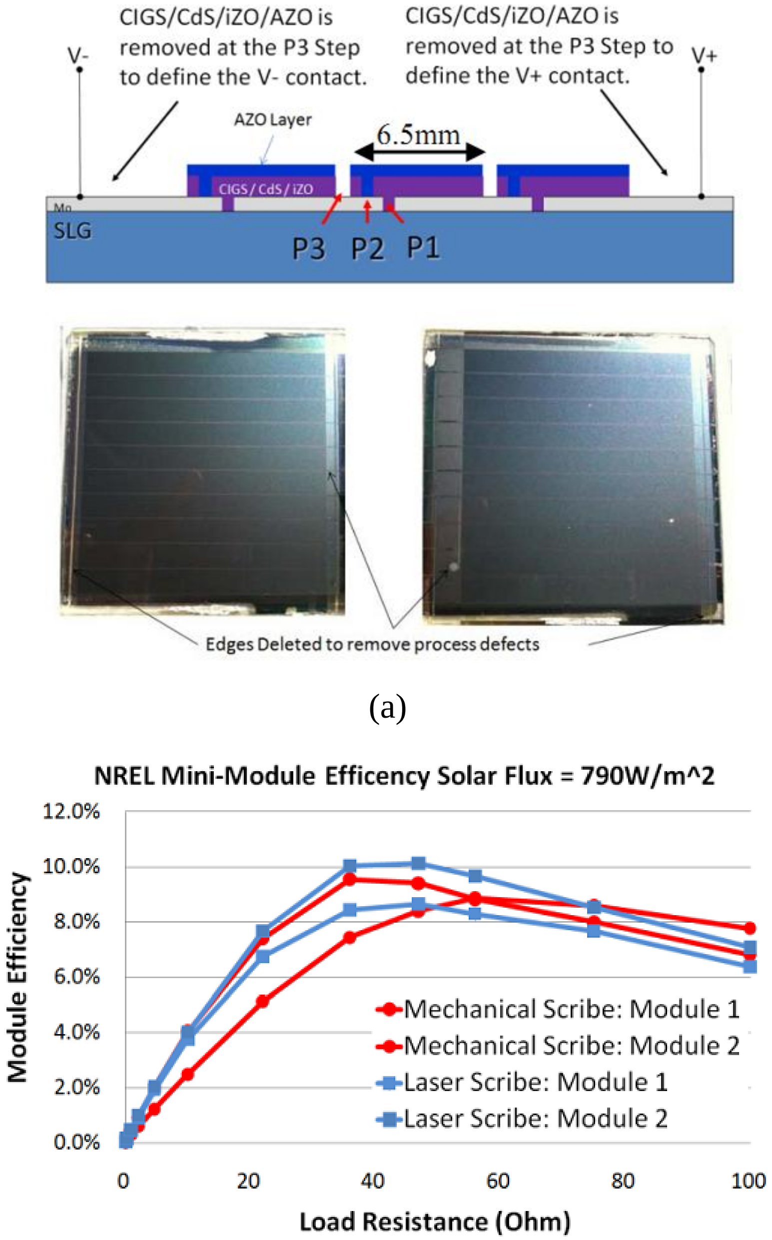

(a)

(b)

Fig. 34 (a) Electrical / Mechanical structure of mini-module cell interconnects. Appearance of actual mini-modules after the laser processing, including edge deletion and defect deletion. (b) Laser scribed and mechanically scribed mini-module efficiency as a function of load resistance [40].

3 THEORY OF LIGHT INTERACTION WITH MULTILAYER THIN-FILM STRUCTURE

3.1 Absorption of laser radiation

The reflection at the surfaces is described by the coefficient of reflection or reflectivity. This is usually given by the symbol R_λ and is defined as the ratio of the reflected power to the power incident on the surface. The coefficient of transmission or transmittance T_λ is defined likewise as the ratio of the transmitted power to the incident power. If there is no scattering, then by conservation of energy [69]:

$$A_\lambda + R_\lambda + T_\lambda = 1, \tag{10}$$

where A_λ is the absorptivity. The absorption and refraction of a medium can be described by a single quantity called the complex refractive index. This is usually given by the symbol $\bar{n}$ and is defined through the equation:

$$\bar{n} = n + ik_{ext}, \tag{11}$$

The real part of the complex refractive index, namely n, is the same as the normal refractive index. The imaginary part of $\bar{n}$, namely k_{ext}, is called the extinction coefficient. The reflectivity depends on both n and k_{ext} and is given by [70]:

$$R_\lambda = \left|\frac{\bar{n}-1}{\bar{n}+1}\right|^2 = \frac{(n-1)^2 + k_{\text{ext}}^2}{(n+1)^2 + k_{\text{ext}}^2}. \tag{12}$$

It gives the coefficient of reflection between the medium and the air (or vacuum) at a normal incidence. The absorption of light by an optical medium is quantified by its absorption coefficient α. This is defined as the fraction of the power absorbed in a unit length of the medium. Extinction coefficient k_{ext} is directly related to the absorption coefficient of the medium [70]:

$$\alpha = \frac{4\pi k_{\text{ext}}}{\lambda}, \tag{13}$$

where λ is the wavelength of light in vacuum. According to the Beer–Lambert–Bouguer law the intensity of the electromagnetic wave inside the material decays exponentially. If the beam is propagating in z direction, and the intensity (optical power per unit area) at position z is I, then the decay of the intensity inside the material can be expressed as [70]:

$$I = \left(1 - R_{\lambda}\right) I_0 e^{-\alpha z}, \tag{14}$$

where I_0 is the intensity of the incident beam. The transmittance of an absorbing medium at a distance z is given by:

$$T_{\lambda} = \left(1 - R_{\lambda}\right) e^{-\alpha z}, \tag{15}$$

and the absorptivity from Eqs. (10) and (15) is:

$$A_{\lambda} = \left(1 - R_{\lambda}\right)\left(1 - e^{-\alpha z}\right), \tag{16}$$

The penetration depth [71,72]:

$$\delta_{\mathrm{p}} = \frac{1}{\alpha}, \tag{17}$$

is the parameter that describes the decay of electromagnetic waves inside the material. It refers to the depth at which the intensity or power of the field decays to e^{-1} (about 37%). The skin depth, $\delta_{\mathrm{e}} = 2\delta_{\mathrm{p}}$, twice as large as penetration depth refers to the length from the surface at which the magnitude of the electric (or magnetic) field has decayed to e^{-1} of its surface value [73]. The skin depth is also known as a length at which the power of the wave has decreased to e^{-2} or about 13% of its surface value.

3.2 Heat transfer equation

The laser power absorbed by the material finally is converted to heat. The time-dependent temperature distribution at the target depth $T(t, z)$ is governed by the heat flow equation in one-dimensional form, appropriate to many experimental situations [43,74,75]:

$$\frac{\partial T}{\partial t} = \alpha_{\mathrm{diff}} \frac{\partial^2 T}{\partial z^2} + \left(1 - R_{\lambda}\right) \frac{\alpha}{\rho C_p} I e^{-\alpha z}, \tag{18}$$

where ρ is the density, C_p is the specific heat, T is the temperature, t is the time, z is the longitudinal coordinate, R_λ is the reflectivity, α is the absorption coefficient, I is the laser intensity, α_diff is the thermal diffusivity:

$$\alpha_\mathrm{diff} = \frac{\kappa}{\rho C_\mathrm{p}}, \tag{19}$$

where κ is the thermal conductivity. Heat diffuses away from an irradiated region of the material to a characteristic length described as [76,77]:

$$D_\mathrm{haz} = \sqrt{\alpha_\mathrm{diff}\tau_\mathrm{p}}, \tag{20}$$

where τ_p is the laser pulse duration.

3.3 Two-temperature model

The two-temperature model (TTM) [78-82] is needed when the laser pulse duration is less than the phonon-electron interaction time which for metals is of the order of 1 ps [83,84]. When a fs-laser pulse incidents onto the surface of a metal sample, it is generally believed that a certain amount of pulse energy will initially deposit into the sample over the skin depth across the entire beam spot. During the fs-laser pulse and metal interactions, the absorbed energy is coupled to electrons and leads to an elevated electron temperature. Subsequently, hot electrons are losing energy through two competing processes, coupling to the cold lattice and diffuse to a lower-temperature region. This electron lattice process can be described by TTM. For the electrons heat transfer equation:

$$C_\mathrm{e}\frac{\partial T_\mathrm{e}}{\partial t} = \frac{\partial}{\partial z}K_\mathrm{e}\frac{\partial T_\mathrm{e}}{\partial z} - g\left(T_\mathrm{e} - T_\mathrm{l}\right) + q. \tag{21}$$

where $C_\mathrm{e} = A_\mathrm{e}T_\mathrm{e}$ is the electron heat capacity, T_e is the electron temperature, $K_\mathrm{e} = K_\mathrm{e,0}T_\mathrm{e}/T_\mathrm{l}$ is the electron thermal conductivity, g is the coupling coefficient between electrons and lattice, q is the absorbed power per unit volume from external source [85]. For lattice heat transfer equation:

$$\left(C_\mathrm{l} + L_\mathrm{m}\delta\left(T_\mathrm{l} - T_\mathrm{m}\right) + L_\mathrm{v}\delta\left(T_\mathrm{l} - T_\mathrm{v}\right)\right)\frac{\partial T_\mathrm{l}}{\partial t} = g\left(T_\mathrm{e} - T_\mathrm{l}\right), \tag{22}$$

C_l is the lattice specific heat, L_m and L_v are latent heat of melting and vaporization of the lattice, δ is the Dirac delta function, T_l is the lattice temperature.

3.4 Matrix method

For a metallic medium the dielectric function and the index of refraction are complex valued functions. This is also the case for semiconductors and insulators in certain frequency ranges near and at absorption bands. The complex refractive index:

$$\bar{n}_{m,k} = n_{m,k} + ik_{\mathrm{ext}\ m,k} \tag{23}$$

where *k* is the layer number and *m* is the material number (see Fig. 35).

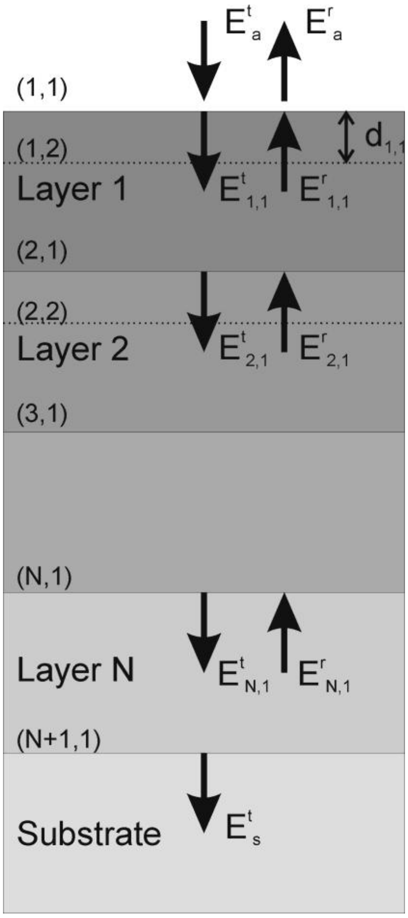

Fig. 35 Discretization of the optical model.

Fresnel's equations are still valid but the angles in the equations are now complex valued and do not have the obvious geometrical interpretation. The reflectivity at normal incidence for interface between different medium can be found from Eq. (12) [70]:

$$R_{\lambda} = \left| \frac{\bar{n}_{m,k-1} - \bar{n}_{m,k}}{\bar{n}_{m,k-1} + \bar{n}_{m,k}} \right|^2 = \frac{\left(n_{m,k-1} - n_{m,k}\right)^2 - \left(k_{\text{ext}\,m,k-1} - k_{\text{ext}\,m,k}\right)^2}{\left(n_{m,k-1} + n_{m,k}\right)^2 + \left(k_{\text{ext}\,m,k-1} - k_{\text{ext}\,m,k}\right)^2}, \tag{24}$$

The investigated work-piece is made up of a multilayer thin film deposited on the polymer substrate. The thickness of the layers is comparable to the wavelength of laser radiation, and the thickness of the substrate exceeds the wavelength of the laser radiation by several orders. The surface is considered as being thermally semi-infinite. The investigated solid is irradiated with a pulsed laser source with a single rectangular pulse. For the elapsed times investigated herein, the thermal penetration depth inside the solid is very small as compared to the spot diameter. Thus the thermal field in the vicinity of the center of the spot can be very well approximated as one-dimensional. The optical and thermal properties of the investigated materials are considered to be temperature independent. For the investigated time intervals the radiative and convective heat losses from the thin film surface toward the ambient as well as non-equilibrium and non-Fourier thermal effects can be neglected. The energy flow along z direction:

$$S = \frac{n}{2\mu c'} E_{\mathrm{a}}^{\mathrm{t}2}, \tag{25}$$

where n is the real part of the air refractive index, μ is the air magnetic permeability, c' is the speed of light and $E_{\mathrm{a}}^{\mathrm{t}}$ is the amplitude of linearly polarized electric field. The relation between the transmitted and refracted electric field, $E_{m,k}^{\mathrm{t}}$ and $E_{m,k}^{\mathrm{r}}$, at the k-th interface is:

$$\begin{pmatrix} E_{m,k-1}^{\mathrm{t}} \\ E_{m,k-1}^{\mathrm{r}} \end{pmatrix} = \mathbf{M}_{m,k} \begin{pmatrix} E_{m,k}^{\mathrm{t}} \\ E_{m,k}^{\mathrm{r}} \end{pmatrix}, \tag{26}$$

where $\mathbf{M}_{m,k}$ is the transmission matrix of the k-th layer of the m-th material defined as

$$\mathbf{M}_{m,k}=\frac{1}{\bar{t}_{m,k-1}}\times\begin{bmatrix}\exp\left(i\delta_{m,k}\right) & \bar{r}_{m,k-1}\exp\left(-i\delta_{m,k}\right)\\ \bar{r}_{m,k-1}\exp\left(i\delta_{m,k}\right) & \exp\left(-i\delta_{m,k}\right)\end{bmatrix}, \tag{27}$$

where:

$$\delta_{m,k}=\frac{2\pi}{\lambda}\bar{n}_{m,k}d_{m,k}. \tag{28}$$

In the previous expressions the $\bar{t}_{m,k-1}$ and $\bar{r}_{m,k-1}$ are the Fresnel‘s coefficients defined as:

$$\bar{t}_{m,k-1}=\frac{2\bar{n}_{m,k-1}}{\bar{n}_{m,k-1}+\bar{n}_{m,k}}, \tag{29}$$

$$\bar{r}_{m,k-1}=\frac{\bar{n}_{m,k-1}-\bar{n}_{m,k}}{\bar{n}_{m,k-1}+\bar{n}_{m,k}}, \tag{30}$$

The multilayer transmission matrix **M** is:

$$\mathbf{M}=\prod_{m=1}^{N}\prod_{k=1}^{N_m}\mathbf{M}_{m,k}. \tag{31}$$

It is possible to evaluate $E_{\mathrm{a}}^{\mathrm{t}}$ and $E_{\mathrm{a}}^{\mathrm{r}}$ by means of relation:

$$\begin{pmatrix}E_{\mathrm{a}}^{\mathrm{t}}\\ E_{\mathrm{a}}^{\mathrm{r}}\end{pmatrix}=\mathbf{M}\begin{pmatrix}E_{m,k}^{\mathrm{t}}\\ 0\end{pmatrix}. \tag{32}$$

The determination of $E_{m,k}^{\mathrm{t}}$ and $E_{m,k}^{\mathrm{r}}$ can be obtained by inverting Eq. (26). The power density in the *k*-th layer is given by the Pointing vector:

$$S_{m,k}=\frac{1}{2\mu c'}\mathrm{Re}\left[\left(\bar{n}_{m,k}\right)^{*}\left(E_{m,k}^{\mathrm{t}}+E_{m,k}^{\mathrm{r}}\right)\left(E_{m,k}^{\mathrm{t}}-E_{m,k}^{\mathrm{r}}\right)^{*}\right]. \tag{33}$$

And the absorbed power per unit volume is:

$$q=f\left(t\right)\frac{\mathrm{d}S_{m,k}}{\mathrm{d}x}, \tag{34}$$

where the pulse function is defined as

$$f\left(t\right)=\begin{cases}t/t_{\mathrm{p}} & \text{for } 0\le t\le t_{\mathrm{p}}\\ 0 & \text{for } t\ge t_{\mathrm{p}}\end{cases}. \tag{35}$$

The nonlinear TTM thermal problem was numerically solved by the finite difference method by using Comsol Multiphysics software.

3.5 Material parameters

Table 5 Material parameters. Physical properties: C_p – specific heat, κ – thermal conductivity, ρ – density, α_λ – absorption coefficient, λ - wavelength, n - real part of the refractive index, k_{ext} - extinction coefficient or imaginary part of the refractive index, T_m -melting point, L_m - heat of fusion, T_v – the vaporization point, L_v - heat of vaporization, E - Young's modulus, ν - Poisson ratio, α_T - the thermal expansion coefficient.

	ITO	**ZnO:Al**	**Zn:O**	**CdS**	**CIGS**	**Mo**	**PI**
C_p, J/(g·K)	0.358 [86]	0.49	0.49 [87]	0.5	0.3 [16]	0.25 [88]	1.15 [89]
κ, W/(m·K)	8.7 [86]	23	23[87]	20	37 [16]	138 [88]	0.52 [89]
ρ, g/m^3	7.2E6[86]	5.6E6	5.6E6[87]	4.8E6 [90]	5.8E6 [16]	10E6 [88]	1.4E6 [89]
α_{266}, cm^{-1}	2.8E5 [91]	8E5	8E5	1E6	1E6	1E6	1E6
α_{355}, cm^{-1}	1.8E4 [91]	6E5	6E5	1E6	1E6	1E6	1E4
α_{532}, cm^{-1}	1E3 [91]	4E5	100	100	1E5	1E6	1E2
α_{1064}, cm^{-1}	5.4E3 [91]	100	10	10	100	1E6	100
n_{266}	2.35 [92]	1.50	1.50	1.50	1.50	1.50	1.9
k_{266}	0.18 [92]	1.69	1.69	2.12	2.12	2.12	3.81
n_{355}	2.21 [92]	1.50	1.5	1.5	1.5	1.5	3.06
k_{355}	5.85E-02 [92]	1.70	1.70	0.28	2.83	2.83	3.21
n_{532}	1.94 [92]	2.03	2.03	2.64	1.5	1.5	3.79
k_{532}	4.59E-02 [92]	1.69	0.00 *	0.00	0.42	4.23	3.61
n_{1064}	1.76 [92] @850nm]	1.50	1.94	2.32	1.5	1.5	2.44
k_{1064}	0.083 [92] @850nm]	0.0008	0.000085	0.000085	0.00085	8.5	4,22
n_{1572}		1.3	1.3	2.3	2.9	1.6	2.4
k_{1572}		0.000085	0.000085	0.000085	0.00085	7.7	4.2
T_m, °C	1910		1975	-	1910	2623	
L_m,	0.5		0.5	-	0.5	0.39	

MJ/kg							
T_v, °C	3000		2360	1000	3000	4912	
L_v, MJ/kg	2		3	1	2	6.25	
E, GPa	116		129	52		329	
v	0.35		0.349	0.41		0.32	
Fail strain	0.022		0.04	0.025		0.1	
α_T [1/°C]	9.25E-6		1.05E-5	4.1E-6	9E-6	4.8E-6	

Because of the lack of material parameters the electron coupling coefficient was kept the same for all the materials. Electron–phonon coupling constant $g = 2.1\times10^{16}$ $\mathrm{W\cdot m^{-3}\cdot K^{-1}}$ [85,93].

4 EXPERIMENTAL SETUPS AND PROCEDURES

4.1 Experimental scribing setup

Thin-film scribing experiments were realized by using basic experimental setups shown below. Experiment set-up (a) (see Fig. 36) for the laser processing experiments included a laser, attenuator made of Pockels cell and the polarizer, harmonics module, the beam expander, a few folding mirrors, an objective mounted on the Z stage, and the sample mounted on the XY stages. In the experimental set-up (b), the laser beam was positioned by the galvanometer scanner and focused with F-Theta lens leaving a sample fixed. The Pockels cell and polarizer were used for the laser beam power control. Laser wavelengths were changed from infrared (IR) to ultraviolet (UV) region by applying harmonics modules.

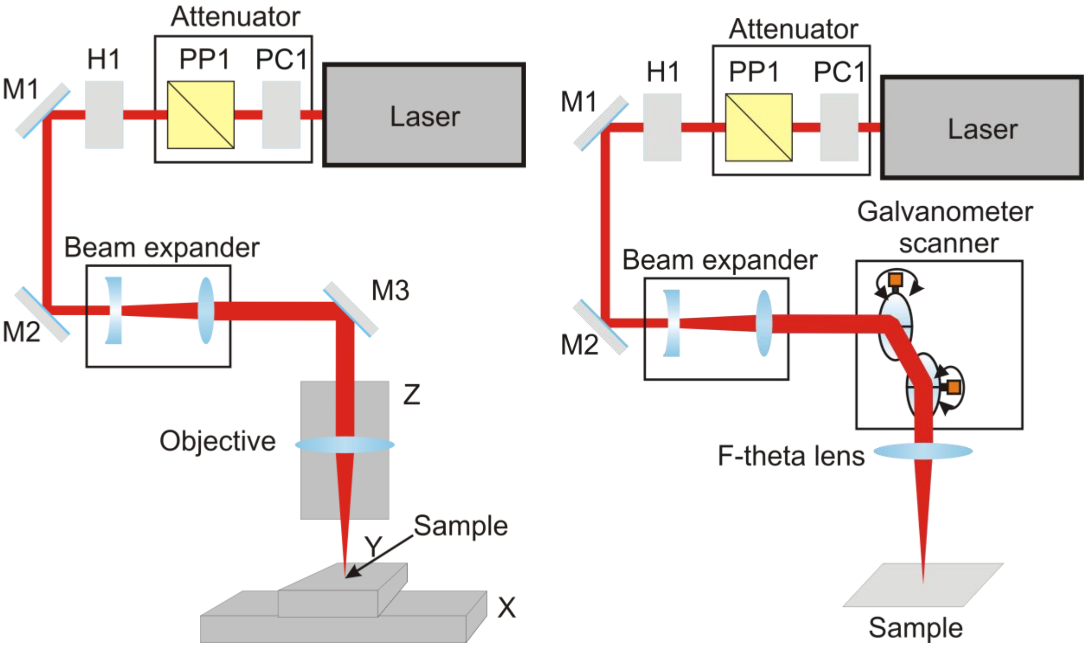

(a) (b)

Fig. 36 Scheme of experimental setups: (a) the setup with XYZ linear stages; (b) the setup with a galvanometer scanner. PP1-polarizer, PC1-Pockels cell, H1-harmonics module.

In some experiments, the setups also included the beam shaper for conversion of the Gaussian beam to the flat-top beam. The element was placed in the beam path after the beam expander close to the scanner head. Two different lasers were used in experiments: the picosecond laser PL10100 from Ekspla Ltd. and the femtosecond laser CPA 2001 from Clark-MXR. The output parameters of lasers and used wavelengths are shown in Table 6 and Table 7.

Table 6 Parameters of lasers used in the thin-film scribing experiments.

	PL10100	CPA 2001
Active media	Nd:YVO_4	Ti:Al_2O_3
Fundamental wavelength	1064 nm	775 nm
Pulse duration	10 ps	300 fs
Repetition rate	100 kHz	1 kHz
Average power	10 W	1 W

Table 7 List of laser wavelengths used in the scribing experiments.

Experimental set-up (a) XYZ stage	Experimental set-up (b) Galvanometer scanner
PL10100	PL10100
1572 nm	1064 nm
1064 nm	532 nm
355 nm	355 nm
266 nm	
CPA 2001	
755 nm	

4.2 The setup for parallel scribing

In extension of the laser scribing setup (see Fig. 36 b), a diffractive optical element was used for the laser beam splitting to realize the parallel beam scribing (see Fig. 37). The lenses L1 and L2 arranged in the 4F scheme were used to control the beam separation in a focal plane.

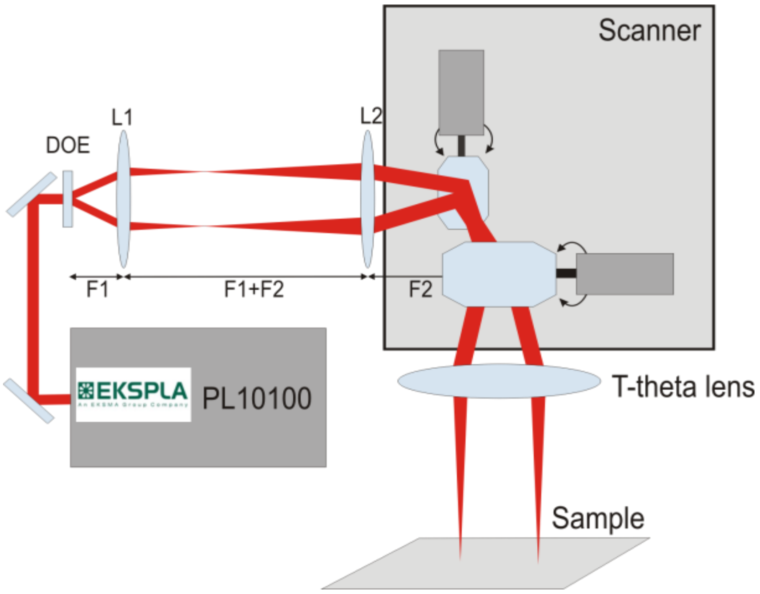

Fig. 37 Scheme of the setup for parallel beam scribing.

4.3 Flat-top beam scribing setup

The laser beam shaping is a process of redistributing the irradiance and phase. If a circular input Gaussian beam is focused by a lens, the intensity distribution in a focal plane of the lens remains circular Gaussian (Fig. 38). When a specially designed diffractive optical element for a flat-top reshaping (FBS, for instance) is introduced in front of the lens, the intensity distribution in the focal plane can be transformed in to a square-shaped beam (in lateral directions) with a flat-top intensity profile.

The diffractive optical element used in this research was the phase plate that converted the input Gaussian beam distribution into the top-hat beam after the objective lens. In the vicinity of the focal plane the beam formed the spatial distribution with a flat-top and a square cross-section (Fig. 39). The FBS beam shaper represents kind of a phase plate with a continuous and smooth phase relief profile which was fabricated by lithographic methods.

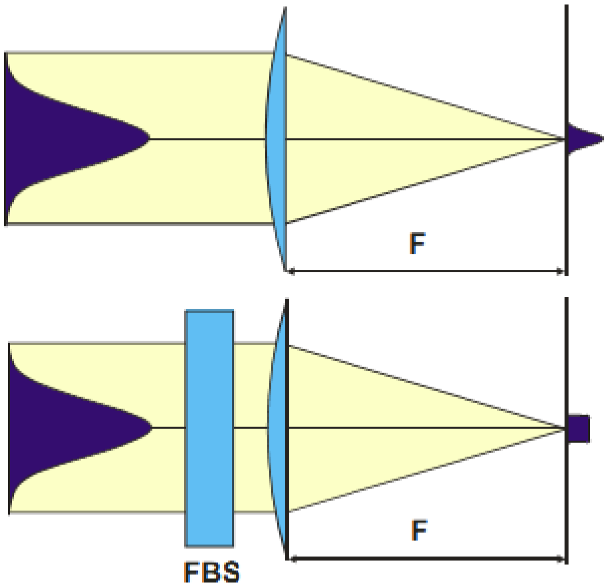

Fig. 38 Transformation of the beam profile by focusing with a lens without and with the FBS-type diffractive optical element in an optical path. Position of FBS along a beam path relative to the lens is not critical.

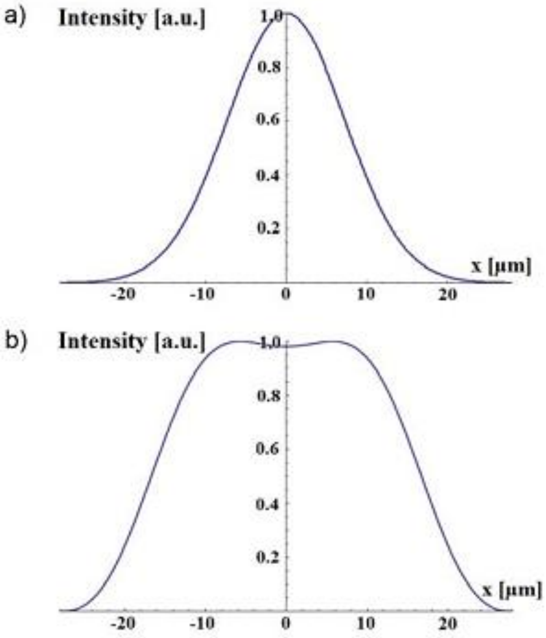

Fig. 39 Simulation of intensity distribution in a focal plane for a diffraction-limited Gaussian beam (a) and a beam transformed in to a square top-hat with the FBS shaper (b) with λ = 532 nm and NA = 0.011.

Efficiency of the beam reshaping from the circular Gaussian beam to the main top-hat profile was 95% in an area limited by $1/e^2$ (13.5%) level. The flat-area uniformity of the top-hat profile was ± 2.5%. The minimum possible (top-hat) spot size was about 1.5-2 times that of the diffraction-limited Gaussian spot. Theoretically, steepness of the edges is diffraction-limited, but practically the limitations arose from quality of the objective and the initial beam (M^2). Depth of the top-hat focus was close to that for a Gaussian beam. Size of the top-hat profile at 13% level ($1/e^2$) can be adjusted by the focal lens and follows a numerical aperture of the focusing objective according to equation [94]:

$$2w_{Top-Hat} = \frac{4k\lambda}{\pi}\frac{F}{D} \approx \frac{\lambda}{NA}, \tag{36}$$

where k is the empirical shaping parameter k~1.5; D is the diameter of the input beam on a lens; F is the focal length of the objective. Numerical aperture of the objective affected only the size but not a shape of the top-hat profile. Specifications of the FBS beam shaper of TOPAG Lasertechnik GmbH are presented in Table 8. The shaper can be customized to transform an elliptical input beam.

Table 8 Specifications of the FBS top-hat beam shaper.

Material	Fused silica
Active area diameter	2.0, 2.5…10.0 mm
Wavelength	1064 nm, 532 nm, 355 nm or 266 nm (other on request)
Transmission	99% (with AR/AR coating)
Shaping efficiency	> 95 % (in top-hat spot)
Uniformity	+/- 2.5% (of top-hat plateaus)
Minimal lateral size of top-hat spot square	5x of Gaussian spot
Installation	In optics holder with x/y adjustment

A profile of the well-prepared (spatial filtering to achieve $M^2<1.1$) laser beam with the diameter of 5.5 mm shaped with the FBS element is shown in Fig. 40. The main part of laser energy is concentrated in the main top-hat peak and only weak wavelets detached from the main peak can be recognized. A typical scribing setup with the top-hat beam is shown in Fig. 41.

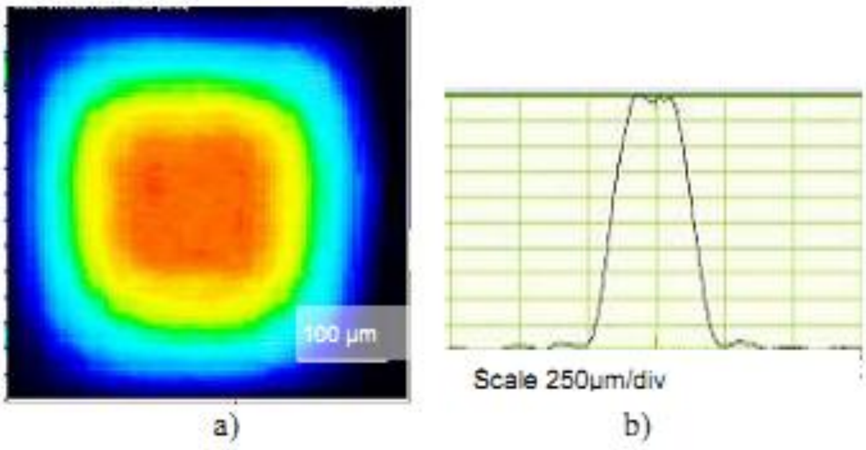

a) b)

Fig. 40 Measured profile of the FBS shaped beam (a) and its cross-section (b): the input Gaussian beam diameter ($1/e^2$) 5.5 mm, wavelength 1064 nm, focusing lens F = 1000 mm.

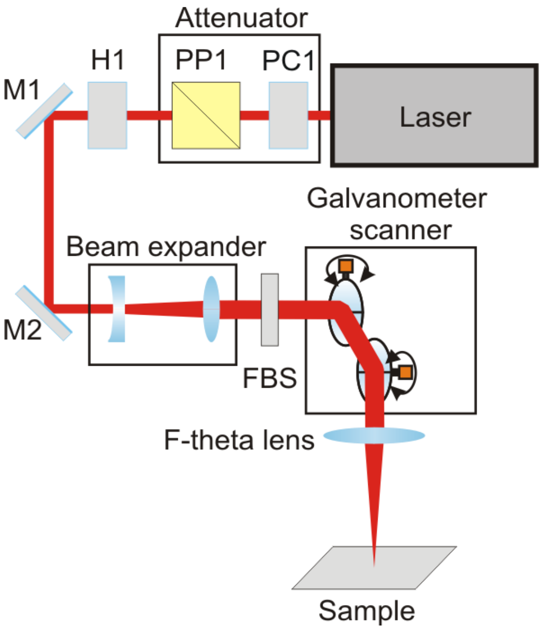

Fig. 41 Typical setup for laser ablation experiments using FBS.

4.4 Experimental procedure for estimation of the layer exposure threshold

A simple method of the material ablation threshold determination [95] was used to estimate the upper layers removal threshold to expose the underneath one. We determined this measurement as a layer exposure threshold. The method includes measuring diameters of the exposed layer area ablated with different laser pulse energies (see Fig. 42).

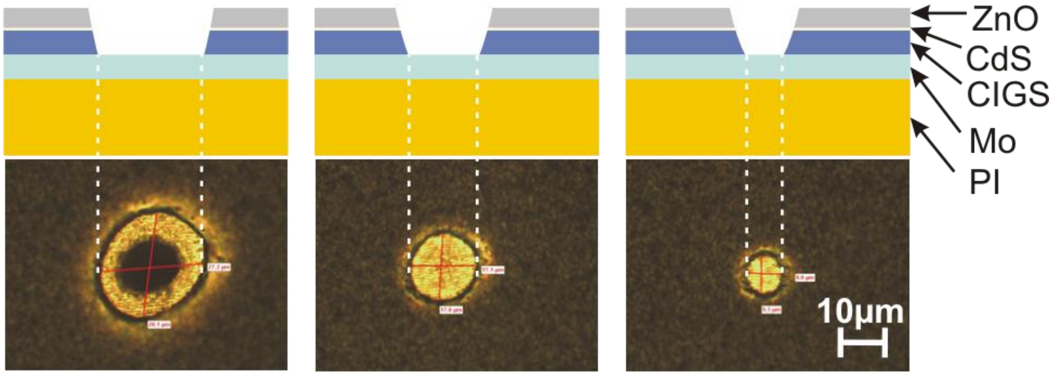

4.42 µJ@10 pulse 1.42 µJ@10 pulse 0.61 µJ@10 pulse

Fig. 42 Illustration of layer exposure threshold measurements.

The diameter of the exposed area is related to laser and material parameters as follows:

$$D^2 = 2w_0^2 \ln\left(\frac{F_0}{F_{th}}\right), \tag{37}$$

where:

$$F_0 = \frac{2E_p}{\pi w_0^2}, \tag{38}$$

w_0 is the beam radius, F_0 is the laser fluence, F_{th} is the exposure threshold, E_p is the laser pulse energy.

Radius of the focused laser beam on the surface can be estimated from the linear fit of $D^2 \sim \ln(E_p)$ function, where fitted slope is equal to $2w_0^2$. Then the exposure threshold fluence can be determined from the linear fit of $D^2 \sim \ln(F_0)$ function, where $D^2=0$.

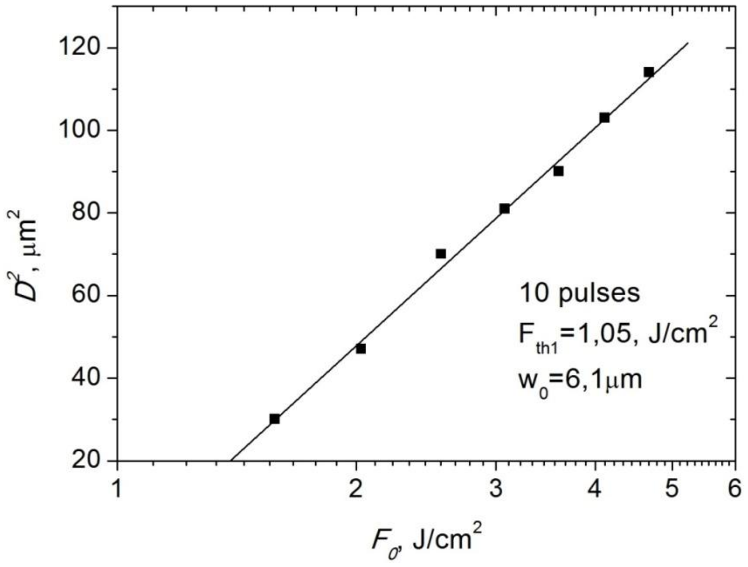

Fig. 43 The squared diameter D^2 of the exposed layer area as a function of the laser fluence applied in ZnO:Al/ZnO/CdS/CIGS/Mo/PI structure. The solid line corresponds to the linear fit of experimental data.

As many pulses are attacking the same area on the surface, accumulation of different type defects might reduce the threshold energy density required to evaporate the material in the interaction region. In this case, the ablation threshold depends on the number of laser pulses N, which are applied into the same area. The first 1000 laser pulses has effect on the ablation threshold in polymers and other materials [55]. No alteration was observed for the larger number of pulses. According to the accumulation model of Jee et al. [96], the ablation threshold and the number of laser pulses are related by an equation:

$$F_{th}(N) = F_{th}(1)N^{\xi-1}, \tag{39}$$

where $0 < \xi \leq 1$ is the accumulation coefficient, which describes incubation of defects after laser irradiation.

4.5 Electrical characterization of solar cells

4.5.1 Efficiency measurement setup

The most fundamental technique for solar cell characterization is measurement of the cell efficiency. Standardized testing allows comparison of the devices manufactured by different companies and laboratories by different technologies. The International Organization for Standardization (ISO) is responsible for standardization of the characterization of extraterrestrial solar cells. These norms correspond to the standards IEC 60904-1 to IEC 60904-10. Basic scheme of the solar cells efficiency measurements is shown in Fig. 44. More detailed information on the *I(V)* measurements can be found in section 2.3.3.2.

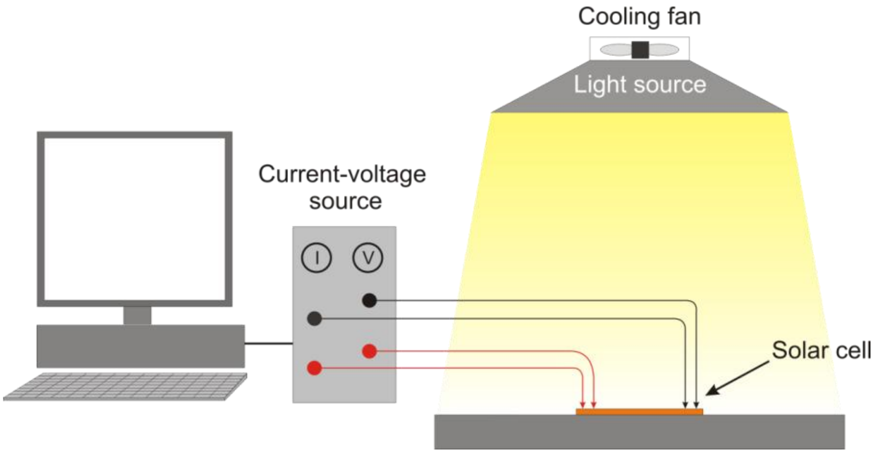

Fig. 44 Scheme of solar cell efficiency measurements.

In the study all solar cell efficiency measurements were performed at the standard testing conditions at Solarion AG. The standard conditions for cell testing were:

1. Air mass 1.5 spectrum (AM1.5) for terrestrial cells;
2. Intensity of irradiation 1000 W/m^2;
3. Cell temperature 25 °C;
4. Four-point probe measurement in order to remove the effect of probe/cell contact resistance.

4.5.2 Lock-in thermography (LIT)

Lock-in thermography has been proven as a valuable technique for non-uniformity diagnostics in crystalline and multi-crystalline solar cells [97,98]. Thermography, evaluating the local solar cell surface temperature due to the application of a forward bias in the dark, enables the detection of shunt currents via their local heating effect. However, a sensitivity limit well below 1 mK is necessary to investigate the behavior of weak shunts at the normal operating point of 0.5 V forward bias or below [98].

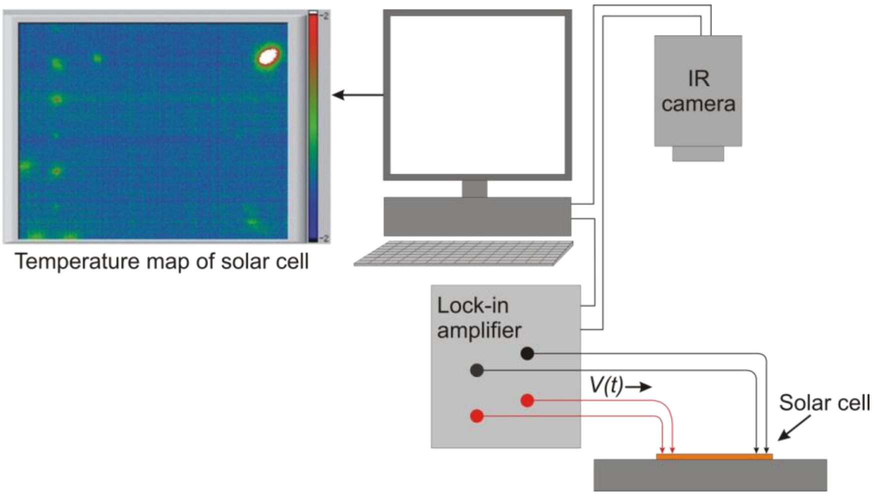

Fig. 45 Scheme of the lock-in thermography measurements.

In the lock-in thermography technique, the heat action is applied periodically, and only the local periodic temperature modulation is evaluated [99]. Due to this modulation technique only the heat-induced signals are detected, but the stationary and slowly varying image information (topography contrasts, inhomogeneous emissivity, temperature drift, etc.) is omitted. Averaging over many periods makes it possible to enhance the signal-to-noise ratio by several orders of magnitude. Finally, the spatial resolution of the lock-in thermography is governed by the frequency-dependent thermal diffusion length of the thermal waves. Thus, depending on the lock-in frequency, the spatial resolution can be drastically increased relative to the stationary thermography [98].

4.5.3 Laser-beam-induced current (LBIC) measurements

The laser-beam-induced current (LBIC) technique is a simple procedure for the superficial characterization of photosensitive devices, both those used as photovoltaic energy generators (solid state solar cells, photo-electro-chemical cells, etc) and those used to detect and measure radiation (photodiodes, photoresistors, etc). The technique uses monochromatic laser radiation with wavelength of ~650 nm to irradiate a small section of the surface of a solar cell, measuring the electric current generated. By moving the solar cell sample with a XY linear stage, the superficial mapping of the generated photo-response enabled us to obtain information about the relationship between the quantum yield and its possible structural defects [100]. The basic scheme of LBIC measurement technique is shown below (see Fig. 46).

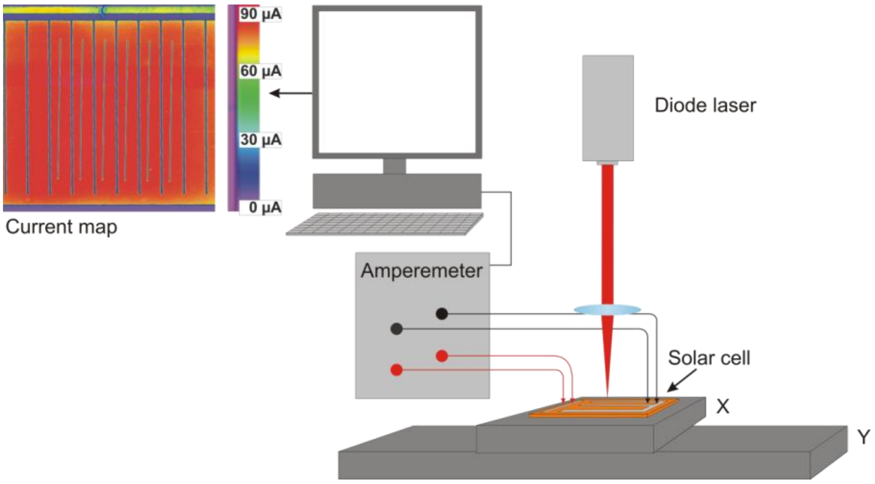

Fig. 46 Scheme of LBIC measurements set-up.

4.6 Visual and chemical analysis

Visual characterization of the solar cell samples was performed with the Olympus BX51 optical microscope. More detailed analysis of samples was performed with the scanning electron microscope JEOL JSM-6490LV equipped with the energy dispersive X-ray spectrometer EDS.

To stimulate the emission of characteristic X-rays from a specimen, a high-energy beam of charged particles such as electrons is focused into the sample being studied. At rest, an atom within the sample contains ground state (or unexcited) electrons at discrete energy levels or electron shells bound to the nucleus. The incident beam may excite an electron in an inner shell, ejecting it from the shell while creating an electron hole where the electron was. An electron from an outer, higher-energy shell then fills the hole, and the difference in energy between the higher-energy shell and the lower energy shell may be released in the form of an X-rays. The number and energy of the X-ray photons emitted from a specimen can be measured with an energy-dispersive spectrometer. As the energy of the X-rays photons is characteristic of the difference in energy between the two shells, and of the atomic structure of the element from which they were emitted, this allows the elemental composition of the specimen to be measured.

4.7 Structural characterization by Raman micro-spectroscopy

Raman spectroscopy is a spectroscopic technique used to study vibrational, rotational, and other low-frequency modes in a system [101]. It is based on inelastic scattering, or Raman scattering, of monochromatic light, usually from a laser in the visible, near infrared, or near ultraviolet range. The laser light interacts with molecular vibrations, phonons or other excitations in the system, resulting in the energy of the laser photons being shifted up or down. The shift in energy gives information about the vibrational modes in the system.

CIGS is a thermally sensitive material and laser scribing can lead to structural changes on the melted edges of the scribe causing defect formation. Raman measurements of laser affected areas were performed with 632.8 nm excitation (He-Ne laser) by using the confocal Raman spectrometer/microscope LabRam HR800 (Horiba Jobin Yvon). The excitation laser power at the sample was restricted to 1 mW and the laser beam was focused to ~ 2 µm diameter spot on the surface to obtain high spatial resolution of the investigated surface.

5 THIN-FILM SOLAR CELL SAMPLES

Three types of flexible multilayer structures of the CIGS solar cells were investigated:

(a) with a thick top-contact made of ITO (1 µm);

(b) with a thick top-contact made of ZnO:Al (350 nm);

(c) without a top-contact.

The absorber layer of $CuIn_xGa_{(1-x)}Se_2$ was 2 µm thick in all cases. A thin buffer layer of ZnO and CdS was between the top-contact and the absorber. The back-contact was made of molybdenum (1 µm) deposited on polyimide (PI) film with the thickness of 25 µm. The samples were prepared by Solarion AG, Germany. The exact composition of CIGS was a commercial secret of Solarion AG and was not disclosed. The sample (d) was a substrate covered with a molybdenum layer.

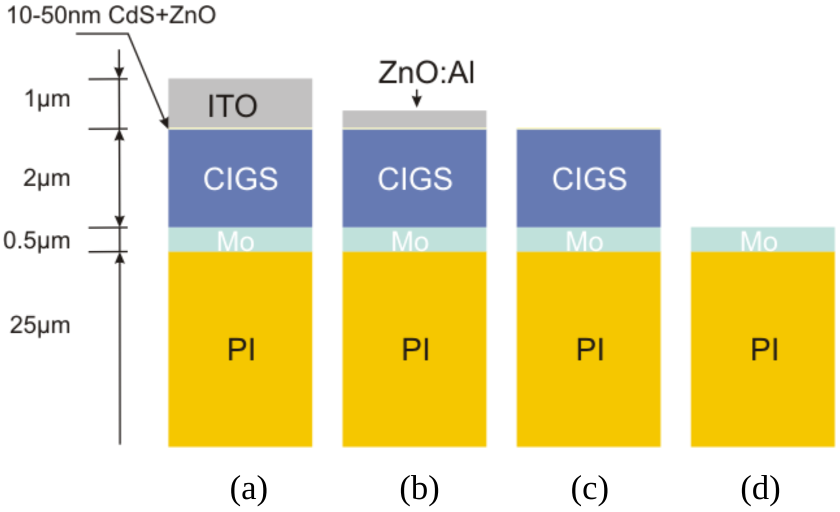

Fig. 47 The solar cell samples used in the scribing and ablation experiments.

6 PICOSECOND LASER PROCESSING OF THIN-FILM CIGS SOLAR CELLS

Material related to this chapter was published in **[A1]-[A8]** and **[C1]-[C25]**.

6.1 P1 process: scribing of molybdenum to form the back-contact

P1 process is defined as patterning of isolation lines in solar cell back-contact. It defines the number of cells and the cell area/width. Two types of experiments will be presented in this chapter: (i) ablation of the solar cell back-contact with the burst of laser pulses to define a working window of the laser ablation parameters; (ii) scribing experiments for the process optimization.

6.1.1 Ablation of Mo/PI structure

Series of samples were prepared by ablating craters and trenches in the thin-film Mo/PI structure with the picosecond laser fundamental harmonics. In case of 1064 nm wavelength, craters were made with a single laser pulse or a burst of pulses, consisting of 10, 100 or 1000. Experiments were repeated at least 10 times, and the laser pulse energy was changed between series of experiments. When the energy density (fluence) exceeded a certain value depending on material properties, the material was evaporated and removed. Experiments were performed on the molybdenum film and the polyimide substrate.

Table 9 Single pulse and multi-pulse (10, 100, 1000) ablation thresholds of molybdenum film and polyimide. Laser: PL10100, 10 ps, 1064 nm. Numbers 1, 10, 100, 1000 are for the number of laser pulses to ablate a crater.

	Ablation threshold F_{th} (J/cm^2)			
	1	10	100	1000
Molybdenum	-	5.89	0.9	0.14
Polyimide	1.59	-	0.44	0.13

The diameter of craters etched with laser pulses was measured and used to estimate the minimal laser fluence that corresponds to the start of material evaporation. We used a standard method to estimate the threshold discussed in section 4.4. The results of evaluations are shown in Table 9. We did not succeed in initiating ablation of the molybdenum film with a single laser pulse in the range of used pulse energies. When the film of molybdenum was irradiated by a burst of laser pulses, every pulse modified the surface and the film increasing its absorptivity. Therefore, the ablation threshold fell down with an increase in the number of pulses applied to irradiation. The variation can be expressed by an accumulation parameter [96] with a typical value for bulk metals of ξ =0.9–0.7.

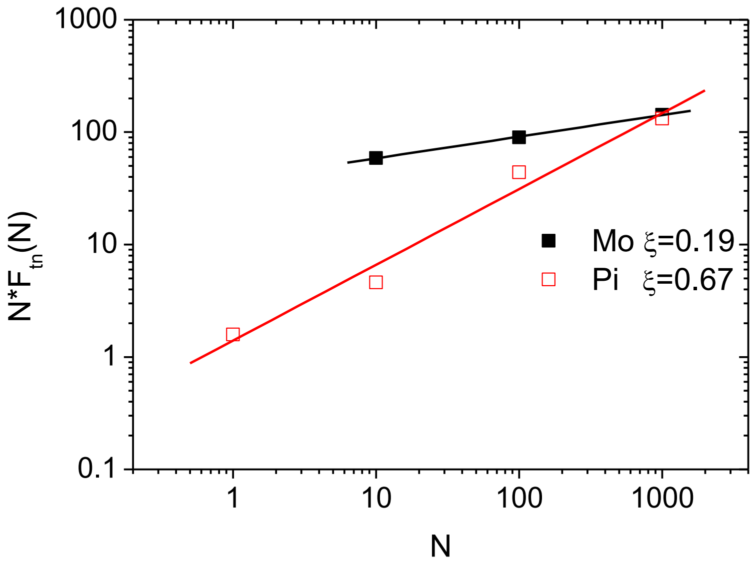

Fig. 48 Relation between the number of laser pulses N used to ablate a crater and the multi-pulse ablation threshold of molybdenum film and the polyimide substrate.

Evaluation of the accumulation parameter was performed for the molybdenum film and polyimide. Results are shown in Fig. 48. Our value for the molybdenum film is quite low (ξ =0.19), probably because of limited heat dissipation in the thin film. Polyimide experienced less variation in its absorption properties. Its ablation threshold also fell down with a number of laser pulses applied, but the effect was less prominent. Ablation properties of both materials became closer in the multi-pulse regime, making selective removal more complicated. Therefore, we limited an overlap of laser pulses in the scribing regime when trenches were produced in the films.

6.1.2 Scribing of Mo/PI structure

As the ablation thresholds of molybdenum and polyimide were close to each other at high beam overlap, we limited the experiments to a high translation speed when only a few laser pulses affected the same area of the film. Moreover, a high processing speed is preferable for the application. Using the infrared 1064 nm laser radiation, the molybdenum film was removed from the substrate. The metal was not evaporated but formed ridges from melt on rims of the processed trench (Fig. 49a, Fig. 50).

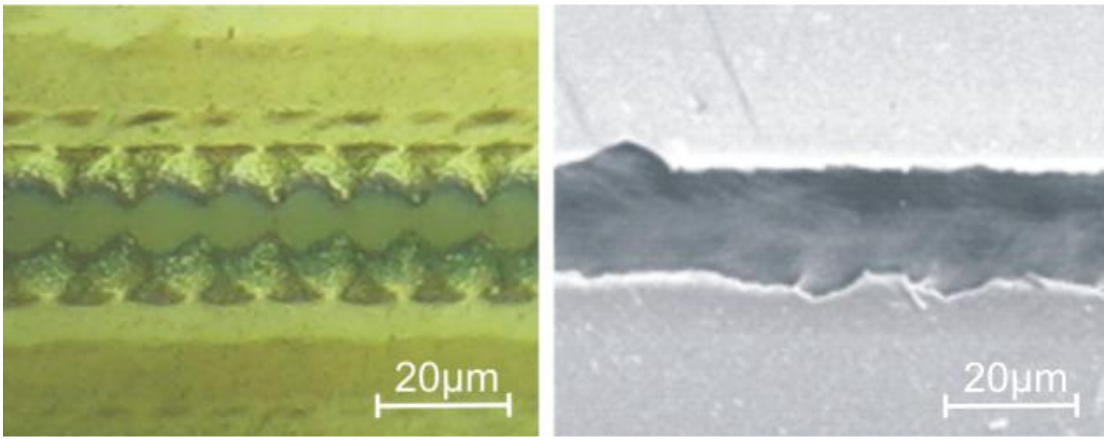

(a) (b)

Fig. 49 Pictures of trenches ablated with the laser: (a) Optical microscope picture (laser: λ = 1064 nm, 2.4 W, 50 kHz, translation speed 600 mm/s); (b) SEM picture (laser: λ = 355 nm, 2.35 W, 100 kHz; translation speed 600 mm/s).

The substrate was damaged when the translation speed was below 600 mm/s at the 50 kHz pulse repetition rate. At a translation speed higher than 700 mm/s, the beam overlap was too small to completely remove the metal along the trench. As the Gaussian spatial profile of the laser beam was used in experiments, central part of the laser spot tended to penetrate into polyimide. Flattening of the profile should help to remove the layer smoothly and prevent damage of Mo in the center of scribed trench. Similar experiments were performed using laser radiation converted to ultraviolet (UV) at the 355 nm wavelength. Removal of the metal film by evaporation from the polymer substrate with a low melting temperature tended to damage the substrate by the high intensive center of the laser spot. The main difference of the processing quality using the UV radiation was clean edges of trenches without appreciable melt formation (Fig. 49b).

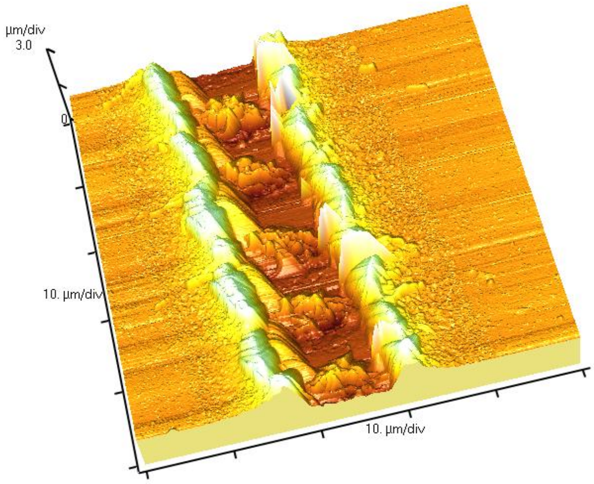

Fig. 50 AFM picture P1 scribe (laser: λ = 1064 nm, 2.4 W, 50 kHz, translation speed 600 mm/s).

6.1.3 Conclusions

1. Ablation properties of both molybdenum and polyimide materials became closer in the multi-pulse regime, making selective removal of the Mo film more complicated. Therefore, the process should be optimized for the low pulse-overlap regime.
2. Narrow processing windows of laser fluence and pulse overlap were estimated for both 1064 nm and 355 nm wavelengths of laser radiation to scribe the molybdenum back-contact on the substrate.

6.2 P2, P3 processes: exposure of the molybdenum back-contact

P2, P3 processes are defined as the processing of complete solar cell structure to open the Mo back-contact. Three different types of solar cell materials were laser-processed to open the Mo back-contact. Two types of experiments are presented in this chapter: (i) ablation of the solar cell samples with a burst of laser pulses to define a working window of the laser ablation parameters; (ii) scribing experiments for the process optimization.

6.2.1 Ablation of the absorber and front-contact layers to expose the molybdenum back-contact

The light absorbing layer of $CuIn_xGa_{(1-x)}Se_2$ deposited on the back-contact should be structured forming parallel trenches in it. We used a complete structure of layers in our experiments to estimate the processing regimes. The aim at this research was to remove all the top layers, including CIGS and to expose the molybdenum back-contact. The first experiments included ablation of craters with 2 and 10 laser pulses with different pulse energies at 1064 nm wavelength.

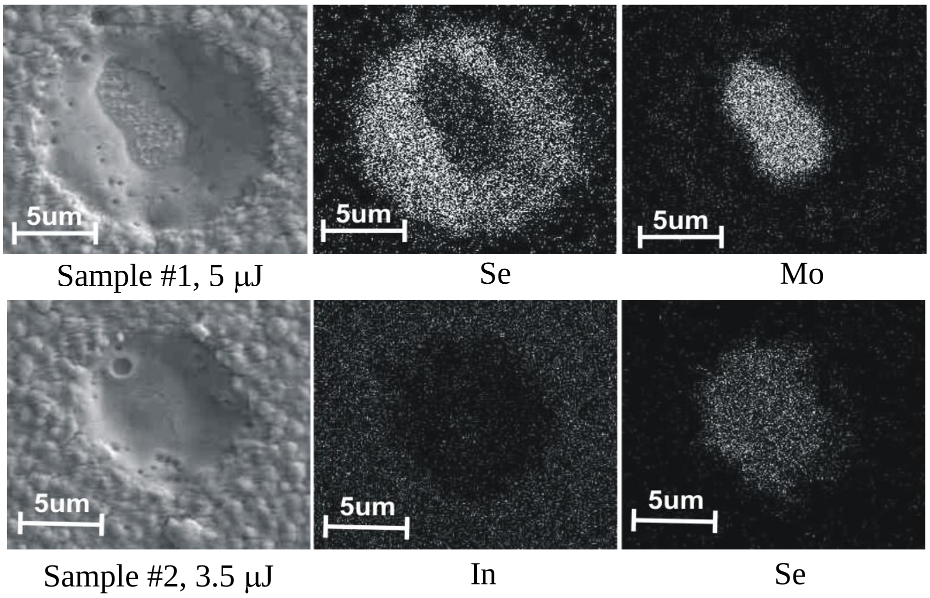

Sample #1, 5 μJ Se Mo

Sample #2, 3.5 μJ In Se

Fig. 51 SEM pictures and EDS maps of the craters ablated with 10 laser pulses with the energy of 5 μJ and 3.5 μJ. (Laser: λ=1064 nm, ITO/ZnO/CdS/CIGS/Mo/PI).

Ten pulses corresponded to the value of the laser beam overlap when the quality of trenches was the best without a significant damage to the polyimide substrate. The samples were investigated with SEM using the X-ray electron dispersion spectrometer because visual contrast did not allow discrimination of differences in chemical composition of layers. Fig. 51 presents comparison of the SEM pictures with the EDS maps of spatial distribution of particular chemical elements in a close surrounding of the laser-made craters.

By ablating with the pulse energy of 3.5 μJ, concentration of indium decreased and a signal from Se atoms appeared at the center of the crater. The top layer of conducting ITO was evaporated and the CIGS layer was exposed. Use of a higher pulse energy (5 μJ) exposed the CIGS layer in a larger area but in the central part of the crater, where the laser intensity was higher, the whole material was evaporated and molybdenum back-contact was exposed. At the pulse energy of 20 μJ, carbon atoms from the polymer were found in EDS spectra.

To investigate laser wavelength effects, two types of experiments were realized with ablation using 2 and 10 pulses per spot with 1064 nm and 532 nm wavelengths at different laser fluences. Typical SEM images of multi-pulse ablation and exposure of the Mo back-contact with different wavelengths are shown in Fig. 52.

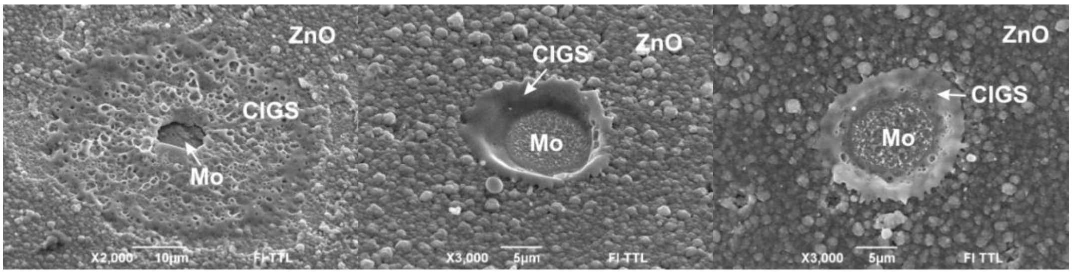

(a) (b) (c)

Fig. 52 SEM images of Mo layer exposure in ZnO:Al/ZnO/CdS/CIGS/Mo/Pi structure by laser pulses: (a) 44 μJ, 2 pulses@1064 nm; (b) 2 μJ, 10 pulses@1064 nm, (c) 2 μJ, 10 pulses@532 nm.

The threshold values for the laser fluence required to remove the top-contact and absorber layers to expose the molybdenum film as well as the beam waist on the processed surfaces were evaluated by the method proposed by Liu [95] for Gaussian beams and are shown in Table 10. The highest thresholds to expose the molybdenum layer for both wavelengths were found for the structure of ITO/ZnO/CdS/CIGS/Mo/PI with the thickest top-contact of 1 µm. For the structure of ZnO:Al(350 nm)/ZnO/CdS/CIGS/Mo/PI, the Mo exposure threshold values were lower due to the thinner top-contact. The lowest threshold was found for the structure without a top-contact of ZnO/CdS/CIGS/Mo/PI.

Table 10 The threshold fluencies for exposure of the molybdenum back-contact and beam waist estimated from the crater ablation in three types of CIGS solar cells using picosecond laser radiation at 1064 nm and 532 nm wavelengths.

	2 pulses		**10 pulses**	
1064 nm	Mo exposure threshold, J/cm^2	Beam waist, µm	Mo exposure threshold, J/cm^2	Beam waist, µm
ITO/ZnO/CdS/CIGS/ Mo/PI	-	-	1.3	6.3
ZnO/CdS/CIGS/ Mo/PI	-	-	0.84	7.8
ZnO:Al/ZnO/CdS/CIGS/ Mo/PI	-	-	0.94	6.5
532 nm				
ITO/ZnO/CdS/CIGS/ Mo/PI	19.4	8.9	1.3	7.1
ZnO/CdS/CIGS/ Mo/PI	4.7	7.4	0.8	5.9
ZnO:Al/ZnO/CdS/CIGS/ Mo/PI	16.7	7.7	1.05	6.1

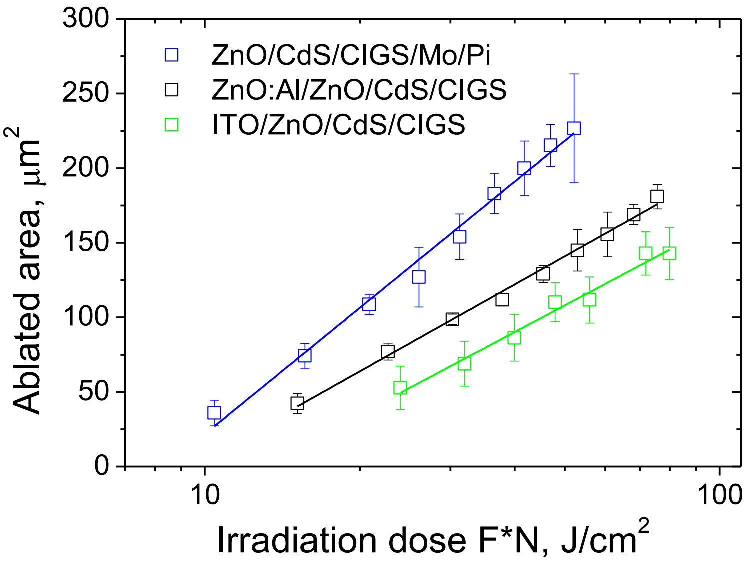

(a) 1064 nm wavelength

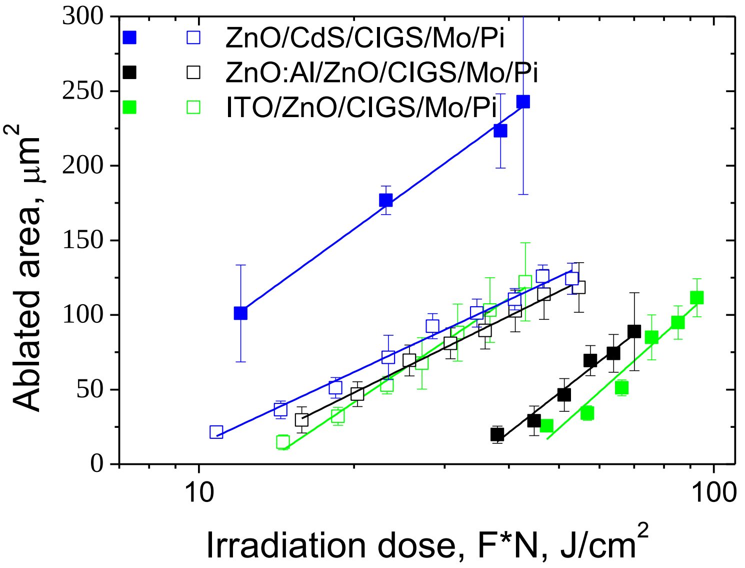

(b) 532 nm wavelength

Fig. 53 Relationship between the exposed area of the Mo layer and the accumulated irradiation dose for 2 (*solid dots*) and 10 (*open dots*) pulses at: (a) 1064 nm wavelength, (b) 532 nm wavelength.

The relationship between the exposed area of the Mo layer and the accumulated irradiation dose for 2 and 10 pulses for both wavelengths is shown in Fig. 53. The irradiation doses required for opening the Mo back-contact at 1064 nm and 532 nm wavelengths were found to be similar for the same structures of CIGS solar cells, although the ablation quality was different.

A larger melted area of the CIGS layer was spotted at the edges of the crater when ablating with low energy laser pulses at 532 nm wavelength, although melted CIGS was observed at both 1064 nm and 532 nm wavelengths. At both wavelengths, a few high energy laser pulses peeled the top-contact leaving extensive melt of the CIGS. While ablating CIGS material with a burst of low energy pulses, the melted area was significantly reduced. A higher overlap of laser pulses slows down the scribing process. Therefore, for the real scribing process, it means that lasers with a high repetition rate should be applied and the laser pulse energy could be focused to an elliptical spot [63] or split into a few channels to increase the overall process speed.

Wavelength-dependant ablation behavior was observed in the experiments. As CIGS solar cell is a multi-layer structure and is made of different materials the ablation properties of single layer can vary a lot. The P3 patterning requires ablation of the whole top layer to expose the Mo back-contact and selection of optimal wavelength is very important. For this modeling of laser radiation absorption will be presented in next section.

6.2.2 Modeling of the energy coupling and laser-induced stress

Selection of the right laser wavelength is important to keep the energy coupling in a well defined volume at the interlayer interface. The finite element method using COMSOL Multiphysics packages was applied to simulate the process. The modeling was split into a few stages, including the laser energy coupling by electrons, evolution of the electron and lattice temperatures according to the two-temperature method and stress induced by rapid local heating of the materials. All simulations were performed for three different CIGS solar cell structures as well as for a set of laser wavelengths available at the laboratory.

The laser energy coupled inside the films can be found by solving the absorptivity equation (16) (see section 3.1).

Each material (layer j) in a stack of a CIGS structure was described by its own set of parameters (n_j, k_j) [102], and each layer was sliced into multiple sub-layers. Boundary conditions included transmission and back-reflection at inner interfaces of the stack, and were considered automatically using transmission matrixes (31) for each layer as described in section 3.4. Equation (16) was solved numerically and its solution was the energy locally coupled from an incident laser pulse inside the material stack *Q(x)* – energy losses in a sub-layer. The losses depended on the longitudinal coordinate (x) and time relative to the laser pulse. *Q(x)* describes the local energy deposition at each point of the beam propagation along the x-axis, perpendicular to the CIGS structure surface.

$$Q(x,t) = \{\ Q(x),\quad t \le \Delta\tau_L \ \ / \ \ 0,\ t > \Delta\tau_L\}. \tag{40}$$

The laser pulse was described by the Heaviside delta function with the pulse duration of $\Delta\tau$ = 10 ps. Therefore, the energy coupling took place only within this time span. Results of simulation in CIGS with the ITO top-contact for different laser wavelengths are presented in Fig. 54.

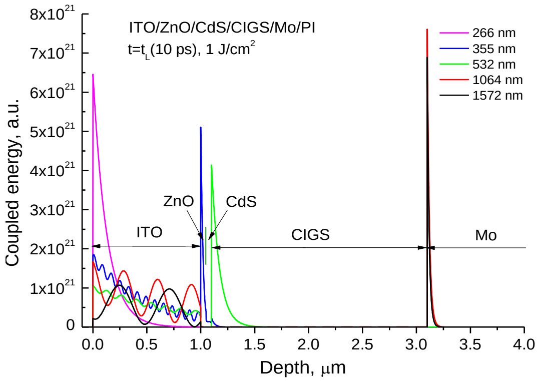

Fig. 54. Distribution of energy coupled from a laser pulse inside the CIGS structure, depending on wavelength of laser radiation. Laser pulse duration - 10 ps; fluence - 1 J/cm^2.

Reflection at inner interfaces in partially transparent films caused periodical modulation of the absorbed laser energy. UV radiation at 266 nm was absorbed in a thin layer close to the outer surface of ITO and selectivity of the ablation process was hardly to be expected. Radiation with longer wavelength pulses penetrated into the CIGS solar cell stack and the penetration stopped in a layer with high absorption: CdS for 355 nm, CIGS itself for 532 nm. The infrared light can reach the molybdenum back-contact. Localization of the coupled energy at inner interfaces was a key to control selectivity of the laser scribing process.

Numerical simulation of the temperature distribution in the CIGS solar cell structures after absorption of a laser pulse was performed depending on the wavelength of laser radiation in order to find out removal mechanisms of the transparent conductor and CIGS layers. Evolution of the electron and lattice temperatures inside the layers was simulated using the two-temperature model. The model predicts temporal and spatial evolution of the lattice and electron temperatures in the irradiated material by two coupled heat diffusion equations (see section 3.3).

An energy source Q is the coupled energy from the previous step of simulation. The temperature dependence of heat diffusion and capacity for electrons was approximated for all materials, excluding molybdenum, as:

$$C_e = A_e T_e, \text{where } A_e = 71 \text{ Jm}^{-3}\text{K}^{-2}. \tag{41}$$

Thermal conductivity of electrons:

$$\kappa_e = \kappa_{e,0} \frac{T_e}{T_l}, \text{where } \kappa_{e,0} = 318 \text{ Wm}^{-1}\text{K}^{-1}. \tag{42}$$

The electron-phonon coupling coefficient was kept constant and equal to g=2.1 10^{16} W/m^{3}K [14]. More exact data of $C_e(T_e)$ and $g(T_e)$ for electrons in molybdenum are taken from the specialized web site prepared by Z. Lin and L. Zhigiley [103]. Other parameters of materials were collected from different sources and are presented in section 3.5.

Longitudinal distribution of the electron and lattice temperatures inside the ITO/CIGS/Mo/PI structure at the end of a laser pulse (10 ps) for different wavelengths of laser radiation is shown in Fig. 55. Numerical simulation shows that the 532 nm and 355 nm laser radiation is well absorbed at the interface between the upper ITO contact and the CIGS layer which may facilitate the material removal with a high layer selectivity. The 266 nm laser radiation is absorbed by ITO which leads to a direct material removal by evaporation with a poor layer selectivity.

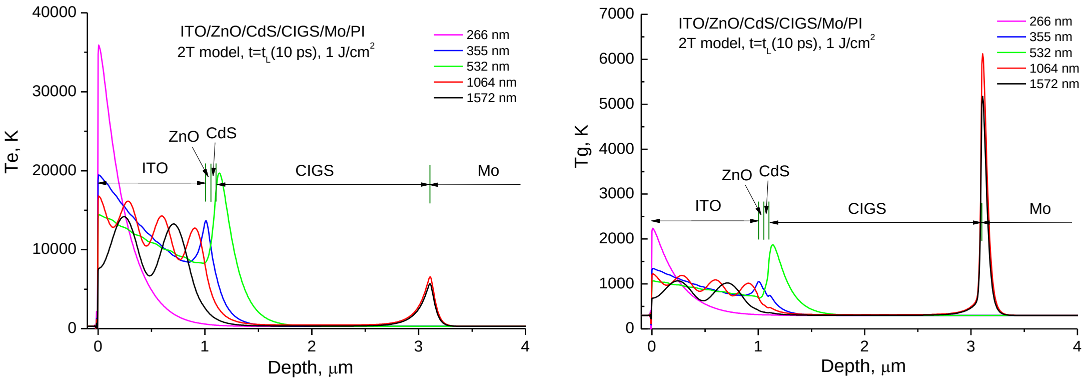

(a) (b)

Fig. 55. Distribution of electron (a) and lattice (b) temperatures at the end of the laser pulse inside the CIGS structure depending on the wavelength of laser radiation. Laser pulse duration - 10 ps; fluence - 1 J/cm^2.

For the infrared 1064 nm and 1572 nm radiation, the high temperature of the molybdenum surface and good selectivity of CIGS layer removal can be predicted (see Fig. 55) because the laser radiation with these wavelength pulses penetrates through the absorber and is well absorbed at the CIGS-Mo interface.

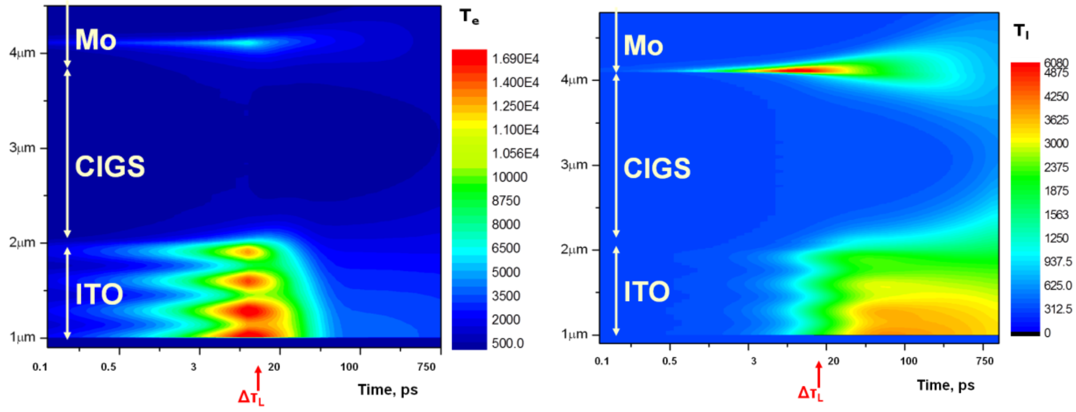

(a) (b)

Fig. 56 Evolution in time of electron (a) and lattice (b) temperature distribution inside the CIGS structure for 1064 nm laser radiation. Laser pulse duration - 10 ps; fluence - 1 J/cm^2.

High temperature at the CIGS-molybdenum interface remains over a time span of a few hundred picoseconds, while the CIGS layer itself is kept cold all the time (see Fig. 56). This can prevent the CIGS material from thermal degradation. Such localization of the heat is possible only by excitation with ultra-short laser pulses.

SEM images in Fig. 57 show experimental CIGS ablation with 532, 1064 and 1572 nm wavelength pulses. In case (a), the 532 nm radiation peels the ITO top contact leaving the CIGS layer exposed, although the ablation of the CIGS layer is not accurate due to direct absorption of the laser light. In case (b), the 1064 nm wavelength laser pulses were well absorbed at the CIGS/Mo interface and clean exposure of Mo layer with the 1064 nm irradiation was observed. In case (c), the 1572 nm wavelength laser pulse energy was not sufficient to fully remove the CIGS layer.

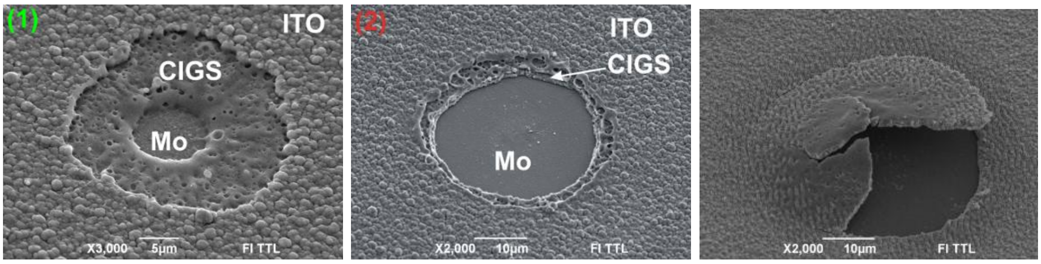

(a) 45 μJ, 2 pulses, 532 nm

(b) 25 μJ, 2 pulses, 1064 nm

(c) 18 J, 5 pulses, 1572 nm

Fig. 57 SEM images of craters ablated in ITO/ZnO/CdS/CIGS/Mo/PI (a,b) and ZnO:Al/ZnO/CdS/CIGS/Mo/PI (c) illustrating effect on the selectivity in energy coupling to material removal quality: ITO can be cleanly removed at 532 nm and CIGS – at 1064 nm or 1572 nm wavelength laser pulses.

To evaluate the mechanical stress generated in layers under the fast laser heating, the approximate solution of the thermo-elasticity equation for a round plate with fixed edges may be used [104]:

$$\sigma_{r\max} = \frac{E\alpha_l \Delta T}{2(1-\nu)}, \tag{43}$$

where E is the Young module; α_l is the linear thermal expansion; ν is the Poisson ratio.

A rapid temperature increase leads to the local thermal strain. According to our simulations, the temperature rise ΔT can be as high as 6000 K. This results in stress values within different layers in the range of tens of GPa. These values are much higher than the expected yield stress of the materials. The irradiated area of the sample experiences plastic deformations and can be fractured under laser-induced thermal stresses. Similar approach was applied for modeling the nanosecond laser scribing of a-Si solar cells [43].

The top-contacts made of ITO and ZnO:Al have similar optical properties for visible light (532 nm). However, their behavior under laser irradiation is completely different. The reason is a tensile strength of the materials: 415 MPa for ZnO [105] versus 130 MPa for ITO [106]. Stress induced by the pulsed laser heating was high enough to initiate spallation of the ITO layer, but not strong enough for ZnO film ablation. A clean removal of all layers from the molybdenum back-contact is important for P3 scribing. The infrared laser beam penetrates into the inner CIGS-Mo interface, causing local heating. If the energy coupled at the interface exceeds the mechanical strength of all upper layers, spallation may occur as in the case of Fig. 57b. The 1064 nm radiation is partially absorbed in the films, therefore melting is still evident on the edges. Radiation with the 1572 nm wavelength penetrates up to the CIGS-Mo interface without significant losses, and the front spallation is triggered by the stress induced by a laser pulse of that wavelength (Fig. 57c).

6.2.3 Processing with the 1064 nm wavelength

When ablating with a burst of high-energy laser pulses, extensive melting of the CIGS layer was observed. A further increase of the pulse energy helped to remove the damaged layers by material lift-off process, although no such effect was observed in the scribing regime. Lowering the pulse energy and applying a longer pulse burst facilitated an increase in selectivity of layer ablation and significantly reduced melt formation in the CIGS layer (see Fig. 58). Such conditions were also observed in the scribing regime.

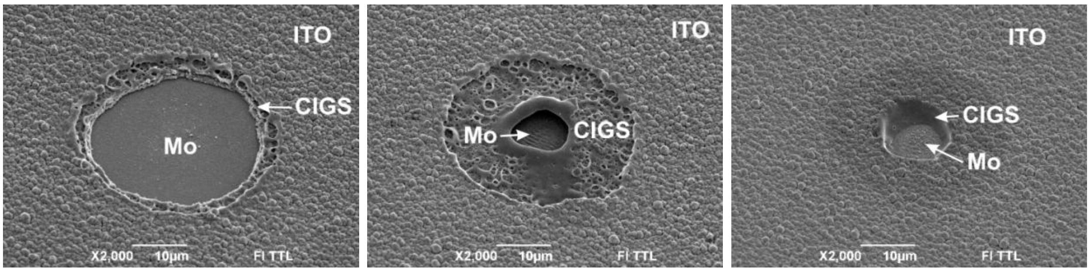

25 μJ, 2 pulses 18 μJ, 2 pulses 2 μJ, 10 pulses

Fig. 58 SEM images of craters ablated in ITO/ZnO/CIGS/Mo/PI structure using the 1064 nm radiation.

Smooth trenches were scribed in all three types of solar cell materials with a low laser power, high pulse overlap and single pass beam scanning to open the molybdenum back-contact. Typical laser scribes are shown in SEM images below. In case of the solar cell structure with the ITO top-contact, some debris and ripple formation were observed in the exposed molybdenum layer, although all the layers had sharp interfaces at the edges of the scribed trench (see Fig. 59).

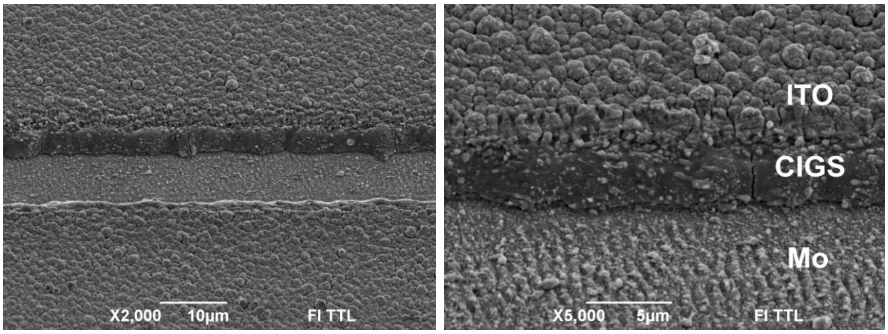

Fig. 59 Laser scribes in ITO/ZnO/CdS/CIGS/Mo/PI structure, 1064 nm wavelength**,** 450 mW, 100 kHz, 4.5 μJ, 90 mm/s, single pass.

Use of gentle ablation with a low laser power and high pulse overlap together with two-pass scanning allowed us to achieve very smooth laser scribes with the high layer selectivity in ITO/ZnO/CdS/CIGS/Mo/PI structure, although process productivity was low (see Fig. 60).

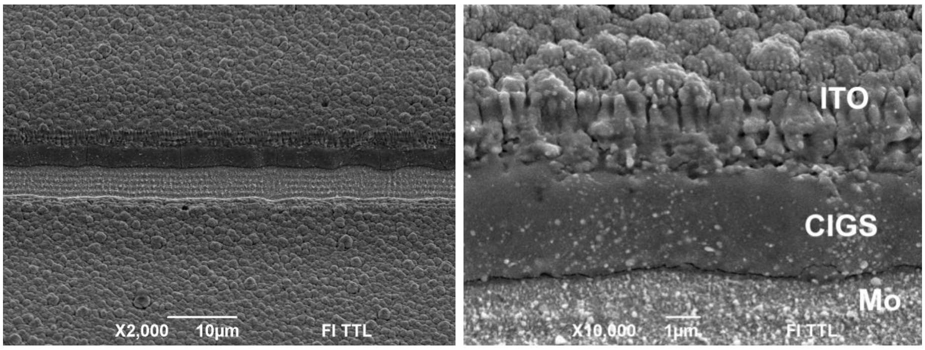

Fig. 60 Laser scribes in ITO/ZnO/CdS/CIGS/Mo/PI structure, 1064 nm wavelength, 100 mW, 100 kHz, 1 µJ, 100 mm/s 2 scans.

In case of structure with ZnO:Al top-contact (ZnO:Al/ZnO/CdS/GIGS/Mo/PI), ablation with a burst of laser pulses was also applied. The situation was the same as for samples with the ITO top-contact. When ablating with a burst of high energy laser pulses, extensive melt of the CIGS layer was observed. Lowering the pulse energy and applying a longer pulse burst facilitated an increase in selectivity of the layer ablation and significantly reduced melt formation in the CIGS layer.

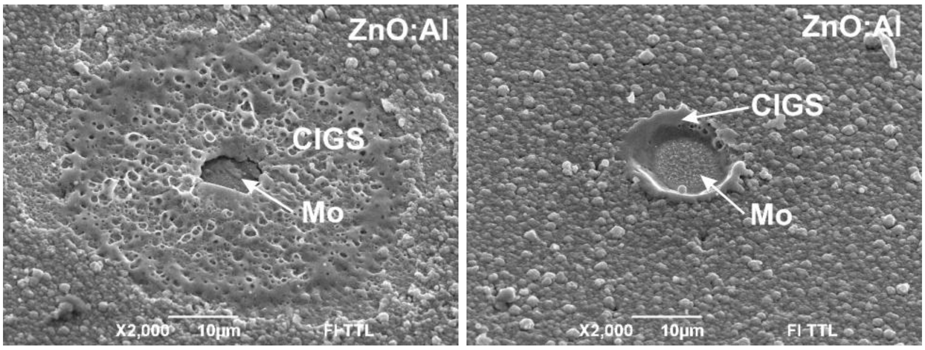

44 µJ, 2 pulses 2 µJ, 10 pulses

Fig. 61 SEM images of craters ablated in ZnO:Al/ZnO/CIGS/Mo/PI structure.

A smooth removal of the upper layers was achieved with a low laser power and high pulse overlap in a single pass scanning. Multi-pass scanning with the lower laser power did not help to increase the scribing quality. Some melt formation was still observed at the edges of the scribe due to the Gaussian beam distribution.

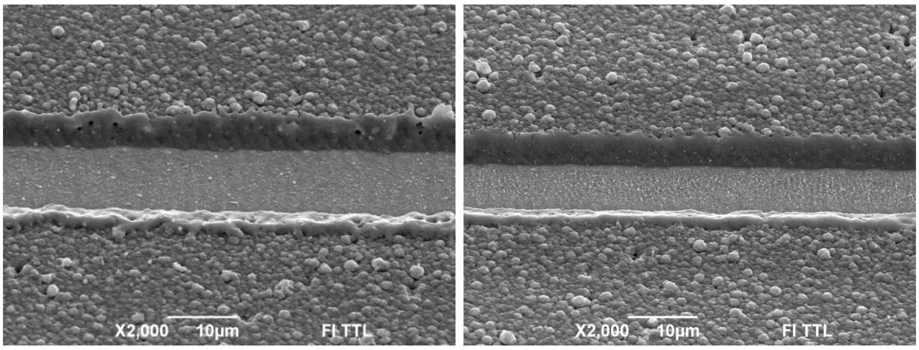

600 mW, 100 kHz, 6 µJ,
200 mm/s single pass

150 mW, 100 kHz, 1.5 µJ,
200 mm/s, 2 scans

Fig. 62 P3 laser scribes in ZnO:Al/ZnO/CdS/GIGS/Mo/PI structure.

The EDS analysis did not detect any deposition of melted molybdenum at the edges of the scribed trench, all the layer interfaces had sharp edges.

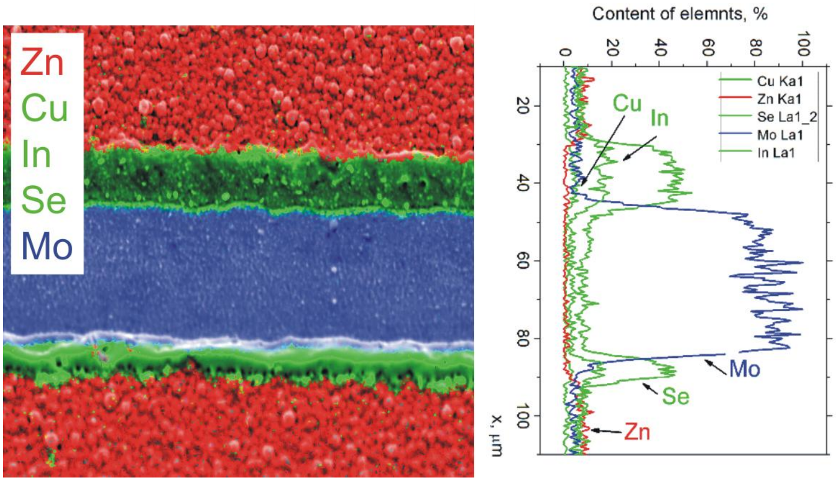

Fig. 63 EDS analysis of the laser scribe in ZnO:Al/ZnO/CdS/CIGS/Mo/PI sample,1064 nm wavelength, 600 mW, 100 kHz, 6 µJ, 200 mm/s single pass.

In case of the structure without a top-contact (ZnO/CdS/CIGS/Mo/PI), the ablation experiments revealed the same behavior as in previous samples when ablating with a burst of laser pulses. Ablating with a burst of high energy laser pulses, an extensive melt of the CIGS layer was observed. Lowering the pulse energy and applying a longer pulse burst facilitated an increase in selectivity of layer ablation and significantly reduced melt formation in the CIGS layer.

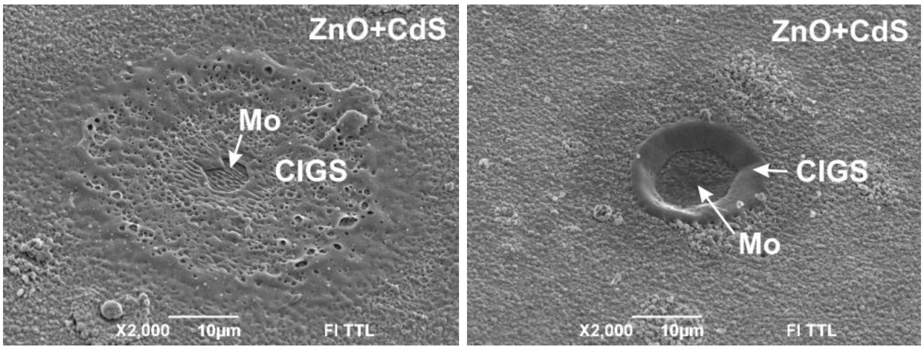

18 μJ, 2 pulses

2 μJ, 10 pulses

Fig. 64 SEM images of craters ablated in ZnO/CdS/CIGS/Mo/PI structure with 1064 nm wavelength.

Smooth exposure of the molybdenum layer was observed by single and multi-pass scanning methods. The multi-pass scribing left narrower melt formation zones at the edges of the scribes compared to the single-pass scribing, although the productivity was lower.

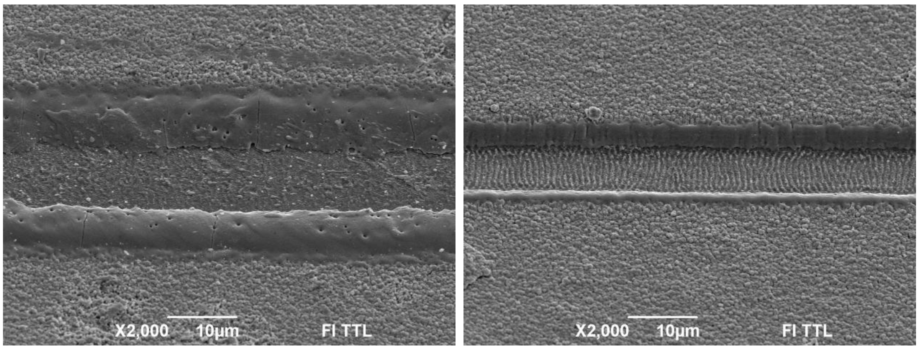

550 mW, 100 kHz, 5.5 μJ, 300 mm/s, single pass.

75 mW, 100 kHz, 0.75 μJ, 300 mm/s, 10 scan.

Fig. 65 Laser scribes in ZnO/CdS/GIGS/Mo/PI structure ablated with the 1064 nm wavelength.

In all samples, use of the 1064 nm laser wavelength enabled us to scribe with a low thermal damage to the surrounding material. For all samples, the average width of laser affected area at the edges of the scribes was 5.7 μm and taking in account both sides of the trench it reached 51 % of the total scribe width. Considering the cost of the industrial scribing device, the fundamental harmonics of the picosecond laser is the best choice.

6.2.4 Processing with 532 nm wavelength

Experiments with a burst of laser pulses at 532 nm revealed similar ablation behavior as processing with the 1064 nm wavelength. Ablation with high energy pulses caused pealing of the ITO and ZnO layers due to thermo-mechanical process. The ablation of the CIGS layer took place only in the center of the laser Gaussian beam (see Fig. 66).

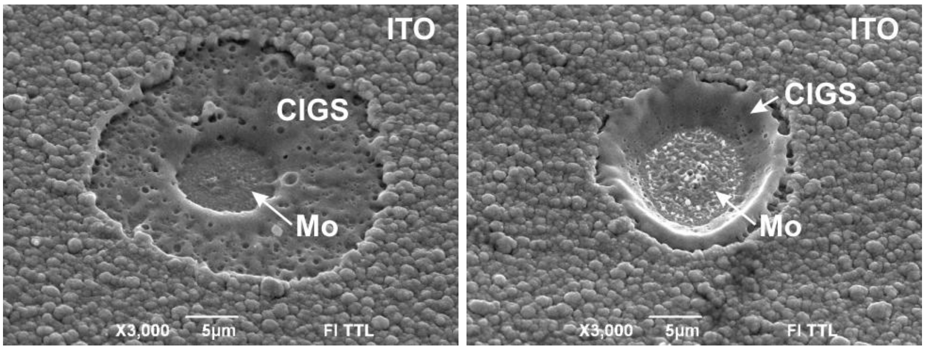

45 μJ, 2 pulses 3.4 μJ, 10 pulses

ITO/ZnO/CIGS/Mo/PI structure.

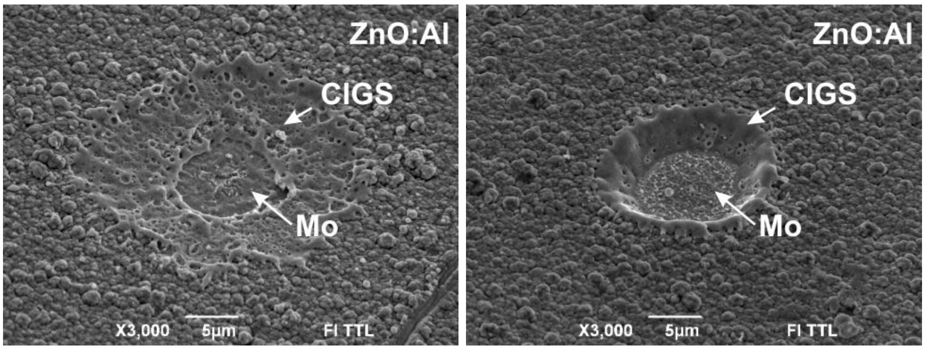

26 μJ, 2 pulses 2 μJ, 10 pulses

ZnO:Al/ZnO/CIGS/Mo/PI structure

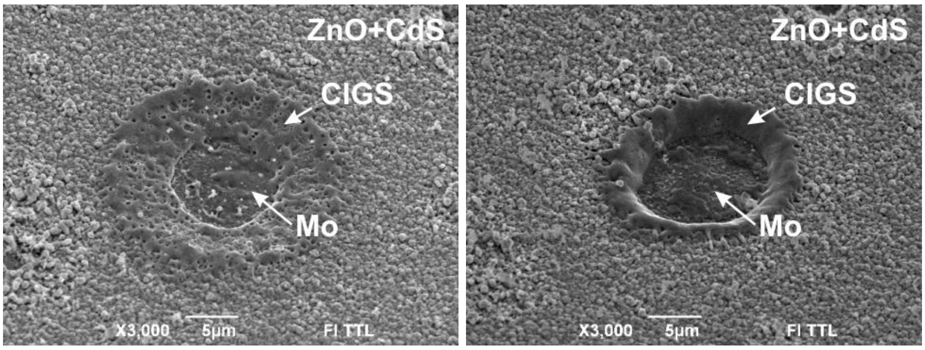

7.7 μJ, 2 pulses 2.9 μJ, 10 pulses

ZnO/CdS/CIGS/Mo/PI structure

Fig. 66 SEM images of craters ablated in CIGS structures with the 532 nm wavelength.

Lowering the pulse energy and applying a longer pulse burst facilitated in an increase of ablation quality. The CIGS layer was smoothly removed with the low melt area formation at the edges of the crater.

SEM images of scribes in the ITO/ZnO/CdS/CIGS/Mo/PI structure with the 532 nm radiation made by single and multiple scans are shown in Fig. 67.

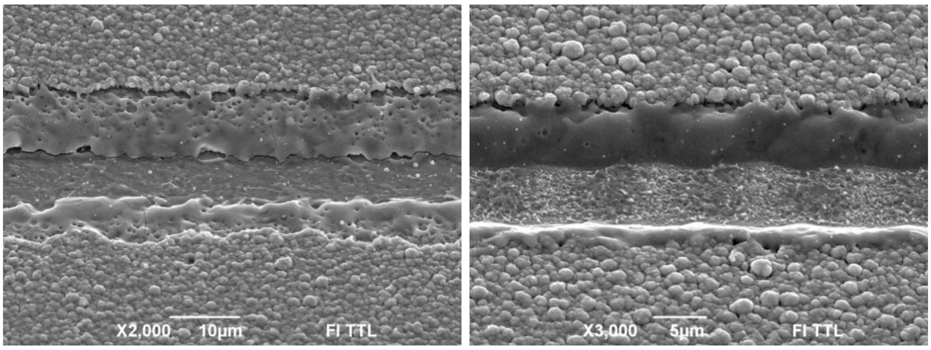

3 W, 100 kHz, 800 mm/s, single pass 100 mW, 100 kHz, 1 m/s, 9 scans

Fig. 67 Laser scribes in ITO/ZnO/CdS/CIGS/Mo/PI structure ablated with the 532 nm wavelength.

Using of the high average laser power to scribe the CIGS films with the ITO top-contact in a single scan led to peeling of the ITO layer over a wide area (width ~30 µm) while exposure of the Mo film by CIGS ablation was only 6 µm wide (see Fig. 67). A smooth scribe was achieved using 10 times reduced laser power and multiple scans. The width of exposed molybdenum was nearly the same, and the width of removed ITO was 13 µm. Edges of the scribe were smooth but the presence of remelted CIGS was obvious.

Similar results were achieved with ablation of ZnO:Al/ZnO/CdS/CIGS/Mo/PI and ZnO/CdS/CIGS/Mo/PI structures. Scribing with high pulse energies and single pass mode enabled forming the ~5 µm-wide melted area of the CIGS material on the edges of the formed trench. The molybdenum back-contact was uncovered smoothly, although some debris of the melted layers was observed in high resolution SEM images (see Fig. 68). When ablating with lower pulse energies and applying multi-pass scanning mode, the melted area of the CIGS material was reduced. Ripple structures were observed at the edges of scribed trench. Although gentle ablation with the multi-pass scanning enabled us to increase the scribing quality, the process time was significantly enlarged. For all samples the average width of laser affected area at the edges of the scribes was 6.2 µm and taking in account both sides of the trench it reached 61 % of the total scribe width.

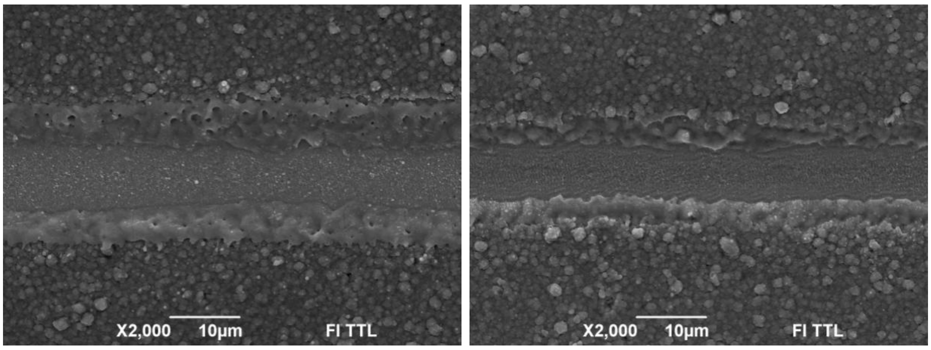

500 mW, 100 kHz, 200 mm/s single pass 50 mW, 100 kHz, 200 mm/s, 4 scans

ZnO:Al/ZnO/CdS/CIGS/Mo/PI structure

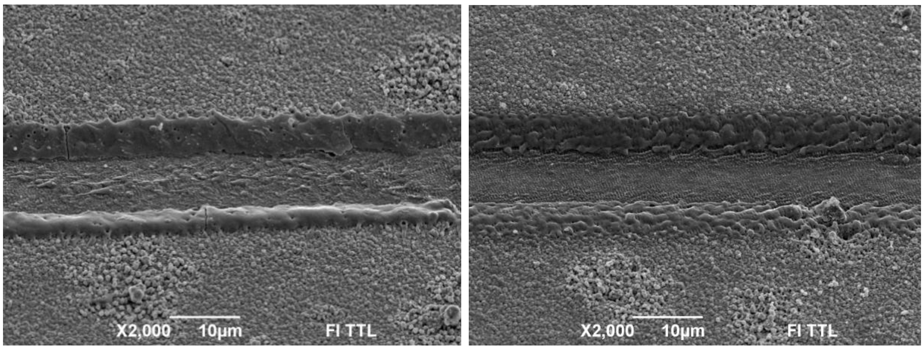

500 mW, 100 kHz, 270 mm/s single pass 50 mW, 100 kHz, 200 mm/s, 9 scans

ZnO/CdS/CIGS/Mo/PI structure

Fig. 68 Laser scribes in CIGS structures with 532 nm wavelength.

6.2.5 Processing with 355 nm and 266 nm wavelengths

The UV laser radiation (355 nm) was used to selectively scribe trenches in layers of the ITO/ZnO/CdS/CIGS/Mo/PI solar cell structure. The process parameters are presented in Table 11. Keeping the laser parameters the same and varying only the translation speed it was possible to find out the regimes of laser structuring in the CIGS multilayer system:

- to evaporate the upper electro-conducting layer of ITO;
- to remove the semiconducting film and expose the molybdenum back-contact (P3 process);
- to make an isolation trench by laser ablation of all films down to the polyimide substrate (edge isolation process);
- to cut a complete structure of the CIGS solar cell together with the substrate.

Table 11 Regimes of selective removal of layers and cutting of the CIGS multilayer structure. (Laser: P= 2.35 W, λ=355 nm, 100 kHz).

Regime	Scanning speed, mm/s	Process
#1	900	Removal of the ITO film
#2	380	Exposure of the Mo back-contact (P3)
#3	150	Isolation trench down to the polyimide foil
#4	35	Cutting of the CIGS multilayer

SEM pictures of trenches ablated in the CIGS structure at different regimes and distribution of main chemical components in the cross-section of trenches are shown below. The top-layer of ITO as well as the thin buffer layers of ZnO and CdS were cleanly removed at the regime #1 (Fig. 69). The Se and Cu signals were detected with the EDS at the bottom of the trench with a synchronous decrease in the concentration of In. The elements formed the absorber layer. Molybdenum and carbon were found at the background level.

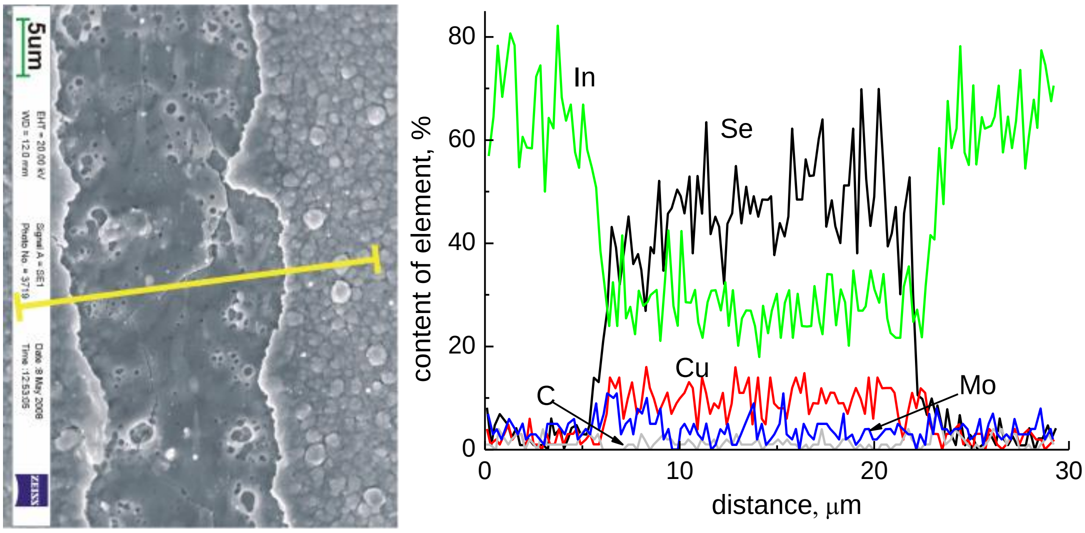

Fig. 69 SEM picture and EDS profile of a trench ablated in the ITO top layer to expose the absorber film. (Laser: 2.35 W, λ=355 nm, 100 kHz; translation speed 900 mm/s).

ITO has low absorption for the 355 nm radiation and thermal exfoliation prevails [107]. The surface of the CIGS layer shows some sings of melting in the central part of the trench. As the properties of the surface of CIGS strongly depend on the bulk stoichiometry [108], heating might affect electrical properties of CIGS and special photo-electrical experiments are planned for verification.

When the translation speed was reduced to 380 mm/s keeping all other processing parameters the same (Fig. 70), the laser was able to evaporate a CIGS film and expose the Mo back-contact. High signal of Mo atoms was detected with the EDS in the central part of the trench.

The trenches had no sharp edges. This is a consequence of the Gaussian spatial distribution of energy in the laser beam. Slopes of the trenches were formed of partially removed layers and included $CuIn_xGa_{(1-x)}Se_2$ at the bottom as quite strong signals of Se were detected with EDS. The trenches were narrow enough to ensure dense dislocation of separation lines between elements in solar cells. The upper layer of the top-contact was not affected outside the irradiation area.

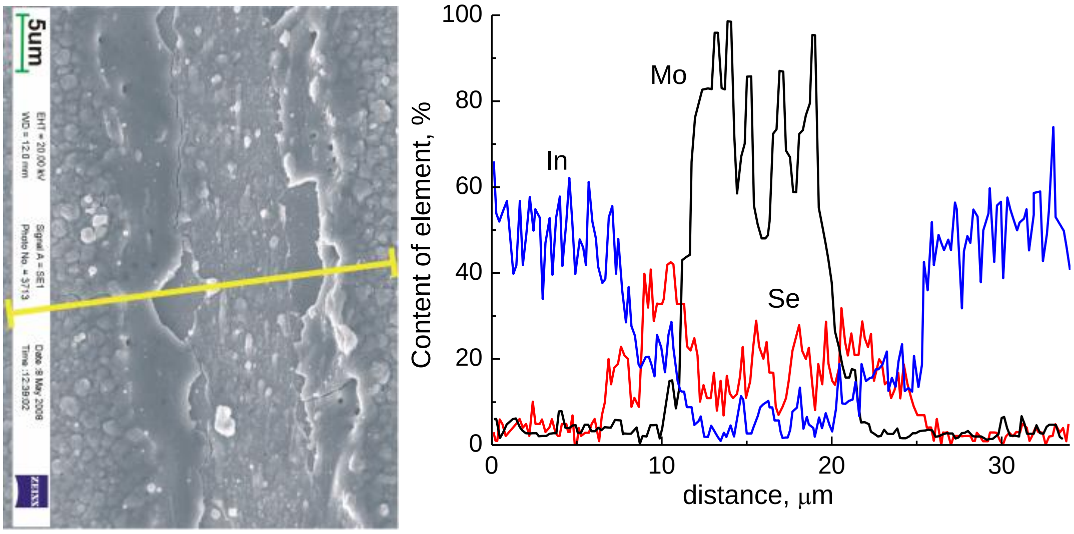

Fig. 70 SEM picture and EDS profile of a trench ablated down to the Mo layer to expose the back-contact. (Laser: 2.35 W, λ=355 nm, 100 kHz; translation speed 380 mm/s).

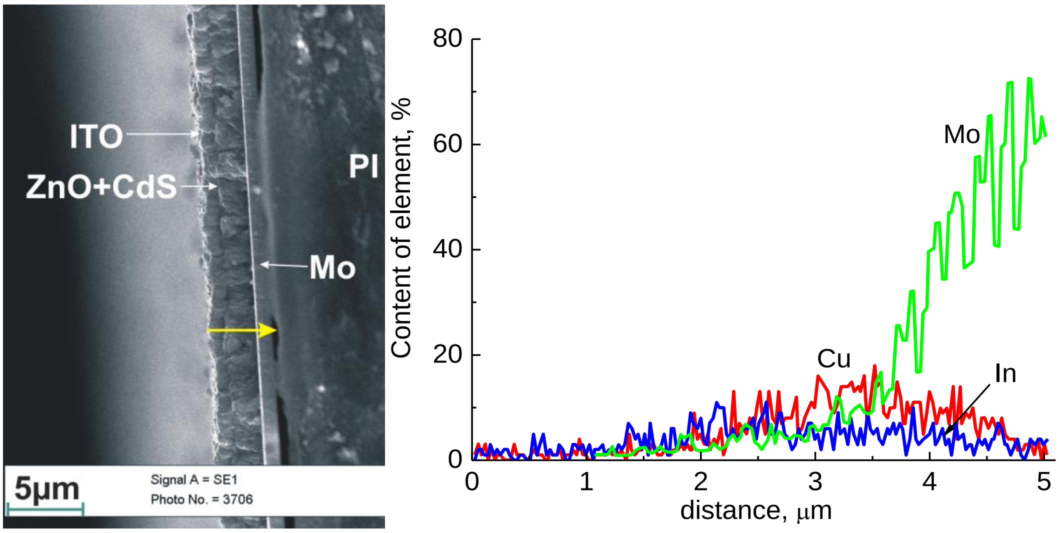

Fig. 71 Cross-section of the CIGS photovoltaic element cut with the laser and its chemical composition estimated by EDS. Arrow indicates the EDS scan direction. Length of the arrow is 5 μm. (Laser: 2.35 W, λ=355 nm, 100 kHz; translation speed 35 mm/s).

A slow translation speed (35 mm/s) was used to cut the whole CIGS/substrate structure with the picosecond laser. Cuts of this kind are not required in the real production cycle, but the EDS investigations of a cross-section provided information about the quality of laser processing. SEM picture of the cross-section of the multi-layer CIGS structure is shown in Fig. 71.

Separate layers can be easily recognized in the picture, which means that there was no mixing during the deposition cycle and the laser processing did not disturb regular position of the layers with sharp edges. J. Hermann et al. [14] estimated that processing of CIGS solar cells with nanosecond lasers resulted in spreading of molybdenum over the CIGS film creating short-circuits. The picosecond pulse duration was short enough to prevent extensive formation of the melt and no mixing of Mo with CIGS was found. The EDS signals of the main chemical components of CIGS were measured along the cut depth (indicated by arrow in Fig. 71). Atoms of molybdenum appeared in EDS spectra on the edge of the Mo layers and were spread towards the polyimide substrate (Fig. 71). The rise in the Mo concentration was at the same depth where concentrations of In and Cu atoms decreased.

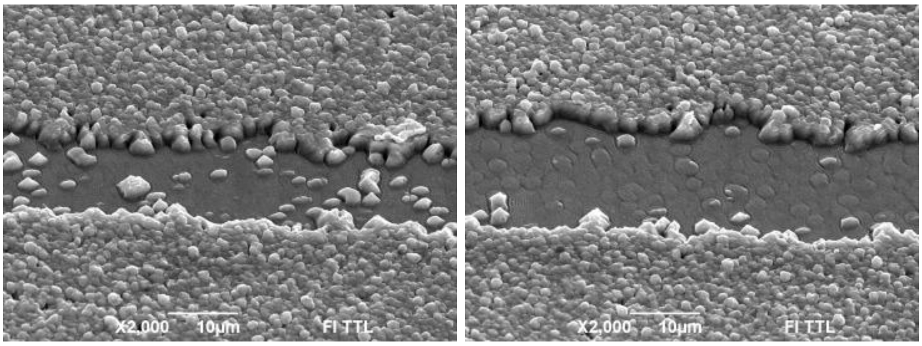

50 mW 75 mW

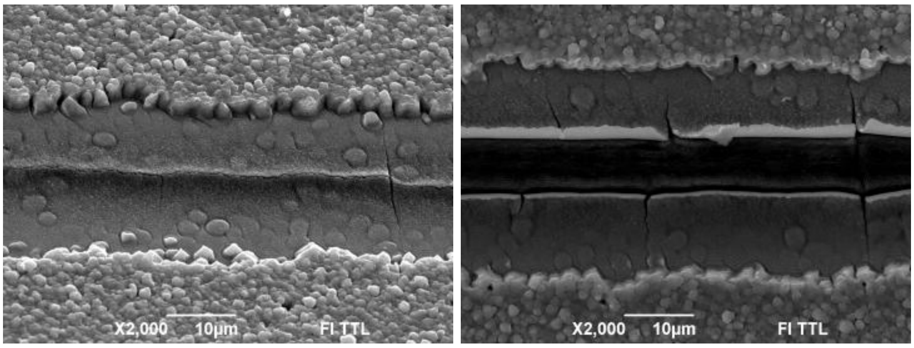

150 mW 200 mW

Fig. 72 The P3 scribe in ZnO:Al/ZnO/CIGS/Mo/PI versus laser power (355 nm, 50 kHz, 300 mm/s, 20 scan).

The Gaussian beam of the picosecond laser was used for processing of the ZnO:Al/ZnO/CdS/CIGS/Mo/PI structure with radiation of the wavelengths equal to 355 nm and 266 nm. Fig. 72 shows results of scribing with the 355 nm radiation depending on the mean laser power. Grains of CIGS remained in the trench at the low laser power, while the laser fluence in the central part was able to crack and exfoliate the molybdenum film at the high laser power.

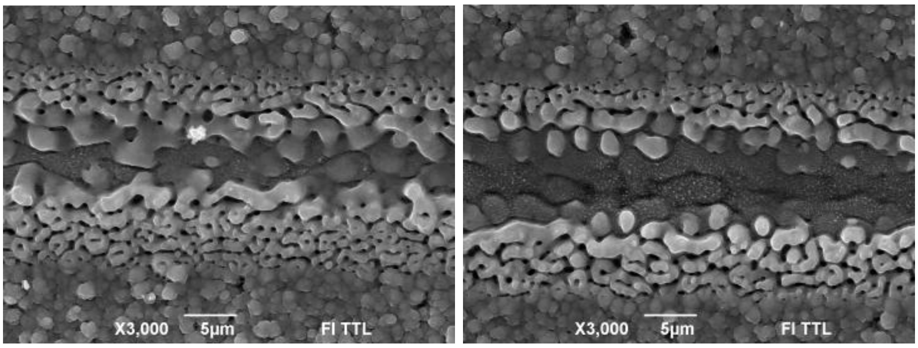

10 scan 16 scan

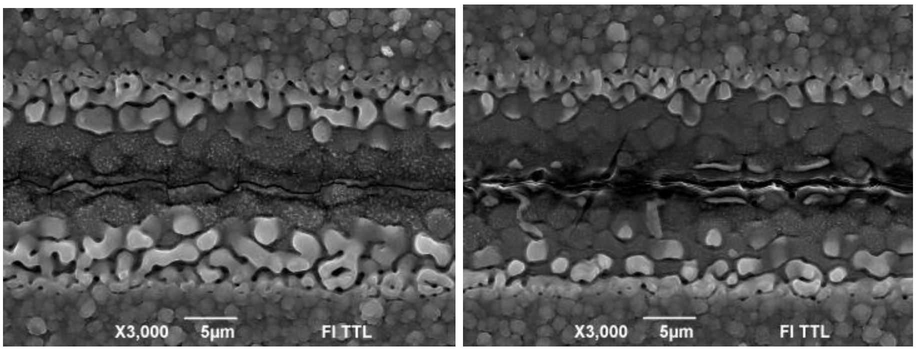

20 scan 30 scan

Fig. 73 The P3 scribe in ZnO/CIGS/Mo/PI versus a number of scans (266 nm. 50 kHz, 200 mm/s, 65 mW).

Results of laser scribing with the 266 nm radiation versus a number of scans are shown in Fig. 73. The 266 nm laser radiation had high absorption in the ZnO layer. Therefore, the energy was initially coupled by the film itself. The CIGS film was partially ablated at every scan. However, the tails of the Gaussian beam affected the CIGS grains. Transformations in the layer structure are evident from Fig. 73. The excessive number of scans led to the damage of the molybdenum layer underneath.

Optimization of the P3 scribing process in the ZnO/CIGS/Mo/PI solar cell system was possible only using the 355 nm laser radiation. Sharp edges of the trenches without damaging the metal film were achieved by removal of the CIGS grains (Fig. 74).

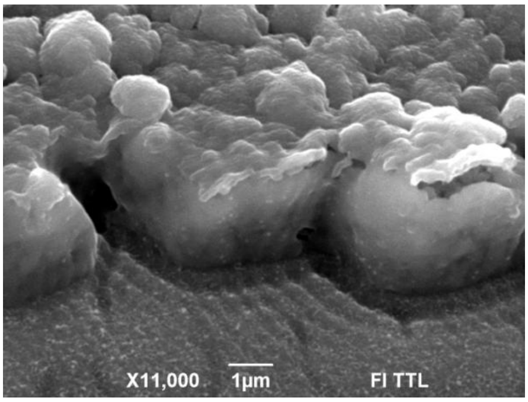

Fig. 74 Close view of edge of the P3 scribe in ZnO/CIGS/Mo/PI with the 355 nm radiation at optimized parameters.

A better quality of processing with the 355 nm radiation compared with the 266 nm radiation was confirmed by the EDS profiles of the laser scribes (Fig. 75).

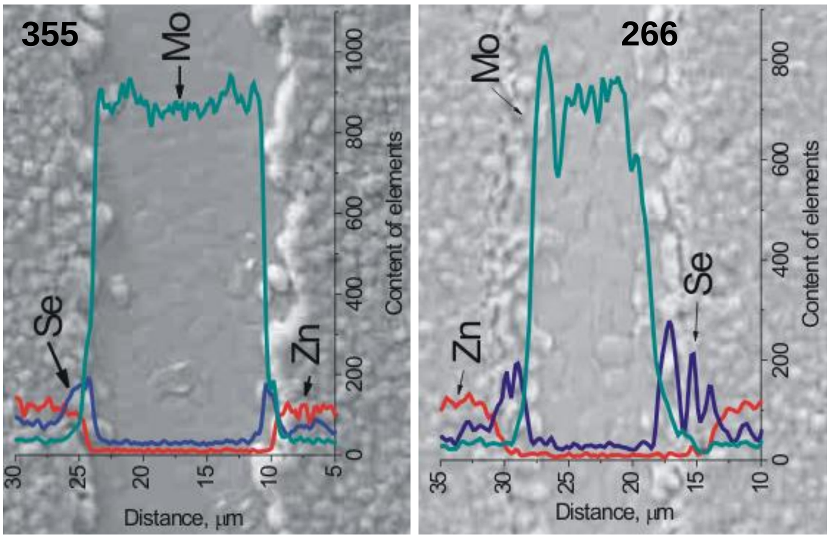

Fig. 75 SEM picture and EDS profiles of the P3 scribe in CIGS: 355 nm versus 266 nm wavelength.

A clean trench was produced by the 355 nm radiation, and remains of Se atoms from the CIGS layer were found along the trench edges in a close area, as narrow as 2 μm. Transformation in the CIGS film structure after irradiation with the 266 nm wavelength led to an intermix of ZnO and CIGS layers.

6.2.6 Processing with 1575 nm wavelength

State of the-art $CuIn_xGa_{1-x}Se_2$ (CIGS) devices generally have an average band gap energy of around 1.2 eV [29] which corresponds to 1033 nm wavelength. In all thin-film structure samples the CIGS layer was transparent to the 1064 nm laser radiation, although material lift-off process was accompanied by direct layer ablation at the edges of the Gaussian beam. This effect was caused by higher absorption at the 1064 nm wavelength in the top-contact and buffer layers. To realize a mechanical removal of thin layers by vapor pressure due to local heating of the CIGS-Mo interface the longer wavelengths should to be applied.

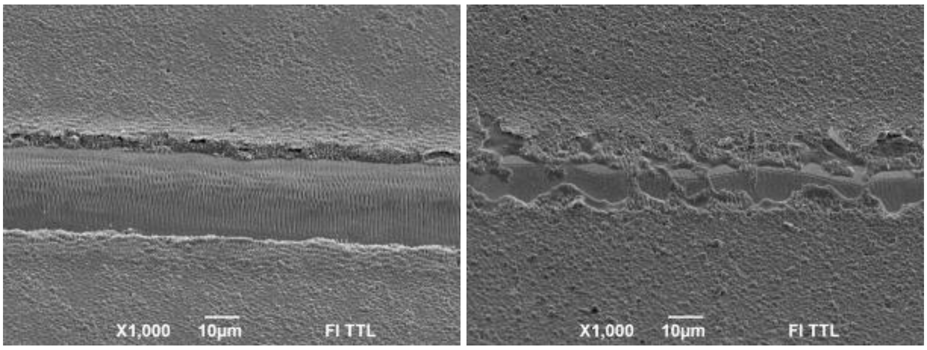

(a) (b)

Fig. 76 P3 type scribes in: (a) ITO/ZnO/CdS/CIGS/Mo/PI structure, 619 mW, 100 kHz, 40 mm/s, single pass; (b) ZnO:Al/ZnO/CdS/CIGS/Mo/PI structure, 428 mW, 100 kHz, 60 mm/s, single pass.

The pulse energy available from the used laser working at the 1572 nm wavelength was insufficient for the thermo-mechanical removal of the CIGS layer in a single scan for the structures with top-contacts (see Fig. 76). The layers were removed by the direct laser ablation process due to still high absorption in top-contact and buffer layers. In the structure of CdS/CIGS/Mo/PI, the 1572 nm laser irradiation power was high enough to remove the CIGS layer by the lift-off process due to low laser radiation absorption in thin buffer layers. The damage or melting of the material was completely prevented by the layer spallation process (see Fig. 77). As no reliable picosecond laser sources are available in this range of wavelengths, use of this approach is still challenging.

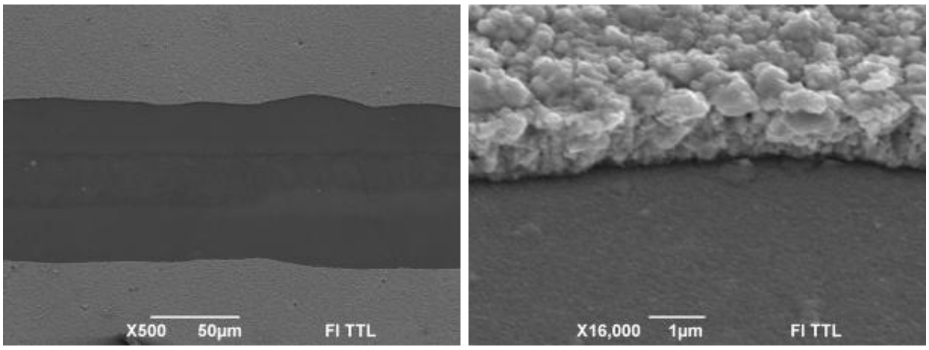

Fig. 77 P2 type process in ZnO/CdS/CIGS/Mo/PI structure, 800 mW, 50 kHz, 200 mm/s, single pass.

6.3 Conclusions

1. Removal of the double layer of the absorber with the top-contact in order to expose (open) the molybdenum layer was energetically favorable using numerous low-energy pulses. The irradiation dose required for exposure of the molybdenum layer was reduced by a factor of 2 to 3 when 10 laser pulses with the wavelength of 532 nm were applied instead of 2 high-energy pulses.
2. Selection of the right laser wavelength was important to keep the energy coupling in a well defined volume at the interlayer interface and this might be a way to achieve the selective removal of layers even in the front-side irradiation geometry, which was the only acceptable process for solar cells on flexible substrates.
3. The 1064 nm wavelength was found to be optimal for the P3 type picosecond laser scribing of the thin-film CIGS solar cells due to thermo-mechanical removal process of the CIGS layer. The laser affected area at both edges reached 51 % of total scribe width.
4. Processing with the 532 nm wavelength caused a 20 % wider melted area formation at the both edges of the scribed trench compared to the 1064 nm wavelength due to higher laser light absorption in the semiconductor layer.

5. The 355 nm laser processing did not help to increase the single pass scribing quality. The low-energy multi-pass scribing showed good results, although the process speed was too low.
6. Layer selectivity in laser processing with the 266 nm wavelength was very low. Extensive formation of the melt material was observed due to direct laser absorption on the structure surface.
7. Scribing with the 1572 nm wavelength was possible only in the thin ZnO/CdS/CIGS/Mo/PI structure. The material was removed mechanically by the micro-explosive effect of evaporated gas due to laser radiation absorption at the CIGS/Mo interface. In other solar cell structures laser scribing caused melting and damage to the underneath layers due to high absorption in the front contacts. A shorter infrared wavelength with reduced absorption on free-carriers can provide benefit in laser scribing of CIGS.

7 COMPARISON OF FEMTOSECOND AND PICOSECOND LASER PROCESSING OF THIN-FILM CIGS SOLAR CELLS

Material related to this chapter was published in **[A3]** and **[C3]**.

In this chapter the pulse length effects on laser processing of thin-film CIGS solar cells were investigated. In these experiments ablation with a train of laser pulses per spot and scribing lines were performed from the top-contact side to expose the molybdenum back-contact using lasers with both pulse durations. Optimal regimes for laser processing of every layer were estimated depending on the pulse duration.

7.1 Exposure of the back-contact with a burst of laser pulses

Exposure of the Mo back-contact with several high energy pulses was found not favorable due to pealing of top-contact and extensive melt of the CIGS layer while ablation with a burst of low energy pulses significantly reduced thermal diffusion into the thin layers and resulted in smooth ablation [109]. In our research, the ablation with a train of laser pulses per spot was performed from the top-contact side to expose the molybdenum back-contact with both lasers. Relationship between the exposed area of Mo layer and laser pulse energies is shown in Fig. 78 for both pulse durations.

For the picosecond pulse duration, the lower Mo exposure threshold compared to femtosecond pulses was found. This could be laser pulse length dependant and wavelength dependent processes:

- The 775 nm wavelength of fs laser is well absorbed by the CIGS layer and at this point the direct material ablation takes place.
- The absorption of the 1064 nm wavelength of the picosecond laser by the CIGS material is low and most of the laser energy is coupled at the Mo-PI interface. In this case the material lift-off process takes place with a higher material removal efficiency compared to the direct layer ablation.

- Another reason could be related to the lower ablation rate of the CIGS layer at femtosecond pulse duration due to the lower heat diffusion length at pulse irradiation.

A lower Mo exposure threshold at the ps laser pulse durations can be the advantage of industrial applications of picosecond lasers where the process speed and efficiency are important. Unfortunately, due to distortions in the beam shape of our femtosecond system, any comparative analysis of the crater ablation quality cannot be performed for both pulse durations, although picosecond pulses showed a larger melt area formation near the exposed Mo area.

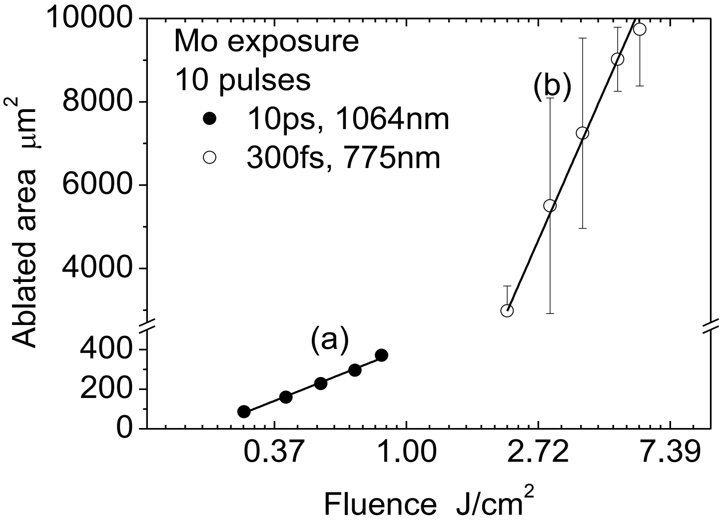

Fig. 78 Relationship between the exposed area of Mo layer and laser fluence: (a) 10 ps, 1064 nm wavelength, 200 kHz; (b) 300 fs, 775 nm wavelength, 1 kHz.

Table 12 The threshold fluencies for exposure of the molybdenum back-contact and beam diameter estimated from crater ablation for different laser pulse durations.

Pulse duration	Mo exposure threshold	Gaussian beam diameter
10 ps	0.22 J/cm^2	11.6 μm
300 fs	1.3 J/cm^2	62 μm

7.2 P3 process: exposure of the molybdenum back-contact

For both picosecond and femtosecond laser systems, the use of high pulse energies with the low pulse overlap caused a poor layer removal selectivity and damage of the Mo back-contact, although more melted CIGS material was observed when scribing with picosecond laser pulses.

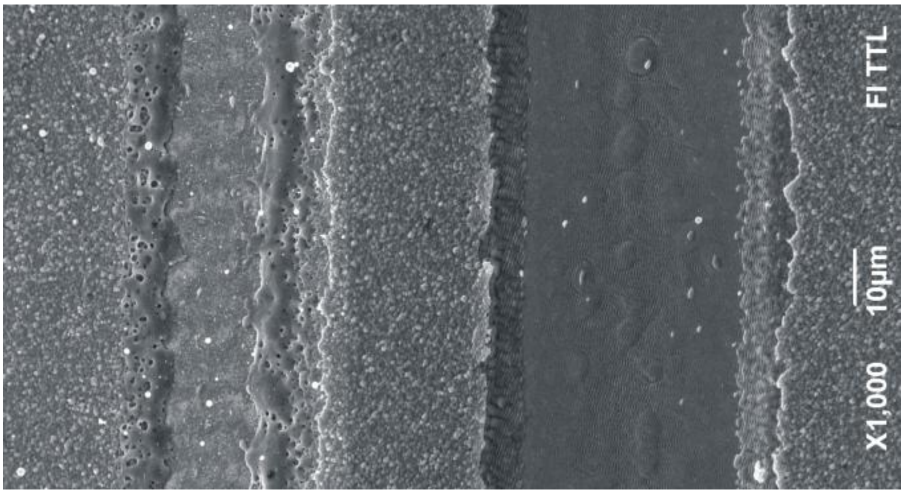

(a) (b)

Fig. 79. Tilted SEM images of the P3 scribe in ZnO:Al/ZnO/CIGS/Mo/PI structure with: (a) 10 ps, 200 kHz, 1064 nm wavelength, scribing speed 1.2 m/s; (b) 300 fs,1 kHz, 755 nm wavelength, scribing speed 4 mm/s.

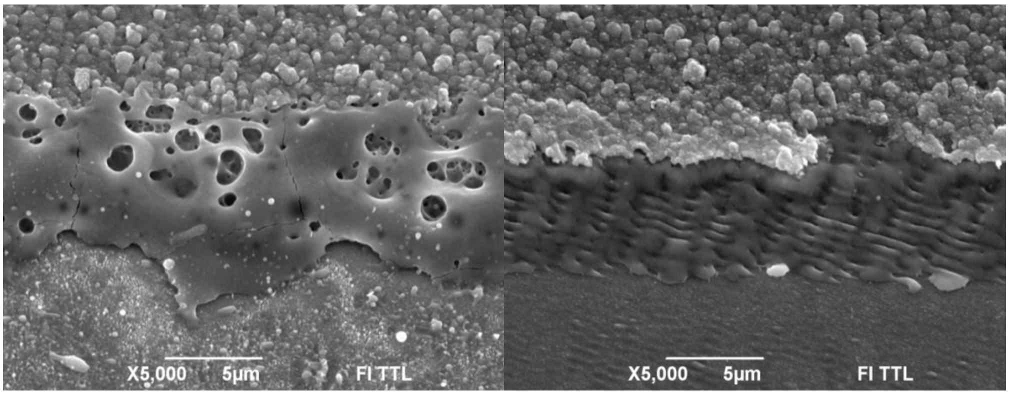

(a) 10 ps, 1.2 m/s scribing speed. (b) 300 fs, 4mm/s scribing speed.

Fig. 80. Tilted SEM images of the P3 scribe edge in ZnO:Al/ZnO/CdS/CIGS/Mo/PI structure with: (a) 10 ps, 3.5 W, 200 kHz, 17.5 μJ, 1064 nm wavelength, scribing speed 1.2 m/s; (b) 300 fs, 35 mW, 1 kHz, 35 μJ, 755 nm wavelength, scribing speed 4 mm/s.

Lowering of the pulse energy and applying higher pulse overlap facilitated an increase in selectivity of layer ablation and reduced melt formation in the CIGS layer for both pulse durations. SEM images of P3 scribe edge in the CIGS solar cell material with 10 ps and 300 fs pulse durations are shown in Fig. 79 and Fig. 80. Even under optimal scribing conditions, the larger melt area formation was observed at the picosecond laser scribe. While scribing with 300 fs laser pulses, the melt area was significantly reduced. Cleaner Mo exposure was also observed in the femtosecond regime. The Mo area was not covered with debris from the CIGS layer and a smooth Mo surface was observed. The average width of the picosecond laser affected area on the edges of the scribes was 8.1 μm and taking in account both sides of the trench it reached 51 % of the total scribe width. Processing with femtosecond laser pulses reduced the melt area width up to 5.8 μm and taking in to account both sides of the trench it reached 23 % of the total scribe with. This could be explained by lower etch rate and “colder” ablation of the material with femtosecond laser pulses. Previous work [109] revealed that even at higher melt formation of the CIGS layer during the picosecond laser scribing, no $CuSe_2$ secondary phase was detected with Raman spectroscopy. This metallic phase formation is responsible for short-circuit formation during laser scribing processes with nanosecond lasers. Going to even lower thermal ablation with femtosecond pulses, the complete, damage-free thin-film solar cell scribing can be realized.

7.3 X-ray energy dispersion (EDS) analysis

Layer selectivity and depth control are crucial for the high quality scribing of a complex thin-film solar cell. For the nanosecond regime the main limiting factor of solar cell scribing was projection of the melted Mo layer onto the sidewalls of the scribed trench [16] and a significant decrease in solar cell performance. To investigate the remaining layer structure after picosecond and femtosecond laser scribing, The SEM together with X-ray energy dispersion spectrometer measurements were applied. SEM images of the investigated area together with a map of chemical elements are presented in Fig. 81. For both pulse durations, the EDS analysis did not detect projection of molted molybdenum on the edges of the scribed trench and remaining layers still had sharp interfaces. No carbon was detected at the bottom of the scribes in both cases confirming that the Mo back-contact layer was not damaged or cracked. This demonstrates the potential of ultra-short lasers for high quality selective thin layer micromachining.

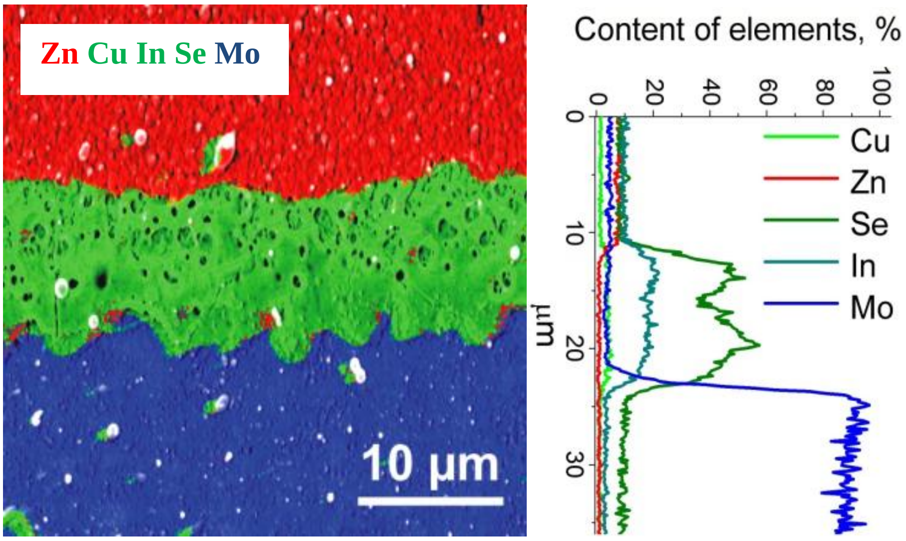

(a) 10 ps, 1.2 m/s scribing speed.

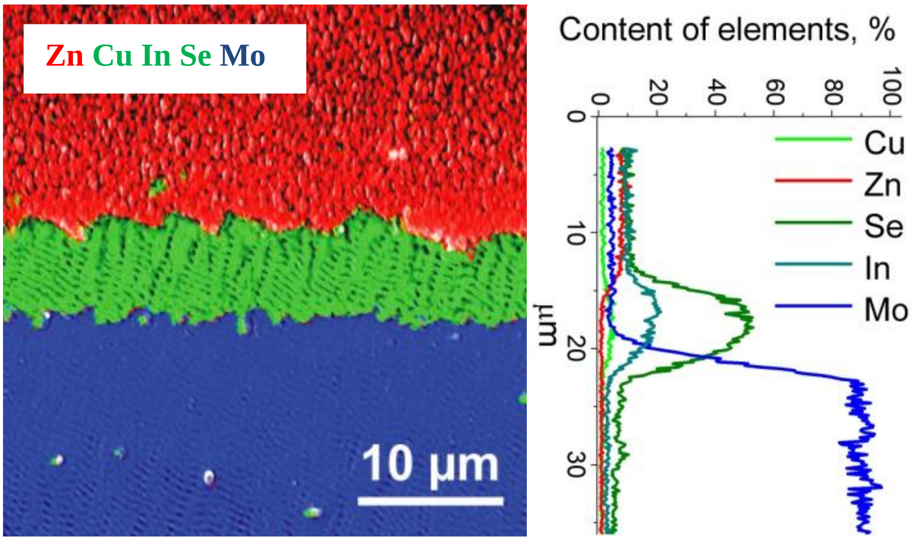

(b) 300 fs, 4 mm/s scribing speed.

Fig. 81. EDS map and cross-section of the chemical element distribution of the P3 scribe edge in ZnO/CdS/CIGS/Mo/PI structure: (a) 10 ps, 1.2 m/s scribing speed; (b) 300 fs, 4 mm/s scribing speed. Lateral resolution of the EDS detector was ~1 µm.

7.4 Conclusions

1. Picosecond laser pulses provided a 6 times higher layer removal efficiency although the remaining thermal impact on the thin layers was larger compared to the femtosecond regime.
2. The melt formation area on the edges of the picosecond laser irradiated zone reached 51 % of the total scribe width and was reduced down to 23 % by applying shorter femtosecond laser pulses, although the laser affected area was still present and was related to the Gaussian distributions of the laser beams.

8 SCRIBING PROCESS OPTIMIZATION

Material related to this chapter was published in **[A2]**, **[A4]**, **[A5]** and **[C3]**, **[C17]**.

8.1 Scribing of thin-film CIGS solar cells with the shaped laser beam of the picosecond laser

Laser scribing in multi-layered structures of modern thin-film solar cells requires high selectivity in ablation of the films without any effect on adjusted materials. A Gaussian beam profile does not enable achievement of distinct boundary, and use of flat-top shaped beams is proposed to be a solution [45]. Results of the picosecond laser scribing of the ZnO:Al/ZnO/CdS/CIGS/Mo/PI structure with the Gaussian and top-hat shaped beam profiles are shown below.

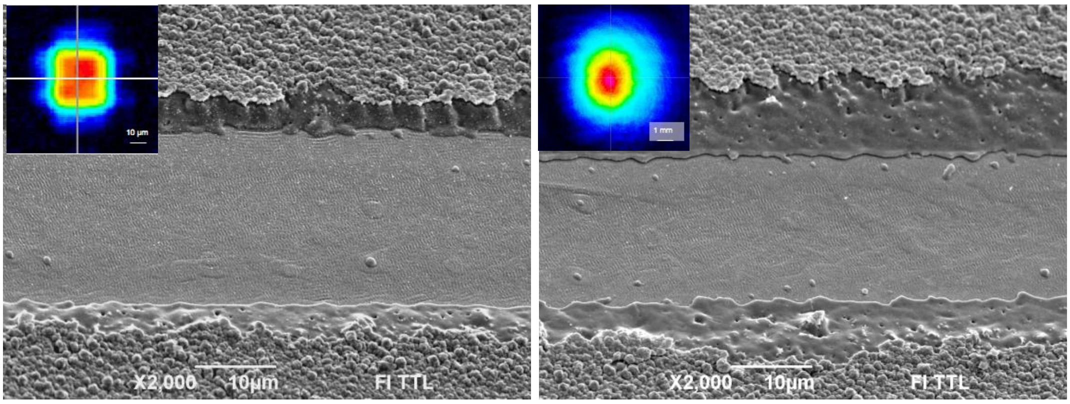

Top-hat profile beam Gaussian profile beam

Fig. 82 Tilted SEM pictures of the P3 scribe in ZnO:Al/ZnO/CIGS/ Mo/PI structure. Laser PL10100/SH, 370 mW, 100 kHz, 532 nm; scanning speed 60 mm/s, single pass.

More details about beam shaping and experimental setup can be found in section 4.3. Fig. 82 presents results of the laser scribing to expose the back-contact of Mo (so called P3 scribe). Areas of 12.3 µm in width of the disturbed absorber layer were left on both sides of the trench using the Gaussian beam and the laser affected area reached 50 % of the total scribe width. The FBS (diffractive optical element for a flat-top reshaping, see section 4.3) had higher steepness of the beam edges, which caused reduction in a width of the modified area down to 7.1 μm and 33 % of the total scribe width. The width of the trench was less sensitive to variation in the laser pulse energy for the FBS shaped beam.

8.2 Parallel beam scribing CIGS with the picosecond laser

The industrial scribing applications demand cost-effective high-speed processes that can be easily integrated into the existing production lines. Thin-film scribing usually requires laser processes with low pulse energies however at relatively low scribing speeds for industrial applications. Today high power industrial ultrashort pulsed lasers are available and to reach productivity of the process the parallel beam scribing should be used in most applications. We realized the four-parallel-beam scribing of the CIGS thin-film solar cells by installing a beam splitter into our experimental setup and still working with a single scanner head. The overall power required for the scribing was much lower than the maximum power of the used laser and processing with four or more parallel beams could be easily realized. The distance between focused parallel laser beams was controlled by controlling the splitting angle which could be changed by applying a variable beam expander in the optical setup. All laser scribing regimes fitted well in a new four-beam scribing setup, although the laser power had to be multiplied as we were working with four beams. More details could be found in section 4.2. The same scribing conditions (focusing, power) could be maintained for parallel beams with a proper repeatability of laser scribed trenches (see Fig. 83). This shows a potential for optimizing laser scribing processes for CIGS solar cells and satisfying the demand of industry in terms of process productivity and economical point of view.

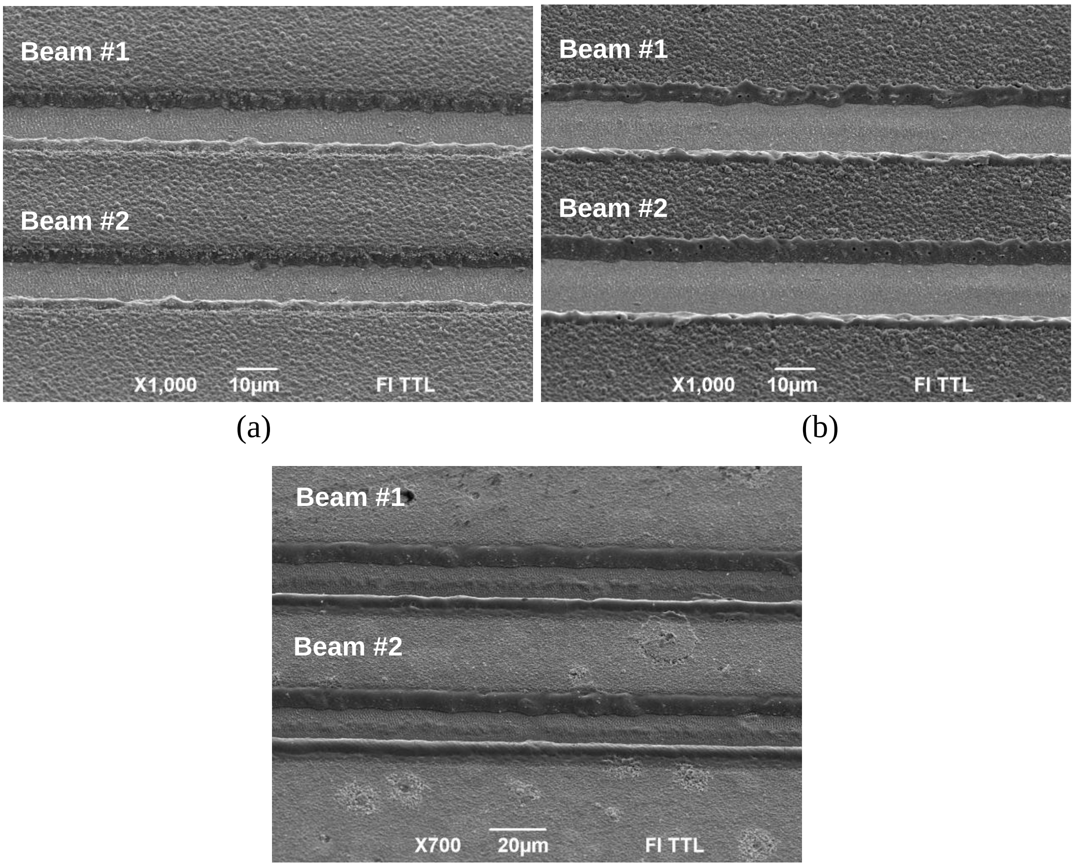

(a) (b)

(c)

Fig. 83 SEM images of parallel beam P3 step scribing in: (a) ITO/ZnO/CIGS/Mo/PI structure, 2x450 mW, 100 kHz, single pass at 90 mm/s; (b) ZnO:Al/ZnO/CIGS/Mo/PI structure, 2x600 mW, 100 kHz, single pass at 200 mm/s; (c) ZnO/CdS/CIGS/Mo/PI structure, 2x450 mW, 100 kHz, single pass at 200 mm/s.

8.3 Conclusions

1. The multi-beam scribing enabled using full power of the laser and maximizing process speed. The same scribing conditions (focusing, power) were maintained for parallel beams with a good repeatability for laser scribed trenches.
2. The beam shaping enabled a better control of the thin layer removal process and reduced the width of laser affected area at the edges by 34 %.
3. By applying the multi-beam and beam shaping techniques it was possible to increase the overall process speed and maintain the scribing quality.

9 ANALYSIS OF LASER-SCRIBED AREAS

Material related to this chapter was published in **[A2]**, **[A4]** and **[C3]**, [**C4]**, [**C12]**.

In order to investigate laser processing impact to the solar cell electrical properties completely operating solar cells of prefabrication stage (Solarion AG) with the average efficiency of 10.7% and the active surface area of 32 cm^2 were scribed between the contact grid using the optimal scribing parameters with both picosecond and femtosecond laser systems (see Fig. 84). Then the electrical properties of the laser scribed solar cell were investigated with listed techniques below. The total length of laser scribes was 360 mm in all cases.

Fig. 84 Red lines indicate laser scribed trenches in complete single cell. The total length of the scribes was 360 mm.

9.1 Raman measurements of laser-affected area

CIGS is a thermally sensitive material and laser scribing can lead to structural changes on the melted edges of the scribe. Formation of Cu_xSe metallic phase in the CIGS material close to the laser-scribed zone may cause an internal shunt formation and reduction in solar cell performance [110]. Therefore, laser scribed areas were investigated by Raman spectroscopy to track formation of the secondary metallic phase of Cu_xSe near the scribing zone. The Raman spectrum was measured in four areas starting from the edge of the scribe as shown by the numbers in Fig. 85. The main peak in Raman spectra is the A1 vibration line of $CuInSe_2$ at 174 cm^{-1}, with a shift to longer wavenumbers for CIGS [111]. The shoulder at 150-160 cm^{-1} which appeared after laser processing reflects the presence of defected state of CIGS crystals, called the "ordered vacancy compound" [112]. A broad line in the range of 210-230 cm^{-1} is a combined intrinsic vibration B_2/E of CIGS [113]. Alterations in Raman spectra are obvious in the melt area (walls) as well as outside the trench, where the film was irradiated with wings of the Gaussian beam. However, those changes in spectra do not show any evidence of the secondary metallic phase formation during picosecond laser scribing because the secondary phase Cu_xSe undesired for photovoltaic applications appears in Raman spectra at 262 cm^{-1} [112]. These measurements confirmed ability of picosecond lasers to scribe CICS thin-film solar cells with low thermally-induced structural changes of the material near the scribing zone.

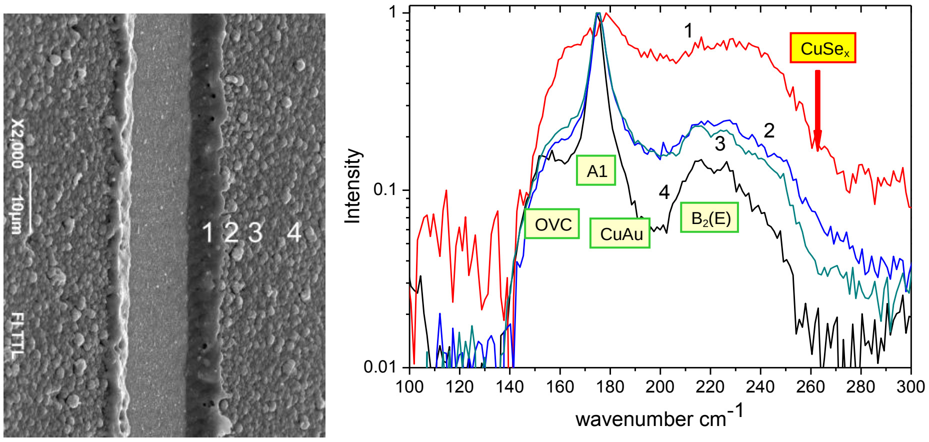

Fig. 85 Raman spectra of ZnO:Al/ZnO/CdS/CIGS/Mo/Pi structure. Numbers of curves correspond to a position on a sample (left).

9.2 Lock-in thermography measurements

The main limiting factor to reach higher solar cell efficiencies is the defect accumulation in the absorber material causing the internal shunt formation and decrease in photo-current. Laser scribing could lead to defect formation and the shunt detection near the laser affected areas is an important step to characterize electrical properties of any solar cell. Lock-in thermography has proven to be a valuable technique for non-uniformity diagnostics in crystalline and polycrystalline solar cells [97,98]. It utilizes ac infrared imaging of a device, where the temperature is affected by an external ac voltage at the same lock-in frequency. The thermography maps thus represent the current distributions [114]. The lock-in thermography temperature distribution maps are shown in Fig. 86.

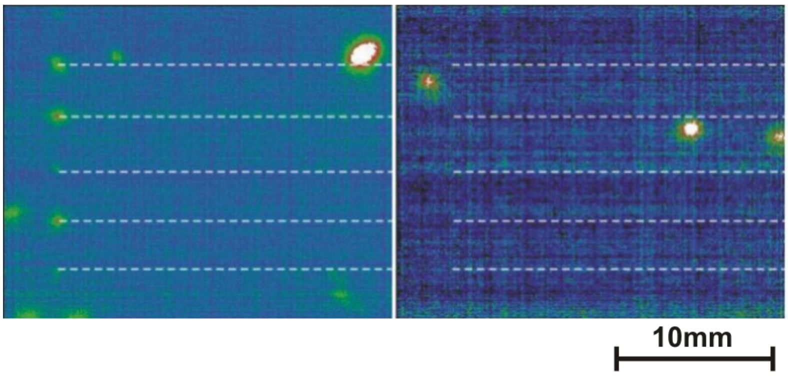

(a) (b)

Fig. 86 Map of temperature distribution in CIGS solar cell area after laser scribing. Blue area represents the colder part of the surface, while red color represents a warm part. White lines represent laser scribes made using lasers with pulse duration of: (a) 10 ps, (b) 300 fs.

The film-deposition defects were clearly visible and they caused a short-current leak at the examined surface although these defects were created in the production of the solar cell and were not related to the laser scribing. In the picosecond regime some increase in temperature was detected at the end of the laser scribes and this is related to the tune-up of the scanning system because the laser beam was switched off too late after the motion stopped. In the area where the laser beam was moving at a constant speed, no change in the surface temperature was observed. For the femtosecond scribing regime, no temperature change was detected close to the scribing area either.

These results conclude that no significant internal shunt formation was detected during laser scribing with pulses of both durations. The IR camera was optimized for large area observation and the resolution was too poor to observe the area in the range of a scribe width and small defects might not be detected.

9.3 Laser-beam-induced current (LBIC) measurements

The laser-beam-induced current is a nondestructive optical technique for the detection of semiconductor defects [115]. In this technique, a laser beam is applied to the material to induce current to flow through two ohmic contacts placed on the boundary. The LBIC image consists of measurements of the total local current flowing out through contacts and induced by a local illumination with a laser. The diode laser beam was focused into a 50 µm spot and this defined the resolution of the measurements. The map of LBIC measurement areas close to laser scribe is shown in Fig. 87.

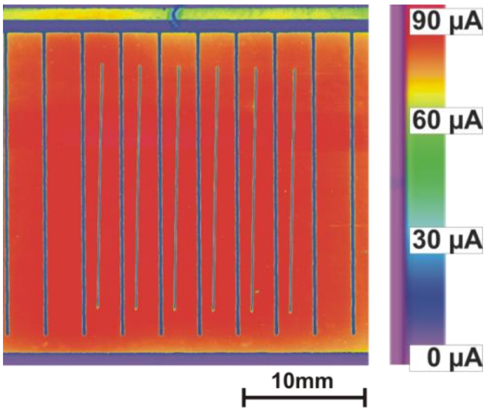

Fig. 87 Photo-current map of the solar cell area after picosecond (10 ps) laser scribing.

Laser scribing was applied between the grids of front-contact. The LBIC map showed uniform distribution of current in the area close to scribe lines made with the picosecond laser. The dead area near the scribe was minimal, although the resolution of our measurements did not allow us to investigate the defect formation on a micro-scale at the edge of ablated trench.

9.4 Performance test of solar cells after the laser scribing

Manufacturing of real working mini-modules with laser processes series interconnects requires integration of the laser system to the solar cell production line. This requires a lot of investment and was not possible in the research. For this purpose completely operating solar cells of prefabrication stage were scribed as shown in Fig. 84. The efficiency tests were performed before and after laser scribing to evaluate the influence of laser scribing on the solar cell performance under standard testing conditions (standard global spectra AM 1.5 and 1000 W/m^2 total irradiance).

Three solar cells were scribed with 10 ps laser pulses and also three cells were processed with the 300 fs pulsed laser. The results of efficiency and parallel-resistance measurements are shown in Table 13.

Table 13 Photo-electrical efficiency of CIGS solar cells and $R_{parallel}$ measurement results before and after laser scribing.

	Eff, before laser scribing, %	Eff. After laser scribing, %	Average reference cell Eff. drop %	Absolute eff. drop, %	Absolute $R_{parallel}$ drop, Ohm
10 ps					
#1	10.6	10.41	0.16	0.03	7.09
#2	9.99	9.18		0.57	-0.46
#3	9.7	9.1		0.44	
Average				**0.35**	**3.3**
300 fs					
#4	10.19	9.25	0.16	0.78	-1.36
#5	9.59	9.42		0.01	-0.75
#6	9.96	9.88		-0.08	26.49
Average				**0.24**	**8.13**

The definition of an absolute average drop of the solar cell initial efficiency was used. It was equal to the difference of the efficiency before and after laser scribing process including any spontaneous efficiency degradation of solar cells in time due to contact with ambient air which was controlled using the reference cells without laser scribing. The efficiency tests after femtosecond and picosecond laser scribing showed the 0.24 % and 0.35 % efficiency decrease in solar cell performance during laser scribing. Solar cell samples processed with the femtosecond laser showed marginally better performance. This could be related to the less thermal ablation of the CIGS layer with femtosecond pulses, although still defect formation near the laser-affected zone occurred.

9.5 Conclusions

1. The micro-Raman measurements in the area close to the scribing zone edge did not detect any metallic phase formation which could be responsible for the shunt formation and degradation of the absorber layer.
2. The picosecond and femtosecond laser scribing of the CIGS solar cell structures provides high quality process, because the LIT and LBIC measurements with available spatial resolution were not able to detect any defected areas after the laser scribing.
3. The solar cell efficiency test revealed 0.24-0.35 % degradation in efficiency after the laser scribing was applied to the solar cell samples. Even using ultrashort pulsed lasers for scribing of the GIGS material, the narrow melted edge and laser affected area were formed due to the Gaussian distribution of the laser beam and most likely in these zones generation of shunts and defects induced reduction of electrical properties of investigated solar cells.

MAIN CONCLUSIONS

1. Selection of the right laser wavelength is important to keep the energy coupling in a well defined volume at the interlayer interface and this might be a way to achieve the selective removal of layers even in the front-side irradiation geometry, which is the only acceptable for solar cells on flexible substrates.
2. The 1064 nm wavelength was found to be optimal for the P3 type picosecond laser scribing of the investigated thin-film CIGS solar cells due to thermo-mechanical removal process of the CIGS layer.
3. By applying the multi-beam and beam shaping techniques it was possible to optimize the overall process speed and maintain the scribing quality.
4. The solar cell efficiency test revealed marginal 0.24-0.35 % degradation in efficiency after the laser scribing was applied to the solar cell samples. Even using ultrashort pulsed lasers for scribing of the GIGS material, the narrow melted edge and laser affected area were formed due to Gaussian distribution of the laser beam and most likely in these zones generation of shunts and defects induced reduction of electrical properties of investigated solar cells.

SUMMARY

The PhD thesis is the experimental and theoretical analysis of thin layer ablation processes for photovoltaic devices. The picosecond (10 ps) femtosecond (300 fs) lasers in the ablation and scribing experiments were used. Flexible CIGS solar cell samples were investigated with different top-contact structures. Laser scribing was performed at different wavelengths including: 1575 nm, 1064 nm, 775 nm, 532 nm, 355 nm and 266 nm. Laser-scribed areas were investigated with optical and scanning electron microscopes together with EDS (X-ray energy dispersion) and Raman spectrometers. Electrical characterization was obtained by LIT (Lock-in thermography), LBIC (Laser beam induced current measurements) techniques. The efficiency of the solar cells after laser scribing was also investigated.

Experimental work was supported by modeling and simulation of energy coupling and dissipation inside the layers. Selectiveness of the ablation process was defined by optical and mechanical properties of the materials, and selection of the laser wavelength facilitated control of the structuring process.

The 1064 nm wavelength was found optimal for the CIGS solar cell scribing in terms of quality and the process speed. It is a very positive result in case of industrial applications as the cost and system complexity are reduced.

The solar cell efficiency test revealed a minor degradation in photo-electrical efficiency after the laser scribing was applied to the solar cell samples. Lock-in thermography measurements did not reveal any internal shunt formation during laser scribing with the picosecond pulse duration.

Picosecond lasers with fundamental harmonics and high repetition rates can be used to accomplish an efficient and fast scribing process which is able to satisfy the demands for industrial solar cell scribing applications.

REFERENCES

[1] K. Zweibel. *The Terawatt Challenge for Thin Film Photovoltaics*. (John Wiley & Sons, Ltd, 2006).

[2] T. M. Razykov, C. S. Ferekides, D. Morel *et al.*: Solar photovoltaic electricity: Current status and future prospects, Solar Energy 85, 1580-1608, (2011).

[3] M. Kaelin, D. Rudmann and A. N. Tiwari: Low cost processing of CIGS thin film solar cells, Solar Energy 77, 749-756, (2004).

[4] D. Graham-Rowe: Solar cells get flexible, Nat Photon 1, 433-435, (2007).

[5] F. Long and et al.: CIS(CIGS) thin films prepared for solar cells by one-step electrodeposition in alcohol solution, Journal of Physics: Conference Series 152, 012074, (2009).

[6] U. P. Singh and S. P. Patra: Progress in Polycrystalline Thin-Film Cu(In,Ga)Se_2 Solar Cells, International Journal of Photoenergy 2010, (2010).

[7] P. Jackson, D. Hariskos, E. Lotter *et al.*: New world record efficiency for Cu(In,Ga)Se2 thin-film solar cells beyond 20%, Progress in Photovoltaics: Research and Applications, 894-897, (2011).

[8] A. Jeager-Waldau: Photovoltaic Status Report 2011 - Research, Solar Cell Production and Market Implementation of Photovoltaics, European Commission, (2011).

[9] F. Colville, C. Dunsky and J. Hopkins: Existing and emerging laser applications within PV manufacturing, Photovoltaics International 1, 72, (2008).

[10] F. Kessler and D. Rudmann: Technological aspects of flexible CIGS solar cells and modules, Solar Energy 77, 685-695, (2004).

[11] C. Dunsky and F. Colville: Solid state laser applications in photovoltaics manufacturing, Proceedings of SPIE 6871, (2008).

[12] A. D. Compaan, I. Matulionis and S. Nakade: Laser scribing of polycrystalline thin films, Optics and Lasers in Engineering 34, 15-45, (2000).

[13] R. Tanaka, T. Takaoka, H. Mizukami, T. Arai and Y. Iwai: Laser etching of indium tin oxide thin films by ultra-short pulsed laser, SPIE, 5063, 370-373, (2003).

[14] J. Hermann, M. Benfarah, S. Bruneau *et al.*: Comparative investigation of solar cell thin film processing using nanosecond and femtosecond lasers, Journal of Physics D: Applied Physics 39, 453, (2006).

[15] C. Molpeceres and et al.: Microprocessing of ITO and a-Si thin films using ns laser sources, Journal of Micromechanics and Microengineering 15, 1271, (2005).

[16] J. Hermann, M. Benfarah, G. Coustillier *et al.*: Selective ablation of thin films with short and ultrashort laser pulses, Applied Surface Science 252, 4814-4818, (2006).

[17] A. Jager-Waldau: Progress in chalcopyrite compound semiconductor research for photovoltaic applications and transfer of results into actual solar cell production, Solar Energy Materials and Solar Cells 95, 1509-1517, (2011).

[18] *First Solar pushes PV costs down to $0.76/W*, <http://optics.org/news/1/2/22>, (2010.07.03).

[19] T. Sullivan. *How Thin-Film Solar Will Fare Against Crystalline Silicon's Challenge* <http://www.renewableenergyworld.com/rea/news/article/2011/01/how-thin-film-solar-will-fare-against-crystalline-silicons-shallenge>, (2011.11.17).

[20] C. A. Wolden, J. Kurtin, J. B. Baxter *et al.*: Photovoltaic manufacturing: Present status, future prospects, and research needs, Journal of Vacuum Science & Technology A: Vacuum, Surfaces, and Films 29, 030801, (2011).

[21] M. A. Green, K. Emery, Y. Hishikawa, W. Warta and E. D. Dunlop: Solar cell efficiency tables (Version 38), Progress in Photovoltaics: Research and Applications 19, 565-572, (2011).

[22] *Elektros energijos, atitinkančios viešuosius interesus elektros energetikos sektoriuje, kainos (be PVM)*, Valstybinė kainų ir energetikos kontrolės komisija, <http://www.regula.lt/lt/elektra/tarifai/viap_kainos.php>, (2011.11.21).

[23] *Photovoltaic Geographical Information System*, Joint research center-Institute of energy, <http://re.jrc.ec.europa.eu/pvgis/apps4/pvest.php#>, (2011.11.18).

[24] *Whole sale solar*, <http://www.wholesalesolar.com/ >, (2011.11.22).

[25] *Affordable solar*, <http://www.affordable-solar.com >, (2011.11.22).

[26] *Go green solar*, <http://www.gogreensolar.com >, (2011.11.22).

[27] *Solar home*, <http://www.solarhome.com >, (2011.11.22).

[28] A. Shah. *Thin-film silicon solar cells*. (EPFL Press ; distributed by CRC Press, 2010).

[29] A. Chirilă, S. Buecheler, F. Pianezzi *et al.*: Highly efficient Cu(In,Ga)Se2 solar cells grown on flexible polymer films, Nat Mater advance online publication, (2011).

[30] S. Ishizuka, A. Yamada, P. Fons and S. Niki: Flexible Cu(In,Ga)Se_2 solar cells fabricated using alkali-silicate glass thin layers as an alkali source material, Journal of Renewable and Sustainable Energy 1, 013102, (2009).

[31] G. J.F: The puzzle of Cu(In,Ga)Se2 (CIGS) solar cells stability, Thin Solid Films 403-404, 405-409, (2002).

[32] D. Neelkanth G: Toward GW/year of CIGS production within the next decade, Solar Energy Materials and Solar Cells 91, 1376-1382, (2007).

[33] D. M. Mattox. *Handbook of physical vapor deposition (PVD) processing: film formation, adhesion, surface preparation and contamination control*. (Noyes Publications, 1998).

[34] D. Schmid, M. Ruckh and H. W. Schock: A comprehensive characterization of the interfaces in Mo/CIS/CdS/ZnO solar cell structures, Solar Energy Materials and Solar Cells 41-42, 281-294, (1996).

[35] M. A. Contreras, M. J. Romero, B. To *et al.*: Optimization of CBD CdS process in high-efficiency Cu(In,Ga)Se_2-based solar cells, Thin Solid Films 403-404, 204-211, (2002).

[36] S. H. Kwon, S. C. Park, B. T. Ahn, K. H. Yoon and J. Song: Effect of CuIn3Se5 layer thickness on $CuInSe_2$ thin films and devices, Solar Energy 64, 55-60, (1998).

[37] K. Ramanathan. *Properties of high-efficiency CIGS thin-film solar cells [electronic resource]*. (National Renewable Energy Laboratory, 2005).

[38] M. A. Green: Solar Cells, Prentice-Hall, Engtewood Cliffs, NJ, (1982).

[39] A. Yamada, K. Matsubara, K. Sakurai *et al.*: Effect of band offset on the open circuit voltage of heterojunction $CuIn_{1-x}Ga_xSe_2$ solar cells, Applied Physics Letters 85, 5607-5609, (2004).

[40] R. Murison, C. Dunsky, M. Rekow *et al.*: CIGS P1, P2, P3 Laser Scribing with an Innovative Fiber Laser, Photovoltaic Specialists Conference (PVSC), 000179-000184, (2010).

[41] F. Colville and P. H. Drive: Laser Systems & Processes within Next Generation Photovoltaic Manufacturing Equipment Photovoltaic Manufacturing Technology Conference, Semicon Europa, Stuttgart, (2008).

[42] P. Gečys and G. Račiukaitis: Scribing of a-Si thin-film solar cells with picosecond laser, The European Physical Journal Applied Physics 51, 33209, (2010).

[43] J. Bovatsek, A. Tamhankar, R. S. Patel, N. M. Bulgakova and J. Bonse: Thin film removal mechanisms in ns-laser processing of photovoltaic materials, Thin Solid Films 518, 2897-2904, (2010).

[44] S. Haas, A. Gordijn and H. Stiebig: High speed laser processing for monolithical series connection of silicon thin-film modules, Progress in Photovoltaics: Research and Applications 16, 195-203, (2008).

[45] G. Račiukaitis and P. Gečys: Picosecond-Laser Structuring of Thin Films for CIGS Solar Cells Journal of Laser Micro/Nanoengineering 5, 10-15, (2010).

[46] A. Virtuani, E. Lotter, M. Powalla *et al.*: Influence of Cu content on electronic transport and shunting behavior of Cu(In,Ga)Se_2 solar cells, Journal of Applied Physics 99, 014906-014917, (2006).

[47] J. H. Scofield, A. Duda, D. Albin, B. L. Ballard and P. K. Predecki: Sputtered molybdenum bilayer back contact for copper indium diselenide-based polycrystalline thin-film solar cells, Thin Solid Films 260, 26-31, (1995).

[48] P. O. Westin, U. Zimmermann and M. Edoff: Laser patterning of P2 interconnect via in thin-film CIGS PV modules, Solar Energy Materials and Solar Cells 92, 1230-1235, (2008).

[49] P. O. Westin, U. Zimmermann, M. Ruth and M. Edoff: Next generation interconnective laser patterning of CIGS thin film modules, Solar Energy Materials and Solar Cells 95, 1062-1068, (2011).

[50] S. Wiedeman, J. Kessler, T. Lommasson *et al.*: Challenges in large-area, thin-film CIGS modules, AIP Conference Proceedings 353, 12-18, (1996).

[51] A. Wehrmann, H. Schulte-Huxe, M. Ehrhardt *et al.*: Change of electrical properties of CIGS thin-film solar cells after structuring with ultrashort laser pulses, 7921, 79210T, (2011).

[52] S. Kijima and T. Nakada: High-Temperature Degradation Mechanism of Cu(In,Ga)Se_2-Based Thin Film Solar Cells, Applied Physics Express 1, 075002,

[53] G. Andrä, J. Bergmann and F. Falk: Laser crystallized multicrystalline silicon thin films on glass, Thin Solid Films 487, 77-80, (2005).

[54] X. Maeder, C. Niederberger, S. Christiansen *et al.*: Microstructure and lattice bending in polycrystalline laser–crystallized silicon thin films for photovoltaic applications, Thin Solid Films 519, 58-63, (2010).

[55] D. Bäuerle. *Laser Processing and Chemistry*. (Springer, 2011).

[56] Y. H. Jo, B. C. Mohanty and Y. S. Cho: Enhanced electrical properties of pulsed laser-deposited $CuIn_{0.7}Ga_{0.3}Se_2$ thin films via processing control, Solar Energy 84, 2213-2218, (2010).

[57] M. A. Contreras, B. Egaas, K. Ramanathan *et al.*: Progress toward 20% efficiency in Cu(In,Ga)Se2 polycrystalline thin-film solar cells, Progress in Photovoltaics: Research and Applications 7, 311-316, (1999).

[58] M. Kemell, M. Ritala and M. Leskelä: Thin Film Deposition Methods for $CuInSe_2$ Solar Cells, Critical Reviews in Solid State and Materials Sciences 30, 1-31, (2005).

[59] M. Pavlišta, M. Hrdlička, P. Němec, J. Přikryl and M. Frumar: Thickness distribution of thin amorphous chalcogenide films prepared by pulsed laser deposition, Applied Physics A: Materials Science & Processing 93, 617-620, (2008).

[60] J. Levoska and et al.: Pulsed laser ablation deposition of $CuInSe_2$ and $CuIn_{1-x}Ga_xSe_2$ thin films, Physica Scripta 1994, 244, (1994).

[61] M. D. Abbott, T. Trupke, H. P. Hartmann, R. Gupta and O. Breitenstein: Laser isolation of shunted regions in industrial solar cells, Progress in Photovoltaics: Research and Applications 15, 613-620, (2007).

[62] A. Wehrmann, S. Puttnins, L. Hartmann *et al.*: Analysis of laser scribes at CIGS thin-film solar cells by localized electrical and optical measurements, Optics & Laser Technology,

[63] H. P. Huber, M. Englmaier, C. Hellwig *et al.*: High speed structuring of CIS thin-film solar cells with picosecond laser ablation, 7203, 72030R, (2009).

[64] D. Ruthe, K. Zimmer and T. Höche: Etching of $CuInSe_2$ thin films—comparison of femtosecond and picosecond laser ablation, Applied Surface Science 247, 447-452, (2005).

[65] G. Heise, M. Dickmann, M. Domke *et al.*: Investigation of the ablation of zinc oxide thin films on copper–indium-selenide layers by ps laser pulses, Applied Physics A: Materials Science & Processing 104, 387-393, (2011).

[66] A. Burn, V. Romano, M. Muralt *et al.*: Selective ablation of thin films in latest generation CIGS solar cells with picosecond pulses, SPIE, 8243, 824318, (2012).

[67] G. Heise, M. Domke, J. Konrad *et al.*: Monolithical Serial Interconnects of Large CIS Solar Cells with Picosecond Laser Pulses, Physics Procedia 12, Part B, 149-155, (2011).

[68] F. Kessler, D. Herrmann and M. Powalla: Approaches to flexible CIGS thin-film solar cells, Thin Solid Films 480–481, 491-498, (2005).

[69] O. Stenzel. *Planar Interfaces* in *The Physics of Thin Film Optical Spectra– An Introduction*, 71-100 (Springer, 2005).

[70] M. Fox. *Optical Properties of Solids*. 317 (Oxford, 2001).

[71] R. Wester. *Energy Transport and Heat Conduction* in *Tailored Light 2*, 43-62 (Springer, 2011).

[72] I. N. Mihailescu and J. Hermann. *Laser–Plasma Interactions* in *Laser Processing of Materials*, 49-88 (Springer, 2010).

[73] A. Kruusing. *Handbook of Liquids-Assisted Laser Processing*. (Elsevier, 2008).

[74] N. M. Bulgakova, A. V. Bulgakov and L. P. Babich: Energy balance of pulsed laser ablation: thermal model revised, Applied Physics A: Materials Science & Processing 79, 1323-1326, (2004).

[75] N. M. Bulgakova and A. V. Bulgakov: Pulsed laser ablation of solids: transition from normal vaporization to phase explosion, Applied Physics A: Materials Science & Processing 73, 199-208, (2001).

[76] L. V. Zhigilei, Z. Lin, D. S. Ivanov *et al. Atomic/Molecular-Level Simulations of Laser–Materials Interactions* in *Laser-Surface Interactions for New Materials Production – Tailoring Structure*, 43-72 (Springer, 2010).

[77] M. Beresna, T. Gertus, R. Tomašiūnas, H. Misawa and S. Juodkazis: Three-Dimensional Modeling of the Heat-Affected Zone in Laser Machining Applications, Hindawi Publishing Corporation Laser Chemistry 976205, 1-6, (2008).

[78] L. Jiang and H.-L. Tsai: Improved Two-Temperature Model and Its Application in Ultrashort Laser Heating of Metal Films, Journal of Heat Transfer 127, 1167-1173, (2005).

[79] Y. Zhang and J. K. Chen: Ultrafast melting and resolidification of gold particle irradiated by pico- to femtosecond lasers, Journal of Applied Physics 104, 054910-054919, (2008).

[80] S. I. Anisimov, B. L. Kapeliovich and T. L. Perelman: Electron emission from metal surfaces exposed to ultrashort laser pulses, Sov. Phys. JETP 39, 375-377, (1974).

[81] J. K. Chen, D. Y. Tzou and J. E. Beraun: A semiclassical two-temperature model for ultrafast laser heating, International Journal of Heat and Mass Transfer 49, 307-316, (2006).

[82] B. H. Christensen, K. Vestentoft and P. Balling: Short-pulse ablation rates and the two-temperature model, Applied Surface Science 253, 6347-6352, (2007).

[83] H. Hirori, T. Tachizaki, O. Matsuda and O. B. Wright: Electron dynamics in chromium probed with 20-fs optical pulses, Physical Review B 68, 113102, (2003).

[84] S. D. Brorson, A. Kazeroonian, J. S. Moodera *et al.*: Femtosecond room-temperature measurement of the electron-phonon coupling constant gamma in metallic superconductors, Physical Review Letters 64, 2172, (1990).

[85] Y. P. Meshcheryakov and N. M. Bulgakova: Thermoelastic modeling of microbump and nanojet formation on nanosize gold films under femtosecond laser irradiation, Applied Physics A: Materials Science & Processing 82, 363-368, (2006).

[86] *ITO*, <http://www.reade.com/Products/Oxides/indium_tin_oxide.html >, (2011.05.12).

[87] *Zinc oxide*, <http://en.wikipedia.org/wiki/Zinc_oxide >, (2011.05.12).

[88] *Mo*, <http://en.wikipedia.org/wiki/Molybdenum >, (2011.05.14).

[89] *Polyimide*, <http://en.wikipedia.org/wiki/Polyimide >, (2011.05.14).

[90] *Cadmium sulfide*, <http://en.wikipedia.org/wiki/Cadmium_sulfide >, (2011.05.14).

[91] G. Račiukaitis, M. Brikas, M. Gedvilas and G. Darčianovas: Patterning of ITO layer on glass with high repetition rate picosecond lasers, J. Laser Micro/Nanoeng. 2, 1-6, (2007).

[92] <http://refractiveindex.info/ >. (2011.05.12).

[93] S.-S. Wellershoff, J. Hohlfeld, J. Güdde and E. Matthias: The role of electron–phonon coupling in femtosecond laser damage of metals, Applied Physics A: Materials Science & Processing 69, S99, (1999).

[94] F. M. Dickey and S. C. Holswade. *Laser beam shaping: theory and techniques*. (Marcel Dekker, 2000).

[95] J. M. Liu: Simple technique for measurements of pulsed Gaussian-beam spot sizes, Optics Letters 7, 196-198, (1982).

[96] Y. Jee, M. F. Becker and R. M. Walser: Laser-induced damage on single-crystal metal surfaces, Journal of the Optical Society of America B: Optical Physics 5, 648-659, (1988).

[97] O. Breitenstein, K. Iwig and I. Konovalov: Evaluation of Local Electrical Parameters of Solar Cells by Dynamic (Lock-In) Thermography, physica status solidi (a) 160, 271-282, (1997).

[98] O. Breitenstein, M. Langenkamp, O. Lang and A. Schirrmacher: Shunts due to laser scribing of solar cells evaluated by highly sensitive lock-in thermography, Solar Energy Materials and Solar Cells 65, 55-62, (2001).

[99] G. Busse, D. Wu and W. Karpen: Thermal wave imaging with phase sensitive modulated thermography, Journal of Applied Physics 71, 3962-3965, (1992).

[100] F. J. Navas, R. Alcántara, C. Fernández-Lorenzo and J. Martín-Calleja: High resolution laser beam induced current images under trichromatic laser radiation: Approximation to the solar irradiation, Review of Scientific Instruments 81, 035108, (2010).

[101] D. J. Gardiner, P. R. Graves and H. J. Bowley. *Practical Raman spectroscopy*. (Springer, 1989).

[102] N. Bianco, O. Manca and B. Morrone: Instationary conjugate optical-thermal fields in thin films due to pulsed laser heating: A comparison between back and front treatment, Heat and Mass Transfer 34, 255-261, (1998).

[103] C. M. Group. *Electron-Phonon Coupling and Electron Heat Capacity in Metals at High Electron Temperatures*, <http://faculty.virginia.edu/CompMat/electron-phonon-coupling/>, (2011.12.15).

[104] Y. P. Meshcheryakov and N. M. Bulgakova: Thermoelastic modeling of microbump and nanojet formation on nanosize gold films under femtosecond laser irradiation, Applied Physics A: Materials Science & Processing 82, 363-368, (2006).

[105] C. W. Ong, D. G. Zong, M. Aravind, C. L. Choy and D. R. Lu: Tensile strength of zinc oxide films measured by a microbridge method, Journal of Materials Research 18, 2464-2472, (2003).

[106] *Oxford Indium, Biz Esp Ltd., technical bulletin*.

[107] G. Račiukaitis, M. Brikas, M. Gedvilas and T. Rakickas: Patterning of indium–tin oxide on glass with picosecond lasers, Applied Surface Science 253, 6570-6574, (2007).

[108] A. Rockett: The Electronic effects of point defects in $CuIn_xGa_{(1-x)}Se_2$, Thin Solid Films 361–362, 330-337, (2000).

[109] P. Gecys, G. Raciukaitis, E. Miltenis, A. Braun and S. Ragnow: Scribing of Thin-film Solar Cells with Picosecond Laser Pulses, Physics Procedia 12, 141-148, (2011).

[110] H. Miyazaki, R. Mikami, A. Yamada and M. Konagai: $Cu(InGa)Se_2$ thin film absorber with high Ga contents and its application to the solar cells, Journal of Physics and Chemistry of Solids 64, 2055-2058, (2003).

[111] C.-M. Xu, X.-L. Xu, J. Xu *et al.*: Composition dependence of the Raman A1 mode and additional mode in tetragonal Cu–In–Se thin films, Semiconductor Science and Technology 19, 1201, (2004).

[112] X. Fontane, V. Izquierdo-Roca, L. Calvo-Barrio *et al.*: In-depth resolved Raman scattering analysis of secondary phases in Cu-poor CuInSe[sub 2] based thin films, Applied Physics Letters 95, 121907, (2009).

[113] D. Wang, L. Wan, Z. Bai and Y. Cao: Mixed phases in p-type $CuInSe_2$ thin films detected by using micro-Raman scattering spectroscopy, Applied Physics Letters 92, 211912, (2008).

[114] D. Shvydka, J. P. Rakotoniaina and O. Breitenstein: Lock-in thermography and nonuniformity modeling of thin-film CdTe solar cells, Applied Physics Letters 84, 729-731, (2004).

[115] W. Fang and K. Ito: Reconstruction of Semiconductor Doping Profile from Laser-Beam-Induced Current Image, SIAM Journal on Applied Mathematics 54, 1067-1082, (1994).